

MIXED CARBORANETHIOL SELF-ASSEMBLED MONOLAYERS ON GOLD  
SURFACES

A THESIS SUBMITTED TO  
THE GRADUATE SCHOOL OF NATURAL AND APPLIED SCIENCES  
OF  
MIDDLE EAST TECHNICAL UNIVERSITY

BY

NIMA SOHRABNIA

IN PARTIAL FULFILLMENT OF THE REQUIREMENTS  
FOR  
THE DEGREE OF MASTER OF SCIENCE  
IN  
CHEMISTRY

FEBRUARY 2017



Approval of the thesis:

**MIXED CARBORANETHIOL SELF-ASSEMBLED MONOLAYERS ON  
GOLD SURFACES**

submitted by **Nima Sohrabnia** in partial fulfillment of the requirements for the degree  
of **Master of Science in Chemistry Department, Middle East Technical University**  
by,

Prof. Dr. Gülbin Dural Ünver  
Dean, Graduate School of **Natural and Applied Sciences**

\_\_\_\_\_

Prof. Dr. Cihangir Tanyeli  
Head of Department, **Chemistry**

\_\_\_\_\_

Assoc. Prof. Dr. Mehmet Fatih Danışman  
Supervisor, **Chemistry Dept., METU**

\_\_\_\_\_

Prof. Dr. Ayşen Yılmaz  
Co-Supervisor, **Chemistry Dept., METU**

\_\_\_\_\_

**Examining Committee Members:**

Prof. Dr. Gülsün Gökağaç  
Chemistry Dept., METU

\_\_\_\_\_

Assoc. Prof. Dr. M. Fatih Danışman  
Chemistry Dept., METU

\_\_\_\_\_

Prof. Dr. Ayşen Yılmaz  
Chemistry Dept., METU

\_\_\_\_\_

Prof. Dr. Atilla Cihaner  
Chemical Eng. and Applied Chemistry Dept., Atilim Uni.

\_\_\_\_\_

Assoc. Prof. Dr. İrem Erel Göktepe  
Chemistry Dept., METU

\_\_\_\_\_

**Date:** 03.02.2017

**I hereby declare that all the information in this document has been obtained and presented in accordance with academic rules and ethical conduct. I also declare that, as required by these rules and conduct, I have fully cited and referenced all material and results that are not original to this work.**

Name, Last Name: Nima Sohrabnia

Signature:

## ABSTRACT

### MIXED CARBORANETHIOL SELF-ASSEMBLED MONOLAYERS ON GOLD SURFACES

Sohrabnia, Nima

M.S., Chemistry Department

Supervisor: Assoc. Prof. M. Fatih Danişman

Co-Supervisor: Prof. Dr. Ayşen Yılmaz

February 2017, 118 pages

Thiolated derivatives of dicarba-closo-dodecaborane, HS-C<sub>2</sub>B<sub>10</sub>H<sub>11</sub> (carboranethiols, CTs), with icosahedral molecular structure are one of the promising candidates for self-assembled monolayer (SAM) applications. CT SAMs possess various advantages relative to organic counterparts, such as high stability towards chemical, oxidative and thermal degradations as well as having fewer defects. In this study, pure and mixed SAMs of three different positional isomers of carboranethiols (namely M1, O1 and M9) on template stripped gold surfaces were grown from solution and characterized. Global properties of the SAMs were studied by means of contact angle (CA) and ellipsometric spectroscopy measurements. The ellipsometric thickness of all SAMs were found to be about 1 nm which is consistent with the reported thickness, measured by scanning tunneling microscopy, in the literature. In case of pure SAMs, M1 was observed to have the highest CA (85.4±1.8) whereas O1 SAMs have the lowest CA value (71.2±0.7). The dominant component that governs surface wettability was found to be M1 in mixed M1:M9 and O1:M1 SAMs. This is due to head to tail dipole-dipole interactions of M1 molecules on the surface. In case of M1:M9 co-deposited SAMs, CA was observed to increase with increasing M1 concentration in the growth solution.

Such a clear trend was only present, however, in the advancing CAs for O1:M1 co-deposited SAMs. On the other hand, contact angles of O1:M9 co-deposited films were observed to increase linearly with increasing M9 ratio in the growth solution. The morphological properties of the SAMs were investigated by atomic force microscopy and all SAMs were found to have similar properties with the exception of low defect concentration observed for O1:M9 films.











1.8 Motivation of study .....	38
2.EXPERIMENTAL .....	41
2.1 Experimental techniques .....	41
2.1.1 Atomic force microscopy (AFM).....	41
2.1.2 Spectroscopic Ellipsometry .....	43
2.1.3 Contact angle.....	46
2.1.3.1 Static contact angle.....	48
2.1.3.2 Dynamic contact angle .....	49
2.2 General experimental procedures .....	50
2.2.1 Au film and self assembled monolayer preparation.....	50
2.2.2 Template stripping procedure.....	52
2.2.2.1 Thermally curing .....	54
2.2.2.2 UV-Visible assisted crosslinking .....	54
2.2.3 Contact angles .....	56
2.2.4 Spectroscopic ellipsometry .....	57
2.2.5 Atomic force microscopy .....	57
3.RESULTS AND DISCUSSION .....	61
3.1 Gold substrates .....	61
3.1.1 Thermally evaporated gold film.....	61
3.1.2 Hydrogen flame annealing gold .....	62
3.1.3 Template stripped gold.....	65
3.2 Alkanethiol SAMs.....	67
3.3 Carboranethiol SAMs.....	73
3.3.1 Pure carboranethiol SAMs .....	74
3.3.2 Mixed carboranethiol SAMs .....	78
3.3.2.1 M1:M9 mixed SAMs .....	78
3.3.2.2 O1:M1 mixed SAMs .....	83
3.3.2.3 O1:M9 mixed SAMs .....	87
3.4 Summary .....	91
4.CONCLUSION .....	95



## LIST OF TABLES

### TABLES

<b>Table 1.</b> Contact angle of Carboranthiol (2),(3) and (4) SAMs. ....	32
<b>Table 2.</b> Contact angle of Carboranthiol of M1, M9 and M1:M9 mixed SAMs.....	34
<b>Table 3.</b> Results of quantitative analysis of thermally evaporated gold.....	62
<b>Table 4.</b> Contact angle results of reference SAMs. ....	70
<b>Table 5.</b> Results of quantitative analysis of AFM for ODT and MUD growth ODT. .....	71
<b>Table 6.</b> Contact angle results of 3 s and 10 s growth ODT film. ....	72
<b>Table 7.</b> Results of quantitative analysis of AFM for 3 s and 10 s growth ODT film. .....	72
<b>Table 8.</b> Contact angles of pure carboranethiol SAMs.....	75
<b>Table 9.</b> Contact angles of M1 and M9 in literature.....	75
<b>Table 10.</b> Results of the AFM image analysis for pure M1, M9 and O1 films. ....	76
<b>Table 11.</b> Contact angles of M1:M9 mixed SAMs.....	80
<b>Table 12.</b> Results of the AFM image and contact angle analysis of M1:M9 SAMs.	81
<b>Table 13.</b> Contact angles of O1:M1 mixed SAMs. ....	84
<b>Table 14.</b> Results of the AFM image and contact angle analysis of O1:M1 SAMs..	84
<b>Table 15.</b> Contact angles of O1:M1 mixed SAMs. ....	88
<b>Table 16.</b> Results of the AFM image and contact angle analysis of M1:M9 SAMs.	88

## LIST OF FIGURES

### FIGURES

- Figure 1.** Overview of various preparation routes of crystalline organic thin films. Retrieved from ref [3]. ..... 2
- Figure 2.** a) Schematic representation of a SAM. b) Representation of different energy scales in SAM system. Retrieved from ref [7]. ..... 3
- Figure 3.** A) A model showing the structure of monolayer and the primitive unit cell (small oblique) of the Au(111) surface. The rectangular unit cell shows the  $c(4 \times 2)$  or  $(2\sqrt{3} \times 3)$  rect superstructure (rectangle), while the large oblique unit cell shows the  $(\sqrt{3} \times \sqrt{3})R30^\circ$ . B) Schematic of angular degrees of freedom of alkanethiol.  $\theta$  is tilt angle from normal of surface,  $\Psi$  is twist angle and  $\phi$  projection of molecule in substrate plane. .... 4
- Figure 4.** The different absorption sites on Au(111). Grey dot represents “top” site, red dot indicates a bridge site and blue one corresponds to a hollow site (hcp or fcc). ..... 6
- Figure 5.** Scheme of the different steps taking place during the self-assembly of alkanethiol on Au(111): (i) physisorption, (ii) lying down phase formation, (iii) nucleation of the standing up phase, (iv) completion of the standing up phase. Retrieved from ref [52]. ..... 8
- Figure 6.** A) Tapping mode AFM image of single crystal Au(111) surface of  $2 \mu\text{m} \times 2 \mu\text{m}$ . The black arrow shows a pinhole whereas red one shows a grain boundary. The blue arrow shows step edges. Retrieved from ref [53]. B) STM image of octanethiol SAM on gold surface. The red arrow shows a vacancy island and blue arrow shows a grain boundaries of SAM. Retrieved from ref [56]. ..... 10
- Figure 7.** STM images of a freshly prepared octanethiol self-assembled monolayer on Au(111). STM images are taken sequentially to show the structural transformation. (i)  $(\sqrt{3} \times \sqrt{3})R30^\circ$  structure. ( $4 \text{ nm} \times 4 \text{ nm}$ ). (ii)  $c(4 \times 2)$ -ns, (The

absorbed molecules only has brightness difference when compared to  $(\sqrt{3}\times\sqrt{3})R30^\circ$  structure.) (4 nm  $\times$  4 nm). (iii)  $c(4\times 2)$ -s structure (The absorbed molecules have brightness difference and displacement when compared to  $(\sqrt{3}\times\sqrt{3})R30^\circ$  structure.) (4 nm  $\times$  4 nm) (iv) Reverses to the  $(\sqrt{3}\times\sqrt{3})R30^\circ$  structure (4 nm  $\times$  4 nm). Retrieved from ref [64] . . . . . 12

**Figure 8.** (a) STM image with size of 200 nm x 200 nm. The clean Au(111) surface. Inset arrows indicate the FCC and HCP stacked regions and the elbow sites. (b) STM image showing the surface at the early stage of adsorption with size of 150 nm x 150 nm. Arrow 1 indicate molecules at an elbow site; arrow 2 shows molecules at a step edge; arrow 3 shows molecules within the FCC region; arrow 4 shows a dense molecular island. (c) STM image (150 nm x 150 nm) indicates selective population of the FCC stacked regions by well-spaced molecules. (d) STM image (150 nm x 150 nm) shows the completion of the first molecular layer. The herringbone reconstruction could be observed through the molecular layer. All images were obtained at 120 K. retrieved from ref [37]. . . . . 13

**Figure 9.** Thermally evaporated gold on Mica and corresponding line scan. Retrieved from ref [66]. . . . . 14

**Figure 10.** A) AFM image of thermally evaporated gold. B) Hydrogen flame annealed gold. C) Cross-section area from green square in (b). Retrieved from ref [77]. 15

**Figure 11.** Automatically flat surface preparation by template stripping procedure. . . . . 16

**Figure 12.** STM images of  $5\times 5 \mu\text{m}^2$  scan area. Inset shows the RMS roughness of surface. A) Thermally evaporated gold on mica. B) TS gold prepared by Epo-tek 377. C) TS gold prepared by Cerastil C7. D) TS gold prepared by Panavia 21. Retrieved from ref [80]. . . . . 18

**Figure 13.** AFM image of template-stripped gold. A) ultra-flat template stripped gold AFM. B) Defects observed in template stripped gold. Retrieved from ref [81]. 18

**Figure 14.** Static contact angle of various SAMs on Au(111). . . . . 20

**Figure 15.** a) AFM image of template stripped gold. b) Contact angle of alkanethiols on template stripped gold. c) AFM image of thermally evaporated gold on mica.

d) contact angle of alkanethiols on thermally evaporated gold. Retrieved from ref [87].	21
<b>Figure 16.</b> Model representing end group conformation of even and odd carbon containing alkanethiols. Retrieved from ref [87].	21
<b>Figure 17.</b> a) Ellipsometric thickness of SAMs. Line indicates calculated thickness by the equation. b) Schematic representation of relationship between the components of the equation. Retrieved from ref [82].	22
<b>Figure 18.</b> A) STM image of octylthiol SAM on gold with surface coverage of 0.11 (striped phase). B) STM image of methylthiol at low coverage. The middle atom corresponds to gold adatom. As can be seen there is cis and trans conformation related to methylthiol. C) STM image of methylthiol at full coverage. The proposed relationship between 3x4 structure (D) and $c(4 \times 2)$ phase (F) is also shown. Both have zig zag structure. As the length of alkane chain increases interaction of chains increases as well, resulting in the more ordered trans structure. Retrieved from ref [36,93–95].	24
<b>Figure 19.</b> a) AFM image of bare Au(111) with hexagonal structure. b) AFM image Octadecanethiol on gold surface. Hexagonal structure of SAM is shown by vectors. c) AFM image of decancthiol. d) AFM image of hexanethiol. Retrieved from ref [96].	25
<b>Figure 20.</b> AFM images of butanethiol at different time of immersion in 1mM solution. a) 1 second. b) 10 seconds. c) 30 seconds. d) 3 minutes where surface covered completely. Retrieved from ref [98].	26
<b>Figure 21.</b> AFM image of butanethiol/octadecancthiol mixed SAMs. a) 20/1 .b)40/1. Retrieved from ref [98].	27
<b>Figure 22.</b> Schematic diagram of an alkanethiol SAM on gold. The organic adlayer can be envisaged as two layers of dipoles with dipole moments $\mu_1$ and $\mu_2$ . The net dipole moment, $\mu_{net}$ is also shown.	28
<b>Figure 23.</b> Chemical structures of M1, M9and O1 carboranethiols. Numbering system is shown in M1. Grey: carbon, pink: boron, yellow: sulphur, white: hydrogen.	30
<b>Figure 24.</b> Structure of carboranethiols studied. Retrieved from ref [104].	30

<b>Figure 25.</b> Gold nano particles size coloration with mole ratio carboranethiol (2) to $\text{HAuCl}_4 \cdot 3\text{H}_2\text{O}$ . Retrieved from ref [104].	31
<b>Figure 26.</b> a) Chemical structure of m-1-carboranethiol (M1), m-9-carboranethiol (M9). b) Dipole moment direction of carboranes. The dipole moment vectors are pointing from negative pole to positive pole. Retrieved from ref [105].	32
<b>Figure 27.</b> STM images of SAMs of a) M1. b) M9 and c) an adlayer prepared from a 1:1 solution on gold surface. Onset in a and b correspond to fourier transforms image A and B showing reciprocal lattice. Retrieved from ref [105].	34
<b>Figure 28.</b> Grazing incidence FTIR spectra of M1 (red) and M9 (blue) on gold surface. The right figure show the overlap of the M1 and M9. Retrieved from ref [105].	35
<b>Figure 29.</b> Head to tail dipole moment of M1 and perpendicular dipole of M9. Retrieved from ref [105].	35
<b>Figure 30.</b> A) UPS spectra of Au surfaces decorated with pure or mixed SAMs. B) calculated work function of the gold surface covered by carboranethiols with respect to M1 mole fraction. Retrieved from ref [106].	37
<b>Figure 31.</b> A) Water contact angle and hexadecane contact angle. Water contact angle shows direct relation to M1 ratio. In all cases hexadecane wets surface completely. B) Performance of OFET constructed by using bare and SAM decorated gold electrodes. M1 shows best result by reducing injection barrier. C) Schematic representation of the injection barriers. Retrieved from ref [106].	37
<b>Figure 32.</b> Dipole moments direction of M1, M9 and O1. Grey: carbon, pink: boron, yellow: sulphur: white: hydrogen. Dipole moment vectors are pointing from the negative pole to positive pole.	39
<b>Figure 33.</b> Schematic illustration of AFM working principle. Retrieved from ref [108].	42
<b>Figure 34.</b> illustrative force vs distance curve between the scanning tip and sample.	43
<b>Figure 35.</b> The working principle of spectroscopic ellipsometry. Retrieved from ref [109].	45

<b>Figure 36.</b> Experimentally measured data fitted with models A) Fitted template stripped gold film by using Drude-Lorenz dielectric function and gold/air two phase model. B) Fitted carboranethiol film by using the reference gold parameters, Cauchy dielectric function for SAM and gold/Sam/air three phase model.....	46
<b>Figure 37.</b> Related interfacial tension in contact angle. ....	47
<b>Figure 38.</b> Static contact angle of 1-Octadecanethiol SAM on thermally evaporated gold on mica. ....	48
<b>Figure 39.</b> a) Advancing contact angle measurement of 1-Octadecanethiol SAM on gold. b) Receding contact angle measurement of 1-Octadecanethiol SAM on gold.....	50
<b>Figure 40.</b> The chemical structure of molecules was used in this thesis. ODT and MUD was the reference molecules to optimization instruments and SAMs preparation. Grey: carbon, pink: boron, yellow: sulphur, white: hydrogen, red: oxygen. Theoretical lengths are calculated at AM1 level for alkanethiols and at DFT (PBE) level for carboranethiols.....	51
<b>Figure 41.</b> Activation of triaryl sulfonium hexafluoroantimonate catalyzer.....	53
<b>Figure 42.</b> Polymerization of SU 8 after activating catalyst. Intra as well as inter molecular polymerization takes place via in cross linking. ....	53
<b>Figure 43.</b> Image of a successfully stripped gold film by thermal curing of SU-8...	54
<b>Figure 44.</b> UV-Visible assisted crosslinking. A) 1 hour light illuminated then kept in ethanol for 12 hours. B) 1 hour light illuminated and hard baked for 24 hours then kept in ethanol. ....	55
<b>Figure 45.</b> Successfully stripped gold by UV-Visible assisted cross linking.....	56
<b>Figure 46.</b> AFM image processing: A) A processed image and the program window that shows the used parameters. B) Raw height image of the sample. ....	59
<b>Figure 47.</b> A) AFM topography images of thermally evaporated gold on mica. B) processed image for analysis.....	62
<b>Figure 48.</b> Hydrogen flame annealed gold on mica substrate. A) 1 min. B) 2 min. C) 3 min. D) 4min. E) 5 min. F) 6 min. ....	63

**Figure 49.** Treatments to eliminate contamination. A) piranha treated Au surface. B) ozone treated Au surface. C) microscopic contamination on gold which was flamed for 5 min. D) AFM image of contaminated gold surface after 5 min. ... 64

**Figure 50.** A) SEM image of 5 min flame annealed gold on mica with scan size of 250x250  $\mu\text{m}^2$ . B) SEM image of the same sample at scan size of 7.5x7.5  $\mu\text{m}^2$ . C) SEM image with scan size 5x5  $\mu\text{m}^2$ . D) AFM image of the 5 min flamed annealed with scan size of 1.25x1.25  $\mu\text{m}^2$ . E) Result of EDX survey of point that shown in C. .... 65

**Figure 51.** AFM image of Template stripped gold surface. A) scanned with Nanomagetics ambient. B) Same image with corresponding line scans to show surface roughness. C) The profile of green line which shows ultra-flat surface. D) The profile of grey line which passed over pinhole with 2nm depth. E) Template stripped gold surface scanned with Veeco MultiMode V. F) Corresponding line profile of E. .... 67

**Figure 52.** Schematic presentation of reference SAMs on surface. A) ODT SAM. B) MUD SAM. The molecular length and SAMs thicknesses are related to each other and can be calculated by considering the tilt angle of the molecules. The blue line indicate theoretical length of molecules from center of top hydrogen to center of sulfur. Dash line shows sulfur-gold bond length. Black lines show the theoretical thickness of SAMs. .... 68

**Figure 53.** Contact angle and ellipsometric thickness of ODT and MUD on TS-Au and FA-Au..... 70

**Figure 54.** AFM images of alkanethiol SAMs on template stripped and flame annealed (30 s) gold. A) ODT on template stripped gold. B) ODT on flame annealed gold. C) MUD on template stripped gold. D) MUD on flame annealed gold. .... 70

**Figure 55.** Contact angle and ellipsometric thickness of ODT growth from solution for 3 s and 10 s. .... 72

**Figure 56.** AFM image of ODT growth for A) 3 s and B) 10 s. .... 72

**Figure 57.** Contact angles and ellipsometric thickness for pure carboranethiols. Solid symbols refer to FA gold and the open symbols refer to TS gold surfaces. .... 75

<b>Figure 58.</b> AFM images of pure M9, M1 and O1 SAMs on template stripped gold surface. Upper rows correspond to 1.25x1.25 $\mu\text{m}^2$ and bottom rows 2.5x2.5 $\mu\text{m}^2$ . .....	77
<b>Figure 59.</b> Contact angles and ellipsometric thicknesses of M1:M9 mixed SAMs. Lines in the CAs plot indicate theoretical CAs plotted by assuming surface fraction being equal to solution fraction. S: static, A: advancing and R: receding contact angles. ....	80
<b>Figure 60.</b> A) Theoretical contact angles as a function of surface composition for mixed M1:M9 SAMs. B) Surface composition of mixed M1:M9 SAMs calculated from the observed contact angles, plotted as a function of growth solution composition. S: static, A: advancing and R: receding contact angles. ....	80
<b>Figure 61.</b> AFM images of Mixed M1:M9 SAMs on template stripped gold surface. Upper rows correspond to 1.25x1.25 $\mu\text{m}^2$ and bottom rows 2.5x2.5 $\mu\text{m}^2$ . ....	82
<b>Figure 62.</b> Contact angles and ellipsometric thicknesses of O1:M1 mixed SAMs. Lines in CAs indicate plotted theoretical CAs against $q_{\text{surf}}$ by assuming surface fraction being equal to solution fraction. S: static, A: advancing and R: receding contact angles. ....	84
<b>Figure 63.</b> A) Theoretical contact angles as a function of surface composition for mixed O1:M1 SAMs. B) Surface composition of mixed O1:M1 SAMs calculated from the observed contact angles, plotted as a function of growth solution composition. S: static, A: advancing and R: receding contact angles. ....	85
<b>Figure 64.</b> AFM images of mixed O1:M1 SAMs on template stripped gold surface. Upper rows correspond to 1.25x1.25 $\mu\text{m}^2$ and bottom rows 2.5x2.5 $\mu\text{m}^2$ . ....	86
<b>Figure 65.</b> Contact angles and ellipsometric thicknesses of O1:M9 mixed SAMs. Lines in the CAs plot indicate theoretical CAs plotted by assuming surface fraction being equal to solution fraction. S: static, A: advancing and R: receding contact angles. ....	88
<b>Figure 66.</b> A) Theoretical contact angles as a function of surface composition for mixed O1:M9 SAMs. B) Surface composition of mixed O1:M9 SAMs calculated	

from the observed contact angles, plotted as a function of growth solution composition. S: static, A: advancing and R: receding contact angles..... 89

**Figure 67.** AFM images of Mixed O1:M1 SAMs on template stripped gold surface. Upper rows correspond to 1.25x1.25  $\mu\text{m}^2$  and bottom rows 2.5x2.5  $\mu\text{m}^2$ . ..... 90

**Figure 68.** Schematic representation O1:M9 dipole-dipole interaction on surface... 92

**Figure 69.** Summary of the AFM image analysis results performed on 1.25  $\mu\text{m}$  x 1.25  $\mu\text{m}$  images (a) and 2.5  $\mu\text{m}$  x 2.5  $\mu\text{m}$  images (b). Boundary lengths in (b) is divided by 4 for comparison with (a). ..... 93

**Figure 70.** Gold decorated with polar aromatic groups. The structural differences as well as the direction of the dipole moments of corresponding organic adlayer is shown. .... 105

**Figure 71.** A1 and B1 shows the chemical structure of SAMs. A2 and B2 represent the UV photoemission spectra for clean Au and corresponding Au modified SAM. A3 and B3 is schematic diagram of the differences in work function ( $\Delta W$ ) of Au and modified surface. Retrieved from ref [102]. ..... 107

**Figure 72.** Oligophenylthiols SAMs structure and effect of them on work function. 108

**Figure 73.** Synthetic route of 1-Mercapto-1,7 -dicarba-*closo*-dodecaborane-7-carboxylic acid. .... 109

**Figure 74.** IR spectra of reactant (upper row) and product (bottom row). ..... 110

**Figure 75.**  $^1\text{H}$  of 1-Mercapto-1,7 -dicarba-*closo*-dodecaborane-7-carboxylic acid 110

**Figure 76.**  $^{13}\text{C}$  NMR 1-Mercapto-1,7-dicarba-*closo*-dodecaborane-7-carboxylic acid. .... 111

**Figure 77.** Contamination observed on mica substrate upon heating..... 118

## LIST OF ABBREVIATIONS

<b>SAM</b>	Self Assembled Monolayer
<b>CAs</b>	Contact Angles
<b>TS</b>	Template Stripped
<b>TE</b>	Thermally Evaporated
<b>FA</b>	Flame Annealed
<b>CT</b>	Carboranethiol
<b>ODT</b>	1-octadecanethiol
<b>MUD</b>	11-Mercapto-1-undecanol
<b>WF</b>	Work Function
<b>GIXRD</b>	Grazing Incidence X-ray Diffraction
<b>LEED</b>	Low Energy Electron Diffraction
<b>DFT</b>	Density Functional Theory
<b>AFM</b>	Atomic Force Microscopy
<b>STM</b>	Scanning Tunneling Microscopy
<b>SPM</b>	Scanning Probe Microscopy
<b>M1</b>	m-Carborane-1-Thiol
<b>M9</b>	m-Carborane-9-Thiol
<b>O1</b>	o-Carborane-1-Thiol





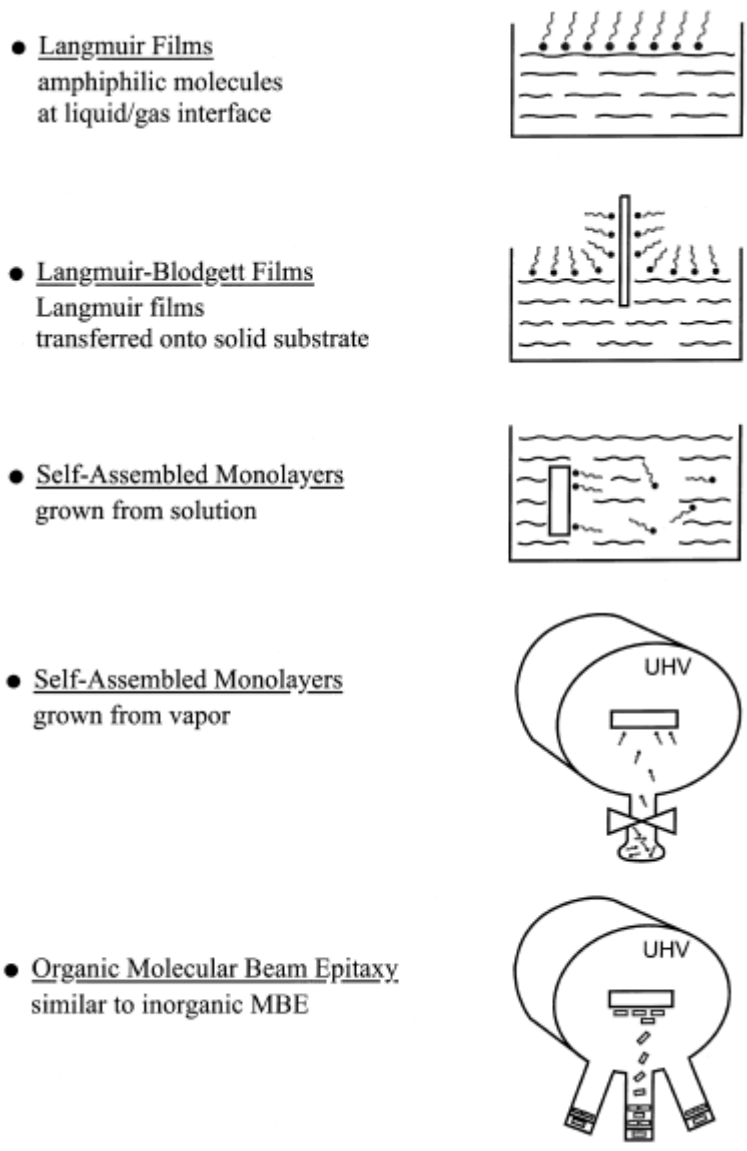


**Figure 1.** Overview of various preparation routes of crystalline organic thin films. Retrieved from ref [3].

**1.2 Thiol SAMs: kinetics and mechanism of SAM formation**

Extensive studies have been conducted on SAMs of thiols and disulfides on Au(111) after their discovery by Nuzzo and Allara in 1983. [9] Since then, tunable interfacial properties and their applications in molecular technologies have become the focal

point of attention in SAM studies. Fundamental phenomena and processes of great importance such as adhesion and bonding [10], surface wetting, friction and lubrication [2], biocompatibility [11], protein and cell adhesion [12,13] and interfacial electron transfer [14,15] have been studied using SAMs of thiols on Au(111).

To determine/control the structure of SAMs, thiol molecules' chemical composition is the main parameter for consideration. Intermolecular interactions (e.g. van der Waals,  $\pi$ - $\pi$  interactions), extent of which is found to be dependent on the spacing between the molecular backbones, and endgroup-endgroup interactions cause the two-dimensional ordering in SAMs. [7] More interestingly, conformation of the individual molecular backbones within the assembly, their packing orientation and ordering with respect to each other are determined by the interplay between intermolecular interactions, inter-terminal group interactions and the interaction of the headgroup with the surface together with entropic effects as depicted in **Figure 2**.

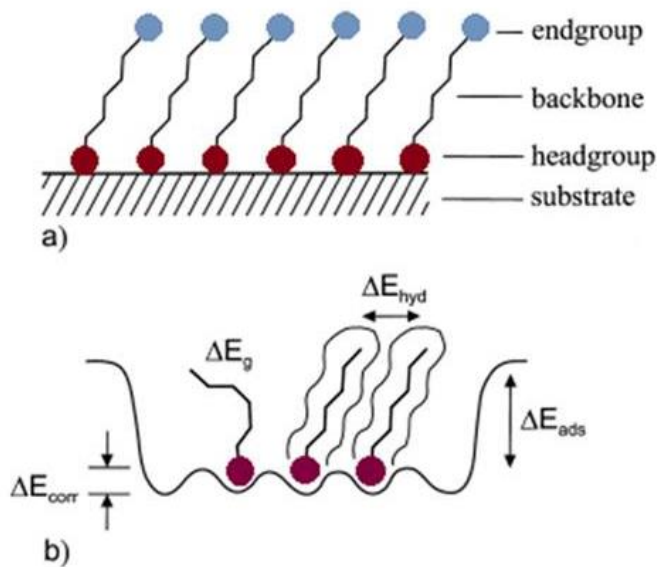


**Figure 2.** a) Schematic representation of a SAM. b) Representation of different energy scales in SAM system. Retrieved from ref [7].

The thiol SAMs on an Au(111) surface are the most comprehensively studied and well characterized SAM systems. These systems were scrutinized by numerous experimental techniques such as FTIR [16,17], surface-enhanced Raman spectroscopy

[18,19], diffraction of electrons, x-rays [20,21], helium atoms [22], atomic force microscopy [23,24] and scanning tunneling microscopy. [25,26] All of these characterization tools suggest that for full coverage films the sulfur atoms of thiols form a  $(\sqrt{3}\times\sqrt{3})R30^\circ$  unit cell corresponding to a molecule-molecule spacing of 5 Å and an area per molecule of 21.6 Å<sup>2</sup> as depicted in **Figure 3 A**. Concluded from the results of FTIR and GIXD [17,16,27,28], the alkyl chains exhibit a twist angle ( $\Psi$ ) of about 52° defined by the zig-zag of the carbon atom structure in the chain and are tilted 14° away from the direction of nearest-neighbor ( $\phi$ ) with a tilt of 30° from the surface normal ( $\theta$ ). The corresponding angles are depicted in **Figure 3 B**.

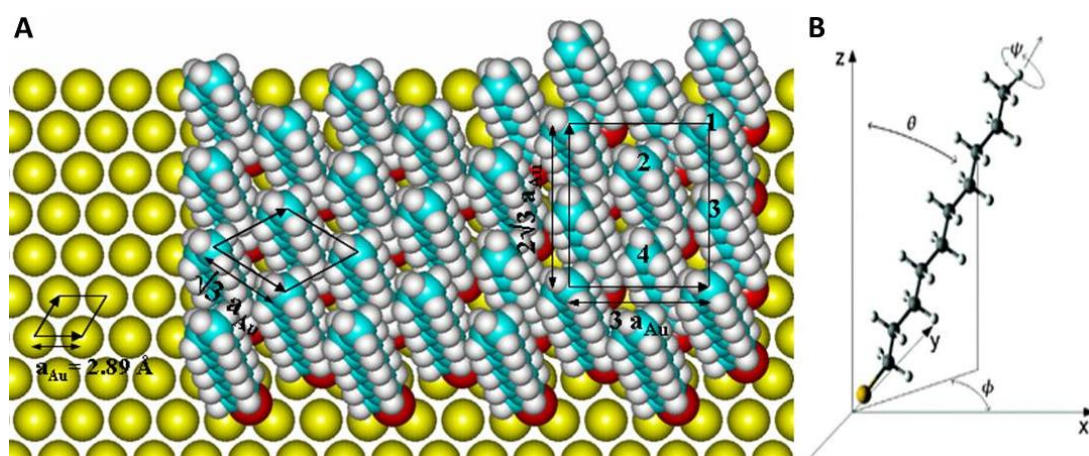


**Figure 3.** A) A model showing the structure of monolayer and the primitive unit cell (small oblique) of the Au(111) surface. The rectangular unit cell shows the  $c(4\times 2)$  or  $(2\sqrt{3}\times 3)$ rect superstructure (rectangle), while the large oblique unit cell shows the  $(\sqrt{3}\times\sqrt{3})R30^\circ$ . B) Schematic of angular degrees of freedom of alkanethiol.  $\theta$  is tilt angle from normal of surface,  $\Psi$  is twist angle and  $\phi$  projection of molecule in substrate plane.

Earlier calculations done for the alkanethiol-gold bonding were pointing to 3-fold hollow site with hcp packing (**Figure 4**) to be the most stable site for adsorption of thiols on Au(111) with bond energy of about 100 KJ/mole. [29] However, diffraction patterns suggest that 2 of the 4 molecules in the  $c(4\times 2)$  unit cell are distinct to a certain extent. Initially, it was thought that this secondary structure was caused by various

reasons including twist angles of the alkyl chains, different tilt angles and/or nonequivalent adsorption sites. [30–32] Therefore, it was logical to investigate short alkanethiols (eliminating/minimizing intermolecular interactions) and methylthiol was expected to have pure  $(\sqrt{3}\times\sqrt{3})R30^\circ$  structure. Though, GIXRD and LEED results confirm formation of  $(\sqrt{3}\times\sqrt{3})R30^\circ$  structure for methylthiol [33], some scattered reports on formation of a  $(3\times 4)$  phase were also published. [34,35] The  $(3\times 4)$  structure indicates two sulfur atoms to be bonded to gold adatoms at both high coverage and low coverage at room temperature (in HUV or air). [36–38] That is, formation of RS–Au–SR species which is commonly known as the staple motif takes place on the gold surface (the structure of these species will be discussed in section 1.5.3.1). [39,40] Later, this structure also was also observed by using helium diffraction and LEED. [41] It is worth to indicate that  $(3\times 4)$  structure was also observed for ethanethiol SAMs as well as propylthiol monolayers. [40,42]

Determination of sulphur -gold interface structure for long chain alkanethiol SAMs is, however, a real challenge, since the interface is buried beneath the long molecular backbone which inhibits direct observation (of the interface) by scanning probe techniques. The challenge still exists for theoretical calculations, since different structural models have similar energy and a key role may be played by intermolecular interactions between the alkyl chains. These kinds of interactions make density functional theory (DFT) calculations more complicated. Utilizing grazing incidence X-ray diffraction (GIXRD) the structure of a hexanethiol (HT) SAM was investigated in UHV on Au(111). The formation of vacancies and adatoms on topmost layer was confirmed by best fitting condition for proposed structural model. Derived structure of HT from this model consists of one dimensional staple motif –S–Au–S–Au–S– as well as thiols adsorbed on a bridge site. [43] This one dimensional chain structure was also observed on several thiol-protected gold clusters. [44–46] According to this model, both adatoms and vacancies are delocalized, which represents the dynamic character reflected by DFT based molecular dynamics simulations. These observations (formation of adatoms and dynamic character of interface) are consistent with creation

of vacancy islands ("etch pits" which will be discussed under the title of "defects in alkanethiol monolayers" in section 1.3.2) on thiol modified gold surfaces. [47]

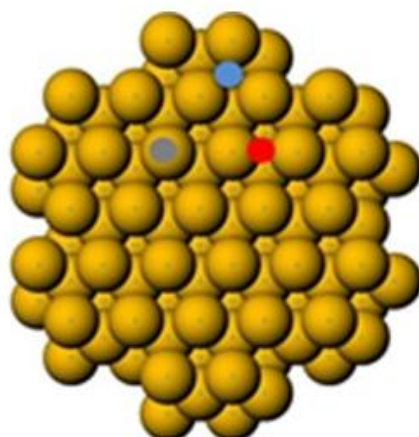


**Figure 4.** The different absorption sites on Au(111). Grey dot represents "top" site, red dot indicates a bridge site and blue one corresponds to a hollow site (hcp or fcc).

SAMs, in particular those that are formed by sulfur-containing organic molecules with alkyl or functionalized alkyl backbone, possess a well-ordered and close-packed surface structure and high stability. In addition, it is easy to control the surface properties by introducing various functional groups at the terminals of the monolayers. Therefore, extensive studies have focused on these functionalized thin films. Toward exploring more on the subject, the packing arrangement of SAMs formed by HS-(CH<sub>2</sub>)<sub>n</sub>-X molecules with X ≠ CH<sub>3</sub> have been scrutinized. The tilt angle of the HS-(CH<sub>2</sub>)<sub>16</sub>-OH molecules adsorbed on Au(111) as well as monolayers composed of alkanethiols with COOH end-group have been studied. The former's tilt angle is determined to be ranging over 28° to 44° as a result of numerous studies based on different techniques. [48,49] In fact, Poirier et al. found a commensurate lattice with an oblique primitive unit cell of dimensions  $a = 3a_{\text{Au}}$ ,  $b = 13a_{\text{Au}}$  (with  $a_{\text{Au}} = 2.88 \text{ \AA}$ ), and a packing density of  $21.5 \text{ \AA}^2$  per molecule. [50] The average tilt angle for the latter is 32° as determined using IR. As concluded from NEXAFS data the strong interaction of the COOH end-groups via hydrogen bonds causes alkylthiols with COOH termination to be largely disordered and to exhibit a high density of gauche defects which might forbid the formation of well-ordered films. [51]

Different groups' investigations of thiol adsorption kinetics onto Au(111) using different analytical techniques including ellipsometry and helium diffraction mostly suggest a two-step kinetic model for alkanethiol film formation:

- (a) A fast initial adsorption step with a time scale of minutes during which 80-90 % of the monolayer is formed.
- (b) A slow adsorption step with a time scale of hours or even days during which the monolayer undergoes orientation ordering resulting in complete film formation. The phase in which the molecules form highest density packing arrangement (the surface is saturated) is referred to as full-coverage phase. [52,7]

The need for molecular level information about localized and heterogeneous events during the self-assembly process was felt mainly because diffraction and spectroscopic studies provide only spatially averaged information of adsorption process. The reaction mechanism and kinetics of the self-assembly of thiols onto Au(111) from the vapor phase and from the solution (in-situ) have been investigated and well interpreted using scanning tunneling microscopy (STM) and atomic force microscopy (AFM). Two-step mechanism for film formation was confirmed as a result of these studies from molecularly resolved STM images. Lying-down or striped phase with molecular axis being parallel to the Au(111) forms in the first step when thiol molecules adsorb as depicted in **Figure 5 i-ii**. A first-order Langmuir adsorption isotherm precedes the growth of the lying-down phase. In the final step, densely packed domains (standing-up phase) is obtained after a two dimensional phase transition at near-saturation coverage consisting of certain intermediate structures (**Figure 5 iii**). At the end of this stage, molecules are oriented with their molecular axis nearly perpendicular to the surface (**Figure 5 iv**).

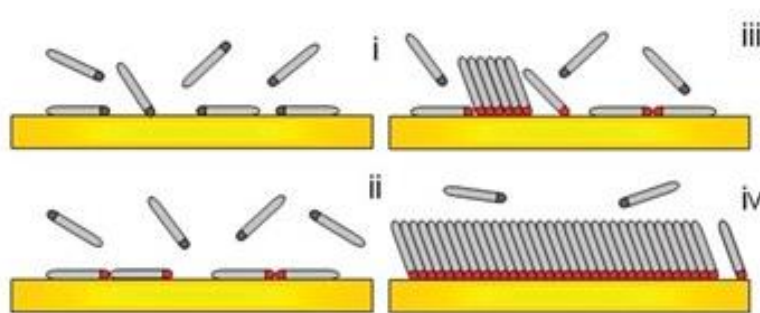


**Figure 5.** Scheme of the different steps taking place during the self-assembly of alkanethiol on Au(111): (i) physisorption, (ii) lying down phase formation, (iii) nucleation of the standing up phase, (iv) completion of the standing up phase. Retrieved from ref [52].

### 1.3 Defects in self-assembled monolayers

Defects in the monolayer can be extrinsic (such as contamination or impurities of molecules) which are not the subject of this work whereas intrinsic defects which can be tailored are discussed in upcoming sections.

#### 1.3.1 Defects in substrate

Polycrystalline gold is used in much of the work with SAMs. In spite of lower surface energy of these substrates leading to strong (111) texture, gross structural defects of varying densities exist. The nature of the gold surface determines the quality of the monolayer, hence, defects within the monolayer are affected by substrate defects. Pinholes, step edges, and grain boundaries are some examples of the metallic substrate defects (**Figure 6 A** depicts these defects indicated with black, blue and red arrow respectively). Because of defects in the underlying metallic surface, it is not feasible that films adsorb on these sites of substrates and form well-ordered structures. In other words, these defects distort favorable lateral interaction of adsorbents which reduce the film quality. [53,54]

### 1.3.2 Defects in the monolayer

Commensurate adlayer is affected not only by imperfections in metallic structure but also by defects in the monolayer. These defects are not desirable since defects negatively affect the electronic properties and quality of the modified interface. The major defects within monolayers are domain boundaries, collapsed sites and etch pits. These defects impair formation of crystalline film and result in incomplete adsorption of molecules. At any defect site, less ordered monolayer structures are formed because of distorted lateral chain-chain interactions.

The self-assembly of thiols follows a nucleation mechanism in which small groups of molecules grow into structured domains. Two adjacent well-ordered domains meet at a region which is called a domain boundary. **Figure 6 B** shows the grain boundary by blue arrow. The lateral interactions are disrupted at the domain boundaries since it is not definite that two domains are oriented in the same direction. When orientation of one domain morphs into a second positional orientation the resulting boundary is referred to as rotational domain boundary. Much like at domain boundaries, along the interface where neighboring alkanethiol molecules are not ordered, there are regions of low thiol concentration which are called collapsed sites. Thiol molecules at well-ordered domains protect the surface to a higher degree than the thiol molecules at collapsed sites. Electrochemical properties of monolayer –modified electrodes are affected by collapsed sites because the films are thinner at collapsed sites than at thiol-rich domains and hence, molecules in the solution can approach the electrode surface at a shorter distance. [55,56]

Lastly, one or two gold atom height imperfections are called vacancy islands or etch pits which are shown by the red arrow in **Figure 6 B**. This type of defects forms due to reconstruction of the gold layer during assembly process of alkanethiols and are filled with corresponding SAMs. It is worth to indicate that this type of defect is an intrinsic property of SAMs and could not be eliminated. [55,57]

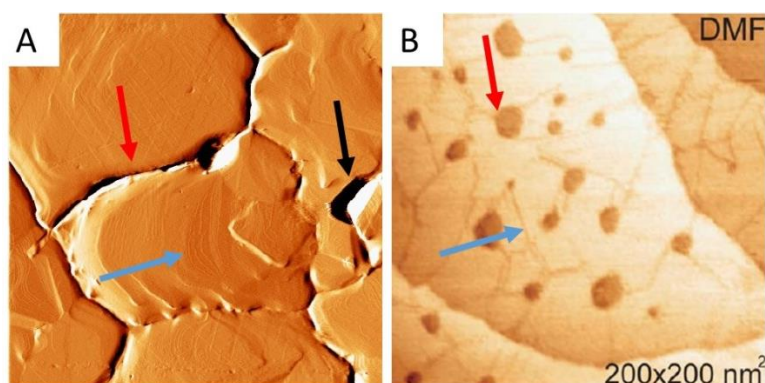


**Figure 6.** A) Tapping mode AFM image of single crystal Au(111) surface of  $2\ \mu\text{m} \times 2\ \mu\text{m}$ . The black arrow shows a pinhole whereas red one shows a grain boundary. The blue arrow shows step edges. Retrieved from ref [53] . B) STM image of octanethiol SAM on gold surface. The red arrow shows a vacancy island and blue arrow shows a grain boundaries of SAM. Retrieved from ref [56].

#### 1.4 Types of substrates for SAM growth

Smooth metal substrates are usually used to fabricate SAMs. Types of substrates can be planar surfaces (glass or silicon slabs coated with thin metal films or single crystals) or highly curved nanostructures (colloids, nanocrystals, nanorods). [58,59] Planar substrates are used widely for characterizing the structure-property relationships of SAMs. They are convenient (easy to prepare) and compatible with a number of techniques for surface characterization such as reflection absorption infrared spectroscopy (RAIRS), Raman spectroscopy, X-ray photoelectron spectroscopy (XPS), near edge X-ray absorption fine structure spectroscopy (NEXAFS), helium atom scattering, X-ray diffraction, contact angle (CA), optical ellipsometry, and scanning probe microscopy (SPM). Other metallic nanostructures, such as nanoparticles also can support SAMs, and these systems have been characterized by many techniques including electron microscopy, SPM, edge X-ray absorption fine structure spectroscopy (EXAFS) and X-ray absorption near-edge spectroscopy (XANES). In this work all SAMs were prepared on planar surfaces, hence in the following section, discussion will be on this type of substrates. The self-assembly

process of alkanethiols on planar metal substrates depends on a number of parameters that include; the chain length, degree of order, and topography/roughness of the substrate (as discussed before). Therefore, the structure and properties of SAMs significantly depend on the substrate. Acquiring detailed information on the interfacial processes necessarily implies the use of well-defined metal surfaces. Hence, most of the research aiming at providing a deeper understanding of interfacial processes such as adsorption, film formation and kinetics deal with single crystal surfaces (instead of polycrystalline ones) in UHV. [60,61]

#### 1.4.1 Single crystal gold films

Metal single crystals are very frequently used in traditional surface science, and they constitute well-defined substrates. Moreover, they offer the possibility to freely choose the crystallographic orientation. The Au(111) single crystal surfaces can be prepared by sputtering with 1 keV Ar ions and annealing at 500 °C repeatedly until a clean surface is obtained in UHV. [62] The clean gold surface is not only identified by the lack of surface contaminations, but also by the well-known  $(22\times\sqrt{3})$  reconstruction. [62,63] SAMs of thiol-functionalized molecules on single-crystal Au(111) surfaces have been studied by numerous groups since their discovery. For example, the transformation of alkanethiols between  $(\sqrt{3}\times\sqrt{3})R30^\circ$  and  $c(4\times 2)$  structures have been confirmed by STM on single crystal surfaces as depicted in **Figure 7**. [64]



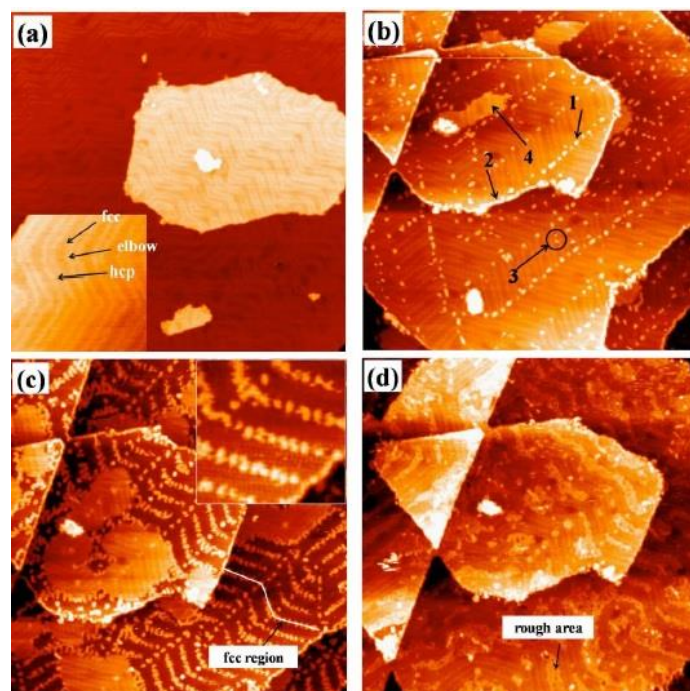


**Figure 8.** (a) STM image with size of 200 nm x 200 nm. The clean Au(111) surface. Inset arrows indicate the FCC and HCP stacked regions and the elbow sites. (b) STM image showing the surface at the early stage of adsorption with size of 150 nm x 150 nm. Arrow 1 indicate molecules at an elbow site; arrow 2 shows molecules at a step edge; arrow 3 shows molecules within the FCC region; arrow 4 shows a dense molecular island. (c) STM image (150 nm x 150 nm) indicates selective population of the FCC stacked regions by well-spaced molecules. (d) STM image (150 nm x 150 nm) shows the completion of the first molecular layer. The herringbone reconstruction could be observed through the molecular layer. All images were obtained at 120 K. retrieved from ref [37].

### 1.4.2 Polycrystalline gold films

Particularly for thiols on Au(111), in many cases evaporated Au films have been employed since preparation of single crystalline Au is expensive and require rather complicated equipment. However, while evaporated Au films predominantly exhibit (111)-oriented terraces, as this is the lowest-energy surface of Au, the crystalline

quality, the number of non-(111)-oriented crystallites, the density of defects, etc. can vary substantially depending on the evaporation conditions, the thermal treatment and other parameters. [65] The criteria important for selecting the type of substrate and method of preparation depend on the application for which the SAM will be used. For example, polycrystalline films are sufficient for many applications on planar substrates such as etch resist templates for crystallization, and model surfaces for biological studies because a wide range of materials can be deposited easily and these substrates are inexpensive relative to single crystals. Other applications, such as measurements of electron transport through organic molecules, benefit from substrates that are single crystals or polycrystalline films with minimal grain boundaries called pseudo- “single crystal”.

Polycrystalline gold films which were shown to be polycrystalline with a predominant (111) orientation, can be prepared by thermal evaporation of 20-300 nm of gold onto mica as well as silicon wafer or glass. [66–68] **Figure 9** shows AFM image of a thermally evaporated film and its corresponding line scan. Root mean square (RMS) roughness of the film is high, therefore, it is not possible to do a molecular investigation on this substrate. Smooth surfaces can be produced by other methods of substrate preparation from evaporated Au films. Ultra Flat Gold Surfaces, RMS roughness of which ranges from 0.3 to 2 nm, are often prepared by means of flame-annealing and template stripping methods. The discussion in the following sections will give more information about these procedures.

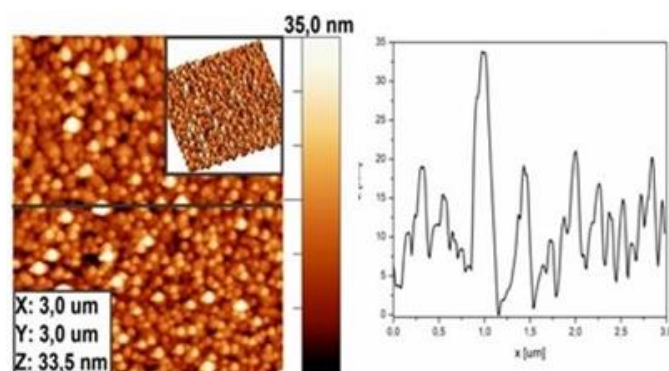


**Figure 9.** Thermally evaporated gold on Mica and corresponding line scan. Retrieved from ref [66].

### 1.4.3 Flame annealing

History of flame-annealing of polycrystalline gold goes back to long time ago. To homogenize the material and/or exclude gas inclusions, jewelers used to anneal gold. Annealing reduces crystallographic defects and introduces smoothness and epitaxy on the surface of films, foils or wires. As a result of thermal annealing of metal films larger grains are produced because of diffusion of grain boundaries. [69–73] During annealing process flame temperature is not uniform over all the regions. As a matter of fact, the flame temperature radially decreases therefore, size of terraces varies from hundreds of nm to some microns while the surface roughness is maintained below 1nm. Flame annealing procedure is mostly applicable to freshly evaporated gold film which interact with air or solvents minimally. Delamination induced by rapid vaporization of water which slowly intercalates between the gold and the substrates (mica, silicon or glass) upon exposure to air seems to be the reason for failure in flame annealing of hours old films. [74–76] **Figure 10 A** and **B** represent AFM image of freshly evaporated and flame annealed gold respectively. [77]

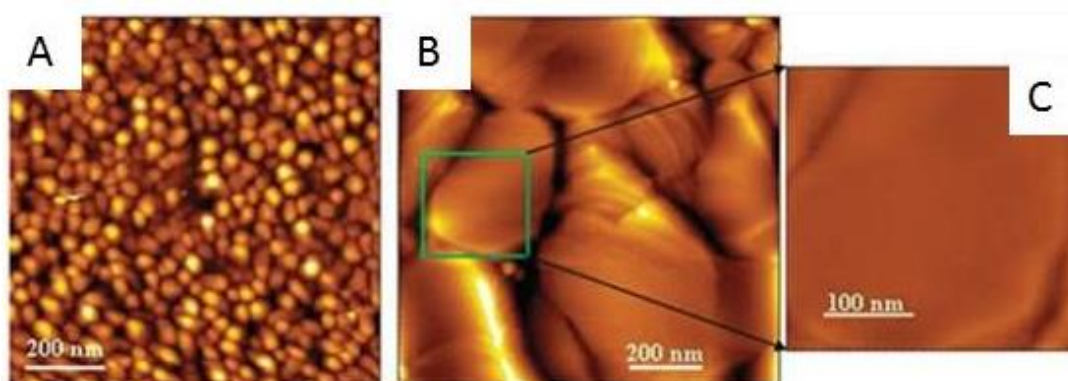


**Figure 10.** A) AFM image of thermally evaporated gold. B) Hydrogen flame annealed gold. C) Cross-section area from green square in (b). Retrieved from ref [77].

#### 1.4.4 Template stripping

Template stripping is another technique in which surface of a metal film deposited on silicon wafer or mica is glued, and then the metal film is peeled from the wafer to expose the surface that had been in direct contact with the substrate. This technique generates surfaces with roughness below 1 nm which is governed by the roughness of the substrate surface on which the gold film is grown. A method reported by Chen et al. and commonly referred to as “remote mechanical annealing” is used in fabrication of ultra-flat Au surface with low RMS roughness of nearly 0.2 nm. [78] Compared to commonly use direct deposition methods, surfaces obtained from template-stripping method are dominated by large smoother grains on which SAMs can pack well and containing only small areas of exposed grain boundaries. In **Figure 11**, one can observe preparation of an ultra-flat surface using gold in the process of template stripping. To produce a homogeneous ultra-flat gold surface, a thin gold film is deposited onto the smooth template (mica or silicon) surface by thermal evaporation or sputtering. Usually a rough gold surface is obtained after this stage. Next, to attach a solid support (often a glass slide) an adhesion layer which is usually thermally curable epoxy resin, is added on top of the gold surface. Lastly, at the Mica-Au or Si-Au interface, a cleavage occurs due to the mismatch between gold and the template material when the sandwich structure is mechanically cleaved at the point of weakest adhesion. [78–81]

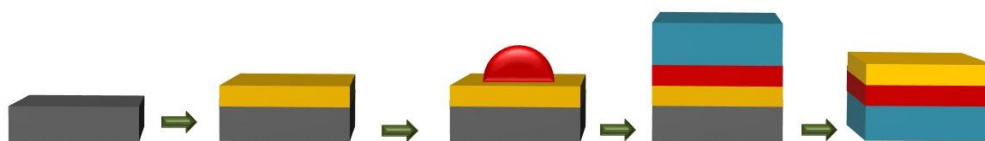


**Figure 11.** Automatically flat surface preparation by template stripping procedure.

Wagner et al. [80] made a survey of glues and developed protocols for the successful application of Panavia 21 (dental adhesive) and Cerastil C7 (inorganic adhesive) as well as epoxy based glues (Epo-tek 301-2 and Epo-tek 377). In case of epoxy resins, gold-deposited mica sheets were glued gold face down onto silicon wafer or glass and

cured. However, in case of inorganic adhesives additional adhesive mediators are required to improve stickiness of gold to supporting substrates. Representative STM image of template stripped (TS) gold produced by above-mentioned glues is depicted in **Figure 12** (mean roughness values are provided in the figure). In whole, all substrates have high quality and comparable roughness relative to the upper surfaces of epitaxially grown gold. The inorganic adhesives (that is Cerastil C7 and Panavia 21) are inert against moderate acids as well as to all organic solvents and alcohols, whereas epoxy based TS gold surfaces swell in chloroform and acetone after several hours. However, epoxy based TS is economically beneficial and applicable for visible light transmissive applications.

When compared to commercially available Au(111) substrates or flame annealed substrates with atomically flat gold terraces, template stripping yields substrates of arbitrary large areas of flat surface which are limited only by the dimensions and quality of the template material (silicon or mica). In addition to being atomically flat, they are also smooth and amorphous without any terraces or steps as shown in **Figure 13 A**. However, in some cases pinholes could be seen to form in TS gold which is correlated to imperfections during thermal evaporation of gold on the substrates as depicted in **Figure 13 B**. [81]



## 1.5 Characterization of thiol SAMs

There are many surface sensitive techniques to characterize SAMs topography, structure and composition such as STM, AFM, FTIR and diffraction of electrons, x-rays and helium atoms. Moreover, global properties of SAMs can be characterized by means of contact angle (CA) and ellipsometry. In this work, three common techniques were utilized to characterize these films and will be discussed in the upcoming sections.

### 1.5.1 Surface wettability

One of the most common methods to tune the wettability of metal surfaces is altering the end group of the SAMs. The wettability of the surface can be tuned by means of the hydrophobic and hydrophilic tails (end groups) on thiols. For example, the hydrophobic  $\text{CH}_3$  end group increase the hydrophobicity of the surface (greater than  $90^\circ$ ), whereas  $\text{COOH}$  or  $\text{OH}$  end groups make the surface hydrophilic. Hence, the surface wettability can be tailored by changing the polarity of interface which have interaction with commonly used probe (water). To further tuning the surface wettability, distinct molecules can be co-deposited simultaneously. By controlling the surface coverage of these molecule desired wetting properties can be designed. **Figure 14** shows static CAs of various end groups. In **Figure 14**  $\text{R}_1$  denotes a  $\text{SH}-(\text{CH}_2)_{11}$  group and  $\text{R}_2$  corresponds to  $\text{HS}-(\text{CH}_2)_2(\text{CF}_2)_5$ . [82] The most hydrophobic surface is fluoroalkyl one, whereas, hydroxyl or carboxyl terminated SAMs shows zero angle. The data point labelled as 7 in this graph represents the co-deposited hydroxyl and carboxyl terminated SAM which has a CA value between methyl and hydroxyl terminated SAMs. [83–86]

Besides the chemical structure of alkanethiols, nature of substrate also influences the surface wettability. Surface roughness plays a crucial role in static and dynamic CAs. The impact of the surface quality on surface wetting properties can be rationalized by considering odd-even effect (the odd or even number of carbon on chain). Thuo and

his coworkers investigated alkanethiol SAMs with structure of  $S-(CH_2)_nCH_3$  (where  $n=9-17$ ) on two distinct substrates with different roughness (thermally evaporated gold and template stripped gold with RMS roughness of  $2.27 \pm 0.16$  nm and  $0.36 \pm 0.01$  nm respectively). They observed a zigzag trend in static CA as the number of carbons in the chain increased from 9 to 17, on smooth metal surface. However, such a trend was not seen on rough deposited gold surface. The surface roughness and CA of corresponding alkanethiols are shown in **Figure 15**. These results support their ideal model (in which there is no gauche rotation) on ultra-flat surfaces. In their proposed model the conformation of the end group (hence dipole of surface) result in such a zigzag oscillation as shown in **Figure 16**. Also the increase in CA value with increasing number of carbon atoms was attributed to enhancement in the crystallinity of the SAMs. [87,88]

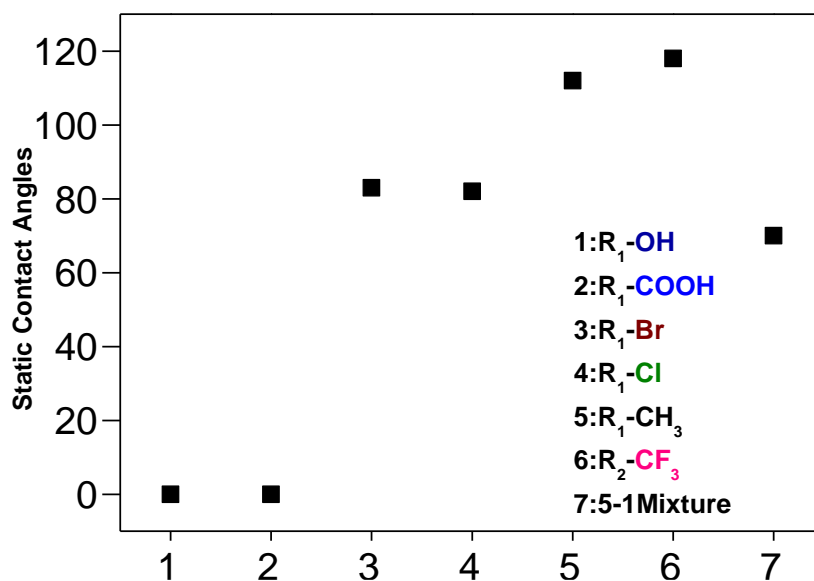


**Figure 14.** Static contact angle of various SAMs on Au(111).

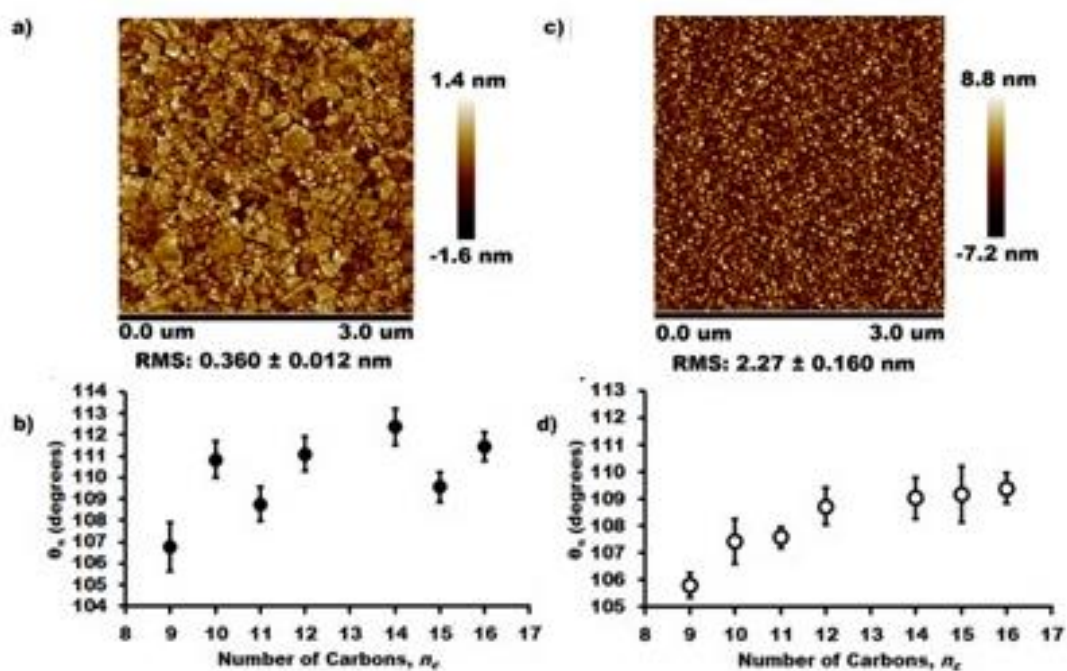


**Figure 15.** a) AFM image of template stripped gold. b) Contact angle of alkanethiols on template stripped gold. c) AFM image of thermally evaporated gold on mica. d) contact angle of alkanethiols on thermally evaporated gold. Retrieved from ref [87].

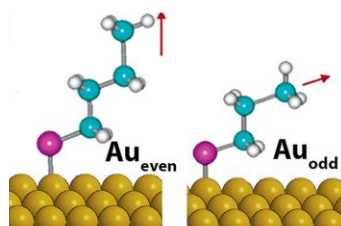


**Figure 16.** Model representing end group conformation of even and odd carbon containing alkanethiols. Retrieved from ref [87].

### 1.5.2 Thickness Characterization via Spectroscopic Ellipsometry

The thickness of thin-films can be measured by means of spectroscopic ellipsometry. [82,83,89,90] Operations in ambient conditions as well as non-destructive nature of characterization are the two main advantages of ellipsometry. This useful characterization tool is widely used for measuring the thickness and coverage of SAMs. As an example, Yasuhiro et al. have studied fluorinated alkanethiols and non-

fluorinated analogues which have structure of  $\text{CF}_3(\text{CH}_2)_n\text{SH}$  and  $\text{CH}_3(\text{CH}_2)_n\text{SH}$  where  $n=9-15$ . As can be seen in **Figure 17 a**, as the number of carbon on the backbone increases the thickness increases systematically. [82] Since the length of the molecule and thickness of SAMs on gold are different, the tilt angle of the molecules should be taken into account. **Figure 17 b** shows a model that is used for simple calculation of SAMs' thickness.  $L_0$  is the distance between gold surface and first carbon atom next to the sulfur atom. This thickness ( $2.8 \text{ \AA}$ ) is almost the same for all alkanethiol SAMs. Hence, the systematic addition of each carbon can be calculated from the equation below.

$$L_E = dn \cos(\alpha) + L_0 \quad \text{Equation 1}$$

Where  $\alpha$  is tilt angle,  $n$  is the number of carbon atoms,  $d$  is the length of the projection of the C-C bond onto the backbone of chain and  $L_E$  is the ellipsometric thickness.

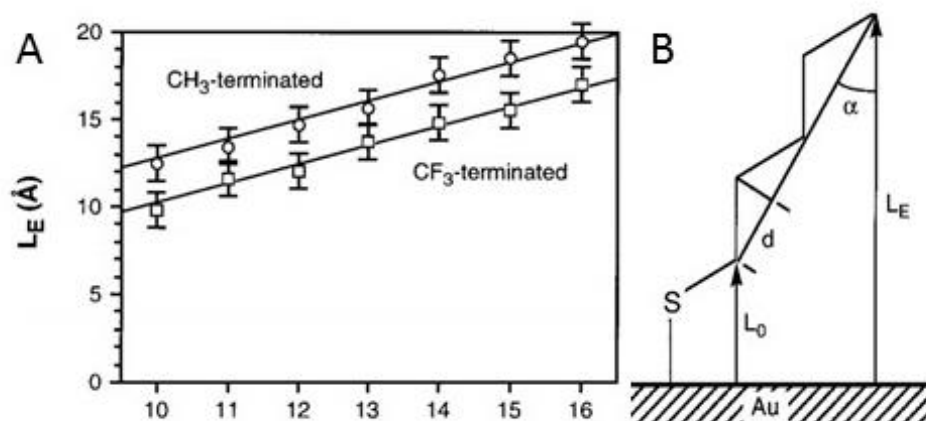


**Figure 17.** a) Ellipsometric thickness of SAMs. Line indicates calculated thickness by the equation. b) Schematic representation of relationship between the components of the equation. Retrieved from ref [82].

### 1.5.3 Scanning Probe Microscopy

SPM (scanning probe microscopy) techniques are used to characterize local properties of non-periodic or periodic structures with molecular and atomic resolution. STM

(scanning tunneling microscopy) and AFM (atomic force microscopy) are two versatile and common techniques of SPM which are used for real time imaging in ambient conditions as well as in UHV. The resolution of STM generally is better than AFM. However, for alkanethiols which contain more than 18 carbons in the backbone, it is difficult to get STM image because of unstable tunneling condition. Hence, AFM is more preferable than STM to get molecular resolution images of SAMs. In addition, AFM is usually used for micro scale topographic imaging for SAMs.

### 1.5.3.1 Scanning tunneling microscopy

STM is one promising tool to characterize films structure on gold. For example, the existence of a  $c(4\times 2)$  superstructure with respect to the basic  $(\sqrt{3}\times\sqrt{3})R30^\circ$  lattice on Au(111) was revealed for octanethiol by STM at saturation coverage (see **Figure 7**) Similar results can be seen for hexanethiol, dodecanethiol and decanethiol monolayers with same lattice structure. [91,92] Besides these, in recent years STM resolved some controversial concepts about film formation and nature of superstructures. For instance, atomic resolution STM image of striped phase (at 0.11MLcoverage) of octylthiol revealed head to head arrangement of molecules as shown in **Figure 18 A**. [93] However, this head to head structure of the striped phase brings up the question of “how the repulsive interaction of sulfur atoms allows formation of the film in this arrangement?”. In fact, formation gold adatoms and RS-Au-SR motif assists to explain this question. Insertion of gold atom between two sulfurs suppresses the electrostatic repulsion between them and promotes formation of striped phase. As discussed earlier (see section 1.2), recent studies show that short alkanethiols ( $\text{CH}_3(\text{CH}_2)_n\text{SH}$  where  $n=0,1$  and  $2$ ) form  $(3\times 4)$  lattice structure on gold surface. To shed light on the interface structure, methylthiol was investigated in HUV at low temperature and low coverage. STM results as well as diffraction studies in these conditions revealed that sulfur atoms of two methylthiol are joined by one gold adatom as depicted in **Figure 18 B**. [94] It is worth noting that there are trans and cis conformations of  $\text{CH}_3\text{S-Au-SCH}_3$ . This kind of structure was also observed at full coverage of methylthiol as well as for ethanethiol and propylthiol monolayers. [36,93,95] As can be seen from **Figure**

**18 C**, at full coverage of these molecules only trans conformation exists. Guo and his colleagues also observed  $(3 \times 4)$  structure for propylthiol SAMs and explained how  $(3 \times 4)$  relate to  $c(4 \times 2)$  structure. [93] They discussed that for alkanethiol SAMs with  $n \geq 2$ , the van der Waals interaction plays crucial role in the structure of superlattice and force cis–trans isomerization. This kind of isomerization results in formation of  $c(4 \times 2)$  which is a superstructure of  $(\sqrt{3} \times \sqrt{3})R30^\circ$  as depicted in **Figure 18 D-F**. [95] The DFT calculations support these results as well. However, there is no solid experimental evidence against the standard  $(\sqrt{3} \times \sqrt{3})R30^\circ$  lattice structure of longer chain alkanethiol SAMs. Hence, more investigations are required to resolve sulfur-gold complex structure.

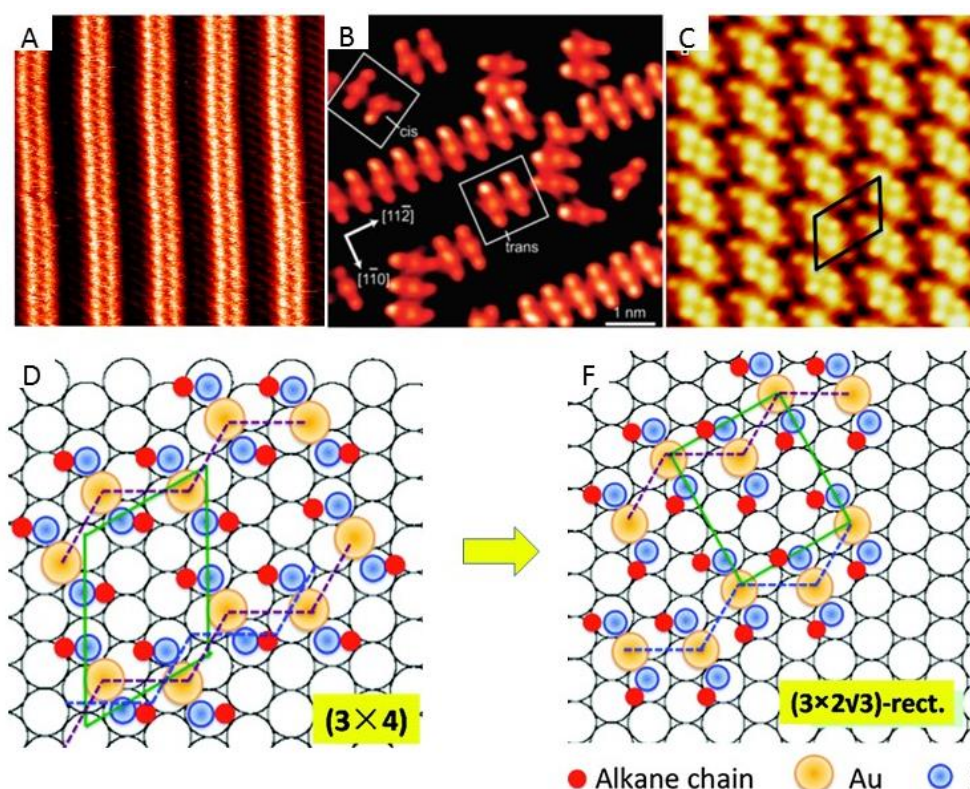


**Figure 18.** A) STM image of octylthiol SAM on gold with surface coverage of 0.11 (striped phase). B) STM image of methylthiol at low coverage The middle atom corresponds to gold adatom. As can be seen there is cis and trans conformation related to methylthiol. C) STM image of methylthiol at full coverage. The proposed relationship between  $3 \times 4$  structure (D) and  $c(4 \times 2)$  phase (F) is also shown. Both have

zig zag structure. As the length of alkane chain increases interaction of chains increases as well, resulting in the more ordered trans structure. Retrieved from ref [36,93–95].

### 1.5.3.2 Atomic force microscopy

AFM can also be used to characterize thiol films. [96,97] **Figure 19 a** shows a bare Au(111) surface structure in atomic resolution. **Figure 19 b,c** and **d** reveals lattice structure of octadecanethiol, decanctiol and hexanethiol, respectively. Clearly  $(\sqrt{3}\times\sqrt{3})R30^\circ$  lattice on Au(111) can be deduced from these images.

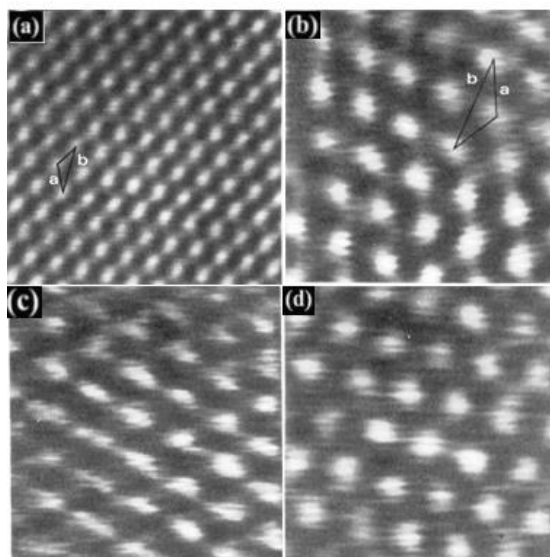


**Figure 19.** a) AFM image of bare Au(111) with hexagonal structure. b) AFM image Octadecanethiol on gold surface. Hexagonal structure of SAM is shown by vectors. c) AFM image of decanctiol. d) AFM image of hexanethiol. Retrieved from ref [96].

It is worth to discuss time dependent domain formation of alkanethiols on Au(111) surface. Tamada and his coworkers investigated domain formation of partially and fully covered Au surface by controlling time of immersion in ethanolic solution of butanethiol ( $C_4H_9SH$ ), dodecanethiol ( $C_{12}H_{25}SH$ ) and octadecanethiol ( $C_{18}H_{37}SH$ ) by AFM. [98] By comparing AFM images with same time of immersion they concluded that as length of alkanethiol increases diffusion of the molecules decreases, hence

shorter chains cover the surface in shorter time. For example AFM image of butanethiol SAMs are shown in **Figure 20** which demonstrate the change in coverage with changing immersion time. After 3 min immersion, full coverage was observed whereas after 10 seconds only a partially covered surface was observed.

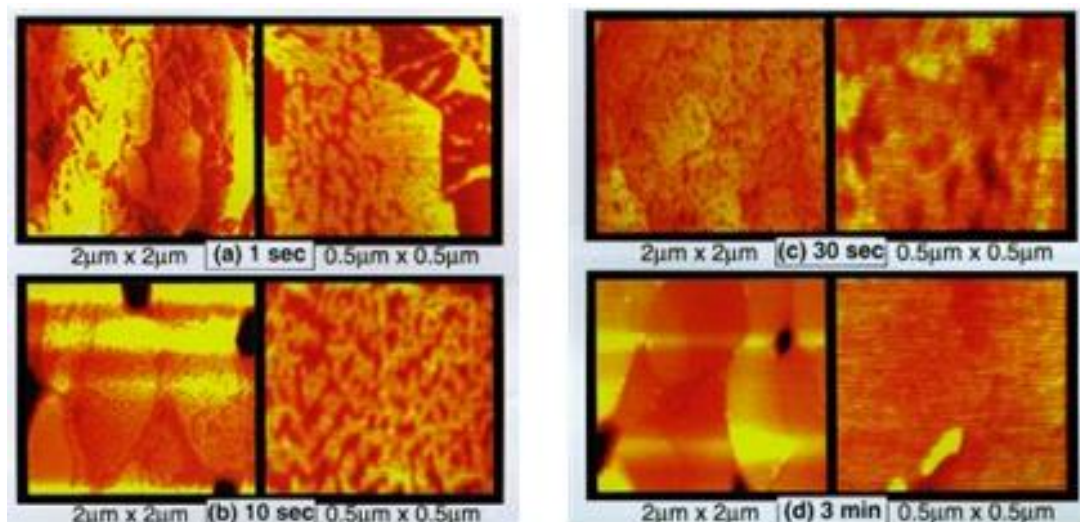


**Figure 20.** AFM images of butanethiol at different time of immersion in 1mM solution. a) 1 second. b) 10 seconds. c) 30 seconds. d) 3 minutes where surface covered completely. Retrieved from ref [98].

One interesting and promising way to systemically alter surface properties is to use mixed SAMs. The properties of metal surfaces such as wettability and work function can be tuned by varying tail group and chain length. For example, mixed SAMs of butanethiol/octadecanethiol (with solution ratio of  $R_{soln} = 1/1, 10/1, 20/1, 40/1, 100/1$ ) was studied. 1/1, 10/1 and 100/1 mixed SAMs exhibit homogenous films without any domain formation due to phase separation. However, at  $R_{soln} = 20/1$  and 40/1 clear phase separation was observed as depicted in **Figure 21**. Octadecanethiol was observed as bright islands, while shorter butanethiol phases act as a sea matrix in which octadecanethiol grow from. In fact, this hypothesis was supported by difference of the domains height ( $\Delta d = 1.0-1.4$  nm) which is consistent with the difference of thickness of butanethiol and octadecanethiol (see **Figure 21**).

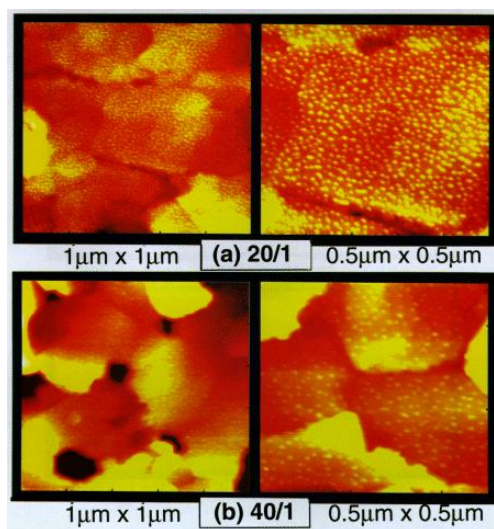


**Figure 21.** AFM image of butanethiol/octadecanethiol mixed SAMs. a) 20/1 .b)40/1. Retrieved from ref [98].

### 1.6 Utilizing SAMs for tuning work function of gold

Minimum energy needed in order to remove an electron from a solid to a point in vacuum immediately outside the solid surface is called the Work Function (WF). Presence of any adsorbates on the surface affects the WF of a metal. Based on observations from experiments WF is shown to be affected by physisorbed atoms of inert gases like argon and xenon. [99] Utilizing chemisorbed or physisorbed organic molecules on metals have greater impact on work function, however. Among thin films of organic molecules on noble metals, thiol-SAMs are employed extensively in semiconducting industry. There are two main advantages/possibilities that SAMs offer in tailoring work function of the metals:

- (a) Possibility of formation of monolayer films of high conformation degree ordering and exact orientation of molecular components within a well-defined array of molecules.
- (b) Possibility of shaping magnitude and direction of the surface dipole moments by modifying structure of molecular adsorbates.

In the upcoming section, the effect thiol-SAMs on gold substrate work function will be discussed in detail. When studying the relationship between WF and thiol SAMs, Evans and Ulman performed ellipsometry and Kelvin-probe measurements on a series of alkanethiol ( $\text{HS}(\text{CH}_2)_n\text{CH}_3$  with  $6 < n < 22$ ). Ellipsometry measurements confirmed formation of dense thiol-bound monolayers on gold implying an increase in the thickness of the monolayers with the alkyl chain length. They proposed that total dipole moment consists of two dipole sheets where monolayer/Au interface is considered as the first layer and monolayer end group/air interface as the second layer. The total dipole moment is sum of these two dipole sheets. They reported that work function of the metal decreased with a slope of  $-9.3$  meV per methylene group. As demonstrated in **Figure 22**, a model involving a dipole layer resting on top of the metal was used for interpretation of the situation. The reason for reduction in work function with respect to bare gold is due to dipole moment charge. Since positive tail of dipole moment stands on monolayer/air interface, a reduction of work function occurs. [100]

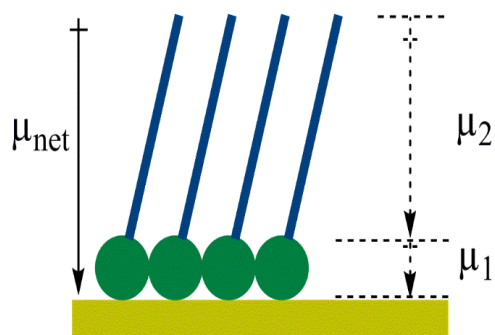


**Figure 22.** Schematic diagram of an alkanethiol SAM on gold. The organic adlayer can be envisaged as two layers of dipoles with dipole moments  $\mu_1$  and  $\mu_2$ . The net dipole moment,  $\mu_{\text{net}}$  is also shown.

The work function of metals can be tuned by changing the tail group of SAMs which results in changing the dipole moment direction and magnitude of molecules on the surface. The surface dipoles for fluorocarbon-terminated gold surfaces exhibit a polarity opposite to the surface dipoles associated with the hydrocarbon-terminated gold surfaces (i.e., those coated with n-alkanethiol SAMs). In other words, terminal fluoroalkyl raises the work function of gold (as much as  $0.75$  eV), whereas, n-alkane

terminated one decreases as much as 0.45 eV. (For more details about tuning work function by SAMs see APPENDIX section 1). [101–103]

### 1.7 Carboranethiol SAMs

Dicarbido-closo-dodecaboranes ( $C_2B_{10}H_{12}$ ), or carboranes, have three isomers depending on position of carbons in the cluster. The carbons separated by one or two boron atoms are referred as Meta (m) and Para (p) respectively and adjacent carbons in the cage is denoted as Ortho (o). Electron deficiency and bond delocalization in carboranes lead to pseudo-aromaticity of the borane cage which have typical aromatic reactivity. Advanced synthetic approaches in preparation of this compound offers substitution on both boron and carbon. These pathways propose thiolation of cluster at different positions about the three isomers which make carborane an auspicious compound for surface modification. For instance, o-carborane-1-thiol (O1), m-1-carboranethiol (M1) and m-9-carboranethiol (M9) are three thiolated derivatives of ortho and meta isomers. In case of M1 and O1 which are meta and ortho isomers of carborane, thiol group is attached to carbon. On the other hand, M9 which is meta isomer of carborane, the thiol group is attached to the boron. In our naming system the position of thiol groups is denoted by a number and the letters indicate the corresponding isomer. The structure of the above mentioned three compounds are shown in **Figure 23**.



diameters of these nano particles change from 2.8 to 12.3 nm. In second part of their study SAMs of (2), (3) and (4) was investigated on gold. The XPS results showed that sulfur 2p electrons of (4) have lower binding energy by 0.5 eV than (2). This observation was explained by electron distribution on boron and carbon vertexes. Boron atoms (at 9-12 position) have higher electron density relative to carbon atoms at 1-2 position. The lower electron density at carbon atom results in stronger binding of sulfur 2p electron. The SAMs of (3) shows two peaks corresponding to thiol bonded sulfur and thiol bonded sulfur (sulfur at 1 and 12 positions), however, the ratio of these peaks are not 1:1. The dominance of thiol suggests that some of carborane clusters were bonded to the surface from both thiol groups at step edges. The hydrophilicity and hydrophobicity of surface modified with carboranes was also compared to have an idea about the orientation of the molecules on surface. The static contact angle values of these films are depicted in **Table 1**. The most hydrophobic surface belongs to SAM of (2) due to from B-H nonpolar vertexes interacting with water. The SAM of (3) shows hydrophilic characteristics because of S-H group covered surfaces (S-H group oriented up ward) and SAM of (4) shows CA close to SAM of (3) because of acidic C-H.

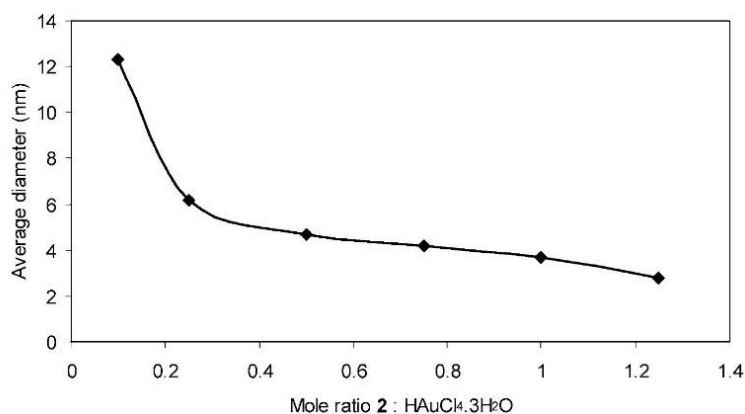


**Figure 25.** Gold nano particles size coloration with mole ratio carboranethiol (2) to H[AuCl<sub>4</sub>].3H<sub>2</sub>O. Retrieved from ref [104].

**Table 1.** Contact angle of Carboranethiol (2),(3) and (4) SAMs.

<i>SAMPLE</i>	<i>Bare gold</i>	<i>2-SAM</i>	<i>3-SAM</i>	<i>4-SAM</i>
<i>contact angle</i>	74°	88°	57°	53°

More comprehensive work was done by Weiss and coworkers on M1 and M9. The structure of these compounds are shown in **Figure 26 a**. As can be seen from **Figure 26 b** by altering the position of carbon atoms in the cage, dipole moment and its direction can be manipulated. [105]

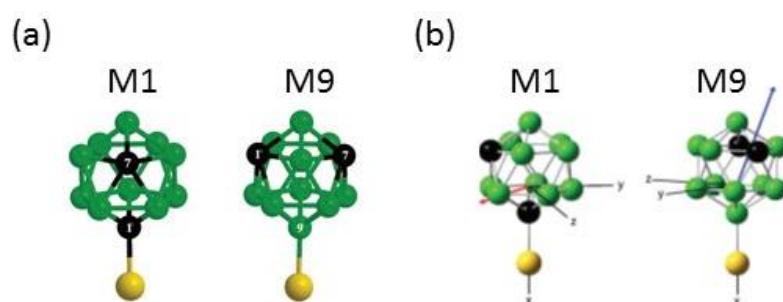


**Figure 26.** a) Chemical structure of m-1-carboranethiol (M1), m-9-carboranethiol (M9). b) Dipole moment direction of carboranes. The dipole moment vectors are pointing from negative pole to positive pole. Retrieved from ref [105].

By utilizing STM and CA measurements, they characterized SAMs of these moieties. STM results show that hexagonally close-packed M1 and M9 are indistinguishable with apparent height of  $9.8 \pm 0.3$  Å as depicted **Figure 27** (There is no discernible change in height or close packing structures, also it is worth to say that the height of carboranethiols was measured relative to 1-dodecanethiol from mixed SAM of carboranethiols and the alkanethiol). Fourier transformed STM image (inset in **Figure 27**) yields a nearest-neighbor spacing of  $7.2 \pm 0.4$  Å for both M9 and M1 SAMs. By considering the nearest-neighbor spacing and commensurate overlayer on gold, they concluded two possible unit cell structures as  $(5 \times 5)$  and  $(\sqrt{19} \times \sqrt{19}) R23.4^\circ$ . Moreover, STM images indicate defect (such as collapsed sites and etch-pits) free monolayer films since the full monolayer of these molecules show robust and well organized structure. In order to investigate importance of direction and magnitude of dipole moment on film properties, they performed DFT calculations, water CA, Kelvin probe

force microscopy (KPFM) and grazing incidence FTIR measurements. Using DFT in gas phase, dipole moments of M1 and M9 were calculated as 1.06 and 4.08 D, respectively. The directions of dipole moments are shown in **Figure 26 b**. In both cases the positive end of dipole moment vectors points between two carbons. In fact, this calculation explains higher acidity of M1 reported earlier. The acidity of thiol on carborane isomers was reported be  $pK_a=9.45$  and  $pK_a=5.30$  for M9 and M1, respectively. The relation of dipole moment direction and acidity was explained by stabilization of negative sulfur atom. In other words, the positive end of the dipole stabilizes the negative sulfur atom resulting in higher acidity of M1. Utilizing KPFM, work function of modified surfaces was shown to decrease for both carboranethiol isomers (M1 and M9). The reduction in work function upon M1 adsorption was measured as  $90\pm 20$  meV and  $480\pm 20$  meV in case of M9. These results are strong evidence of calculated dipole moment direction by DFT. As expected parallel dipole moment to surface normal (M9) have more effective impact on the work function than parallel dipole moment to surface (in case of M1). Also, positive pole of dipole moment pointing away from surface reduces the work function, while negative pole increases the work function. The assigned magnitude and direction of dipole moments explain the difference of hydrophilicity and stability of the SAMs. The CAs of the M1, M9 and co-deposited M1:M9, and 1-dodecanethiol (C12) were measured and are shown in **Table 2**. CA values of all carboranethiol SAMs are more hydrophilic relative to C12. M9 has smaller CA relative to less polar M1. The hydrophilicity of M9 SAMs was explained by relatively larger dipole moment than M1. However, co-deposition of M1 and M9 in different ratios suggests higher percent coverage of M1 on the surface. For example, M1 and M9 co-deposition from 1:3 solution ratio results in dominance of M1 (CAs are close to the M1). This fact can be correlated to dipole moment direction of M1. Since this molecule has dipole moment parallel to the surface, there is favorable interaction between dipole moments of M1 on surface in head to tail fashion which shows curial role of orientation of dipole moments in SAM properties. To support CA results, Grazing incidence FTIR spectra of M1, M9 and co-deposited M1:M9 were collected in range of 800 to 4000  $\text{cm}^{-1}$ . The B-H stretching peaks were

observed in 2500-2700  $\text{cm}^{-1}$  region. The distinct B-H stretching features were observed for M1 and M9 as depicted in **Figure 28 A**. The difference of spectra of the isomers are shown in **Figure 28 B** by overlaying the peaks. The peaks at 2585  $\text{cm}^{-1}$  which belongs to M1 were well resolved when the peaks were overlaid, hence this peak was chosen to analyse co-deposited samples (to have idea about relative coverage of isomers on surface by using relative peak areas). The coverage results that were concluded from this peak analysis are compiled in **Table 1**. In all samples, M1 was the dominant component in the film (even in 1:3 ratio of the M1:M9 in growth solution dominant compound in the SAM was M1). Hence, grazing incidence FTIR results justify their hypothesis that M1 molecules have head to tail dipole-dipole interactions.

**Figure 29** shows this interaction schematically.

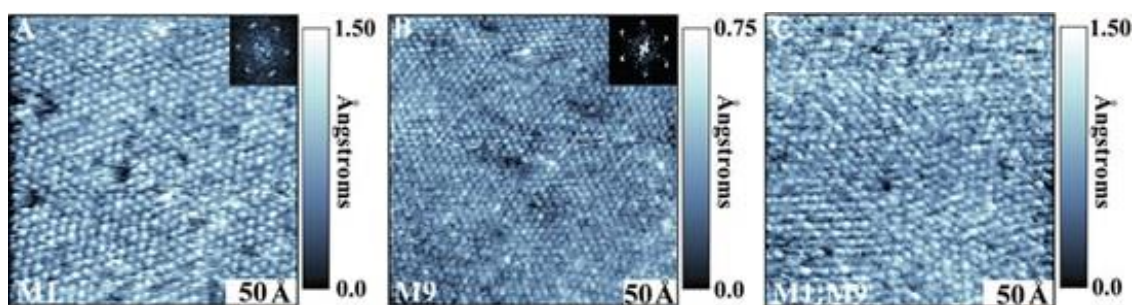


**Figure 27.** STM images of SAMs of a) M1. b) M9 and c) an adlayer prepared from a 1:1 solution on gold surface. Onset in a and b correspond to fourier transforms image A and B showing reciprocal lattice. Retrieved from ref [105].

**Table 2.** Contact angle of Carboranthiol of M1, M9 and M1:M9 mixed SAMs.

<i>SAMPLE</i>	<i>Contact angle (deg)</i>		<i>Hysteresis</i> $\Delta$
	<i>Advancing</i>	<i>Receding</i>	
<i>m-1-carboranethiol (M1)</i>	82±2	71±1	11±1
<i>m-9-carboranethiol (M9)</i>	72±4	52±1	20±4
<i>3:1 M1:M9</i>	82±1	67±1	15±1
<i>1:1 M1:M9</i>	82±2	66±1	16±1
<i>1:3 M1:M9</i>	82±1	68±1	14±1
<i>1-dodecanethiol (C12)</i>	107±1	97±1	10±2

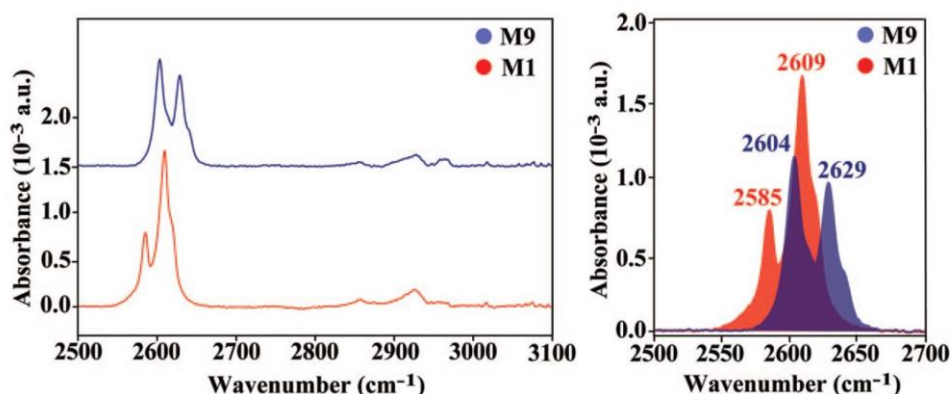


**Figure 28.** Grazing incidence FTIR spectra of M1 (red) and M9 (blue) on gold surface. The right figure shows the overlap of the M1 and M9. Retrieved from ref [105].

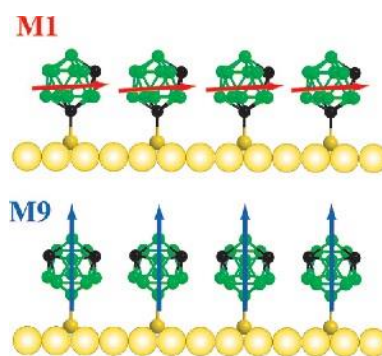


**Figure 29.** Head to tail dipole moment of M1 and perpendicular dipole of M9. Retrieved from ref [105].

Work function, film quality as well as the theoretical calculations show that electronic properties of metal substrates can be further improved by carboranethiol SAMs. In another paper published in 2014 by Weiss and his coworkers, they showed that Organic Field Effect Transistor conductivity can be improved by 2 orders of magnitude when the gold electrodes were modified by M1: M9 mix SAMs. To shed light on this work, the work function of SAMs was investigated comprehensively by Weiss and will be discussed below. [106] It is known that appropriate work function of metals in OFETs is crucial to facilitate charge transfer at the electrode. Besides, the compatibility of the electrode surface (metals) with the organic layer affects the performance of OFETs. Hence, by introducing carboranethiol SAMs on metal surfaces

not only work function can be tuned but also the compatibility of organic and inorganic interfaces can be enhanced. Therefore, Weiss group manipulated work function by employing M1 and M9 mixed SAMs. These isomers were chosen because of two main reasons: dipole moments of them are almost perpendicular and they have large dipole moment (the direction and magnitude of these isomers discussed earlier in this section see **Figure 26 b**). The tunability of work function was confirmed by UPS results as depicted in **Figure 30 A**. The SAMs were deposited from solutions of 3:1, 1:1 and 1:3 ratio of M1:M9 and resulting work functions were  $5.39 \pm 0.03$ ,  $5.25 \pm 0.03$ ,  $5.16 \pm 0.02$ , and  $5.01 \pm 0.05$  eV, respectively. As discussed earlier since M1 have head to tail dipole-dipole interaction the surface coverage of M1 is higher than M9. Hence, surface coverage of M1 and M9 is important and coverage of these moieties was calculated by using polarization modulation infrared reflection adsorption spectroscopy (PM-IRRAS) peak areas. By plotting work function against M1 surface coverage, almost linear increase in work function with increasing M1 surface coverage was observed. This correlation is depicted in **Figure 30 B**. Furthermore, surface wettability of these SAMs was measured by using two different probes (water and hexadecane). In all cases, hexadecane wets surfaces completely. When CA was measured by water, the observed trend is depicted in **Figure 31 A**. By decreasing M1 surface coverage CA decreases from  $85.8 \pm 1.1^\circ$  (100% M1) to  $77.7 \pm 0.8^\circ$  (100% M9). It is worth to emphasize that these CA results are not in agreement with the previous work of the Weiss group (the dynamic CAs in their previous work were shown in **Table 2**. Contact angle of Carboranthiol of M1, M9 and M1:M9 mixed SAMs.). In other words, the static CAs do not lie between dynamic CAs. The performance of OFET devices was evaluated by measuring on/off current ratios ( $I_{on}/I_{off}$ ). Current ratios of OFET devices constructed by using bare gold source/drain electrodes were measured as  $4.78 \pm 1.28 \times 10^3$  and the field-effect mobility was  $(1.67 \pm 0.51) \times 10^{-4} \text{ cm}^2 \text{ V}^{-1} \text{ s}^{-1}$  on average. Comparing this result with the result of gold modified electrode devices, it was concluded that M1 deposited on gold electrode enhances performance of the device to  $(4.53 \pm 1.19) \times 10^5$  and mobility to  $1.30 \pm 0.42 \times 10^{-3} \text{ cm}^2 \text{ V}^{-1} \text{ s}^{-1}$ . However, M9 coated electrode reduces device performance to an

on/off current ratio of  $1.68 \pm 0.62 \times 10^3$  and mobility of  $1.94 \pm 0.58 \times 10^{-5} \text{ cm}^2 \text{ V}^{-1} \text{ s}^{-1}$  as depicted in **Figure 31 A**. These results were explained through injection barrier between gold and organic layer. Bare gold and organic layer have significant hole injection barrier (about 0.25 eV) as shown in by **Figure 31 B**. Introducing M1 on gold surface reduces this barrier, hence performance increases exponentially. In contrast, M9 increases the barrier.

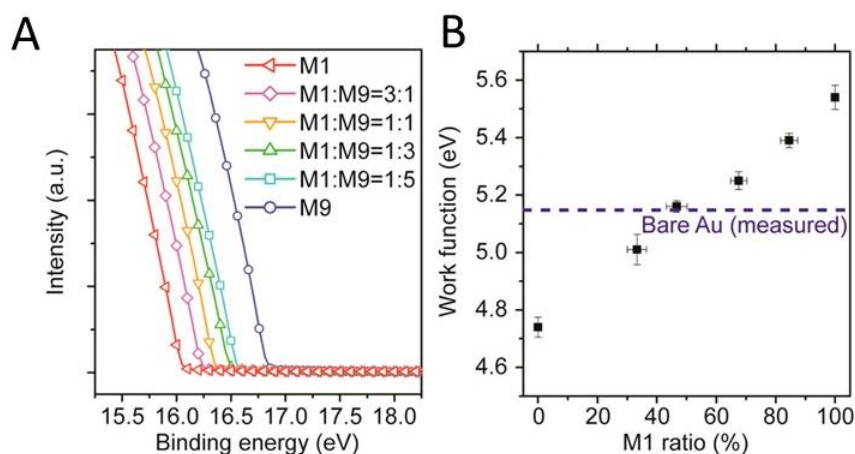


**Figure 30.** A) UPS spectra of Au surfaces decorated with pure or mixed SAMs. B) calculated work function of the gold surface covered by carboranethiols with respect to M1 mole fraction. Retrieved from ref [106].

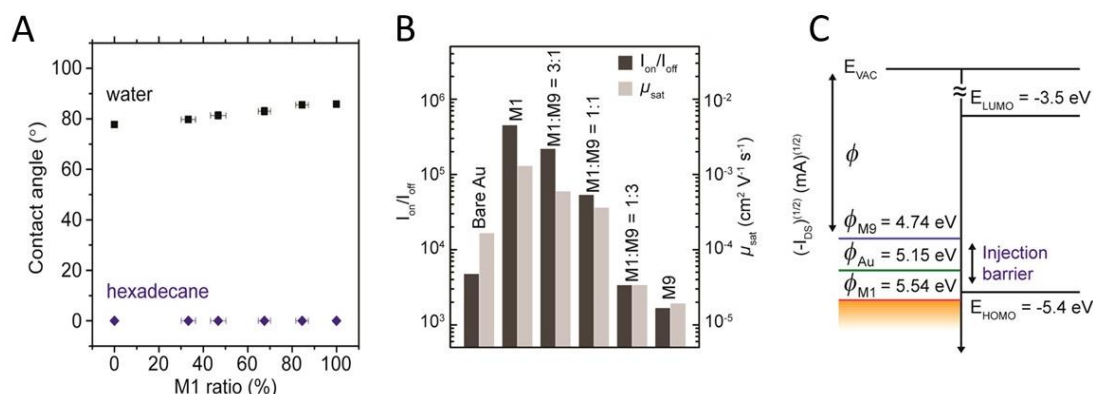


**Figure 31.** A) Water contact angle and hexadecane contact angle. Water contact angle shows direct relation to M1 ratio. In all cases hexadecane wets surface completely. B) Performance of OFET constructed by using bare and SAM decorated gold electrodes. M1 shows best result by reducing injection barrier. C) Schematic representation of the injection barriers. Retrieved from ref [106].

Theoretical calculations of super-lattice structure and dipole-dipole interaction of carboranes was further confirmed by Danişman and coworkers. [107] They calculated dipole moment and total energy of 8 different CT isomers in the gas phase by using both the standard PBE and modern vdW-DF functionals. The dipole moments were calculated as 1.78, 3.89 and 3.70 D for M1, M9 and O1 respectively. Also they showed 5x5 unit cell to be more stable than the ( $\sqrt{19}\times\sqrt{19}$ ) R23.4° unit cell and confirmed that M1 binds to the surface stronger than M9 due to dipole-dipole interactions. All of these results indicate that carboranethiol isomers have intrinsic molecular dipoles which enable to tune surface properties of Au by co-deposition of them without altering the geometry of the assembly. In addition, CTs are highly stable towards chemical, oxidative and thermal degradations which promote films quality significantly.

## 1.8 Motivation of the study

In this study our motivation was Weiss group's work, which shows that head to tail dipole-dipole interaction of M1 on surface affects the film properties significantly which were also confirmed by the theoretical calculations performed in our group. [105,107] To be able to reach a safe conclusion regarding the effect of dipole moment on the CT SAM structure and stability further studies are necessary in which the dipole moment is changed in a systematic way by using the appropriate CT isomers. To this end here in we studied the mixed SAMs of three CT isomers on Au(111) surface with dipole moment vectors parallel to the surface (M1 isomer), pointing above the surface (M9 isomer) and pointing towards the surface (O1 isomer), with magnitudes of 1.76, 3.87, and 3.66 D in the gas phase, respectively as shown in **Figure 32**. Since the direction and magnitude of these isomers are distinct, co-deposited SAMs are expected to have different properties relative to their pure SAMs. We systematically changed concentration ratio of the isomers in the growth solution to correlate their solution ratio to surface ratio and film morphology by means of wettability, ellipsometry and atomic force microscopy (AFM) measurements. All experiments were conducted on template stripped Au (111) surfaces in order to investigate the effect of surface roughness on film properties.





## CHAPTER 2

### EXPERIMENTAL

#### 2.1 Experimental techniques

In this section theoretical background regarding the working principles of the experimental techniques used in this study will be provided.

##### 2.1.1 Atomic force microscopy (AFM)

AFM is one type of scanning probe microscopy. The working principle of the AFM is based on measuring the interaction of sample surface and a sharp tip (which originates from various forces such as, van der Waals forces, electrostatic or magnetic). AFM consists of three major components which are cantilever with a sharp tip as probe, piezo-electric scanner to move sample and/or tip and the split photodiode to measure deflection of cantilever. The deflection of cantilever is measured by means of a laser. The laser is focused on the reflective back side of the cantilever. The reflected laser beam from cantilever then is focused on the center of quadrupole photodiode. Therefore, as cantilever deflects due to interaction with the surface, laser will be deflected too and quadrupole photo detector measures this deflection. The working principle of AFM is depicted in **Figure 33**.

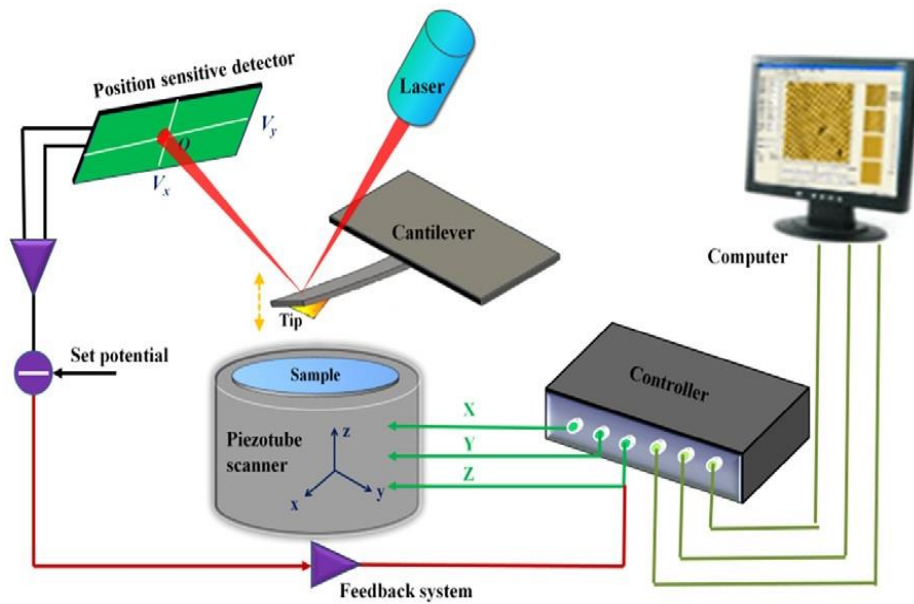


**Figure 33.** Schematic illustration of AFM working principle. Retrieved from ref [108].

The force versus distance curve between surface and tip of cantilever is presented in **Figure 34**. As can be seen, at larger distance there is very weak attraction between the tip and the surface. By approaching to the surface, this attraction increases till a specific distance (about several angstrom). By means of choosing a certain interaction regime, AFM can be operated in contact mode, noncontact mode and tapping mode. In contact mode, tip and sample surface has physical contact, hence, short range repulsive force is the tool to imaging topography of sample. This regime of operation usually enables high resolution topographic image. However, due to the nature of the force, sample may be damaged. In non-contact mode, the tip and surface are separated 1 nm to 10 nm which results in weak attractive forces between tip and sample surface. A piezoelectric is used to oscillate cantilever at its resonance frequency. Then amplitude, phase and frequency of oscillations are measured. In the tapping mode, the cantilever is oscillated at a constant amplitude in a way that the tip touches the surface gently at the bottom of oscillation. Bringing the tip intermittently in contact to the sample, the reduction in oscillation of cantilever is inevitable due to energy lost by touching the surface. Hence, amplitude of oscillation changes which is detected and



from a surface (interface) its polarization changes which can be expressed by two factors,  $\psi$  and  $\Delta$ , where  $\psi$  is the ratio of the amplitude of the p polarized component of the light to s polarized component and formulated as follows:

$$\tan(\psi) = \left| \frac{r_p}{r_s} \right| \quad \text{Equation 2}$$

Where  $r_p$  and  $r_s$  are Fresnel reflection coefficients.  $\Delta$  is the phase difference between the p and s polarized light and denoted as:

$$\Delta = \delta_p - \delta_s \quad \text{Equation 3}$$

Where  $\delta_p$  is phase change in p polarized light and  $\delta_s$  is the phase change in s polarized component upon reflection from sample surface. If the sample is made up of several different layers each with different optical properties than at each interface (between the neighboring layers) reflection and transmission will take place. Then the total amplitude of light reflected from the top layer's surface with p and s polarization will be given by total reflection coefficients  $R_p$  and  $R_s$  [these coefficients are analogues to  $r_p$  and  $r_s$  that are relevant for a single layer (interface) system]. As discussed earlier these two parameters  $R_p$  and  $R_s$  (or  $r_p$  and  $r_s$  for a single layer system) can be correlated to reflectance ratio as follows:

$$\rho = \frac{R_p}{R_s} = \tan(\psi)e^{i\Delta} \quad \text{Equation 4}$$

Reflectance ratio,  $\rho$ , is a complex function which depends on the incidence angle ( $\phi_0$ ) and the wavelength ( $\lambda$ ) of the light and complex refractive indices ( $N_j = n_j + ik_j$ , where  $j$  labels the layers. It should be noted that  $N$ , which is also named as optical constant, further depends on  $\lambda$ ) and thicknesses ( $d_j$ ) of all the layers (labeled by  $j$ ) in the sample (in addition to  $N_{\text{air}}$ ).

In spectroscopic ellipsometry,  $\psi$  and  $\Delta$  are measured as a function of wavelength ( $\lambda$ ) at fixed incidence angle ( $\phi_0$ ). Hence by fitting the experimentally measured  $\psi$  vs.  $\lambda$  and/or  $\Delta$  vs.  $\lambda$  curves to a function (based on Fresnel equations) which parametrically depends on  $d_j$  and  $N_j$ , the thickness and the refractive indices of all the layers could be determined. Of course the reliability of the results obtained strongly depends on the fit

function used. If, on the other hand, some of the parameters ( $d_j$  and/or  $N_j$ ) are already known from previous measurements (literature), the number of fit parameters can be reduced which increases the reliability of the results significantly. The quality of the fit is judged by using the mean square error (MSE) of the data produced by the fit function compared to the experimentally measured data. For the best fit MSE is expected to be minimum (as close to zero as possible).

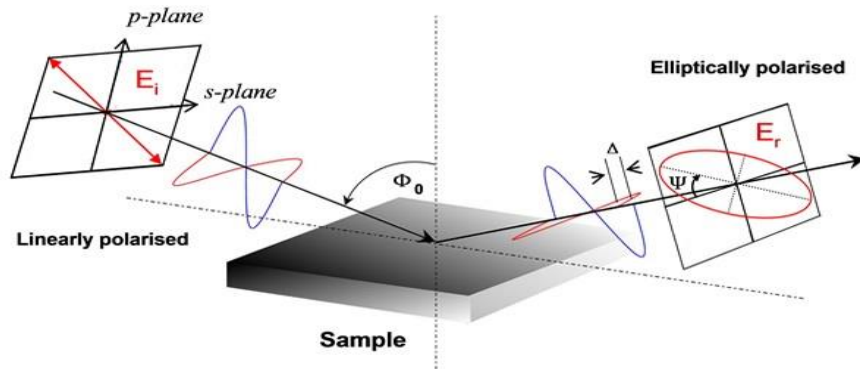


**Figure 35.** The working principle of spectroscopic ellipsometry. Retrieved from ref [109].

To construct the fit function a model is used which describes the number and nature (optical constants,  $N$ ) of the layers that make up the sample. There are different dielectric function models to obtain  $N$  as a function of wavelength. For semi-transparent and transparent films Cauchy or Sellmeier (dielectric function) models are used commonly, whereas, for absorbing or opaque films Drude-Lorentz and Lorentz (dielectric function) models can be used.

For modelling SAMs studied in here we used a three phase model in which the samples are assumed to be made up of three layers as gold/SAM/air. The layer beneath the gold film (which is epoxy resin in case of TS-Au or mica in case of FA-Au) need not be considered because the thickness of the gold film is very high (about 100-150 nm) through which light is incapable of passing through and reaching the layer beneath. For modelling dielectric properties of the gold film, however, either Drude-Lorentz model or the  $N$  values (as a function of wavelength) reported in the literature can be used both of which yield equally good fits. The dielectric properties of the SAMs, on



$$\gamma_{sv} = \gamma_{sl} + \gamma_{lv} \cos \theta_Y \quad \text{Equation 5}$$

Where  $\gamma_{sv}$  is solid-air interfacial tension,  $\gamma_{sl}$  and  $\gamma_{lv}$  are solid-liquid and liquid-air interfacial tensions respectively.  $\theta_Y$  is Young's contact angle. **Figure 37** shows these interfacial tensions and contact angle.

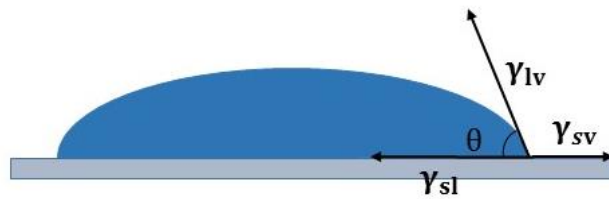


**Figure 37.** Related interfacial tension in contact angle.

The contact angle of an ideal (homogeneous and flat) surface and that of a rough one (with exactly the same chemical nature) can be correlated by Wenzel equation as follows:

$$\cos \theta_{observed} = r \cos \theta_{ideal} \quad \text{Equation 6}$$

Where  $r$  represent the surface roughness and  $\theta_{ideal}$  is the angle in ideal case which means roughness of surface is equal to 1. According to this model, for a hydrophobic surface ( $\theta > 90^\circ$ ) as roughness decreases the observed contact angle decreases whereas for a hydrophilic surface as roughness decreases contact angle increases.

In case of heterogeneous surfaces or for SAMs made up of two or more components, however, different approaches should be followed in order to interpret the observed contact angles. [110-111] One such approach is the Cassie's law that relates the contact angle of a two component film (surface),  $\theta_{obs}$ , to the contact angles of each of the components,  $\theta_1$  and  $\theta_2$ , as follows.

$$\cos \theta_{obs} = q_1 \cos \theta_1 + q_2 \cos \theta_2 \quad \text{Equation 7}$$

Where  $q_1$  and  $q_2$  ( $q_2=1-q_1$ ) are the mole fractions of components in the film which define the composition. In this approach, however, the components of the film are considered to act independently and their effect on the contact angle is assumed to change linearly with changing surface composition (ratio of the surface concentration of one of the CT isomer to the other one). Hence for a given (measured) set of  $\theta_1$ ,  $\theta_2$  and  $\theta_{obs}$ , surface composition (values of  $q_1$  and  $q_2$ ) can be determined. In this work applicability of the Cassie's law to mixed CT SAMs were investigated and will be discussed in the Results section.

### 2.1.3.1 Static contact angle

In order to determine the interaction of solid and the probe liquid on homogenous and smooth surfaces static contact angle measurements are performed. By utilizing this method, where the droplet is stationary, the hydrophobicity/ hydrophilicity of the surface can be determined. As an example, the picture of a static water droplet on a gold surface modified with 1-Octadecanethiol SAM is provided in **Figure 38** which has a contact angle of  $110.05^\circ \pm 0.02$ .

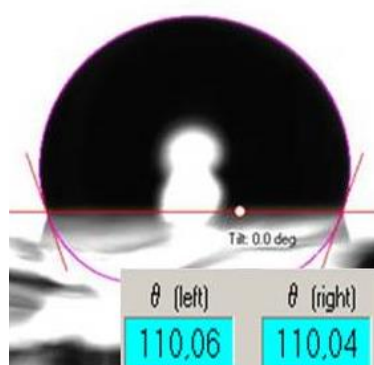


**Figure 38.** Static contact angle of 1-Octadecanethiol SAM on thermally evaporated gold on mica.

### 2.1.3.2 Dynamic contact angle

In practice there are metastable states of a liquid droplet on the surface, hence, the measured contact angle is not exactly equal to Young's contact angle. Therefore, measuring static contact angle is not adequate to characterize the surface wetting properties. One approach to investigate detailed surface wettability is measuring dynamic contact angles. In other words, the contact angles that are formed during contracting and expanding the liquid (by increasing/decreasing the volume of liquid which causes the edges of the droplet to advance or recede) is measured and interpreted. The angle reaching to the maximum value is advancing angle and the angle approaching to minimum value is the receding angle. **Figure 39** shows water droplets during advancing ( $117.96^{\circ} \pm 0.32$ ) and receding ( $103.72^{\circ} \pm 1.78$ ) contact angle measurements on 1-Octadecanethiol SAM on the same gold substrate. The difference of the receding and advancing angle is defined as hysteresis (H) and is formulated as:

$$H = \theta_A - \theta_r \quad \text{Equation 8}$$

Here,  $\theta_a$  is the advancing angle and  $\theta_r$  is the receding angle. The interpretation of surface heterogeneity and roughness can be performed based on hysteresis values.

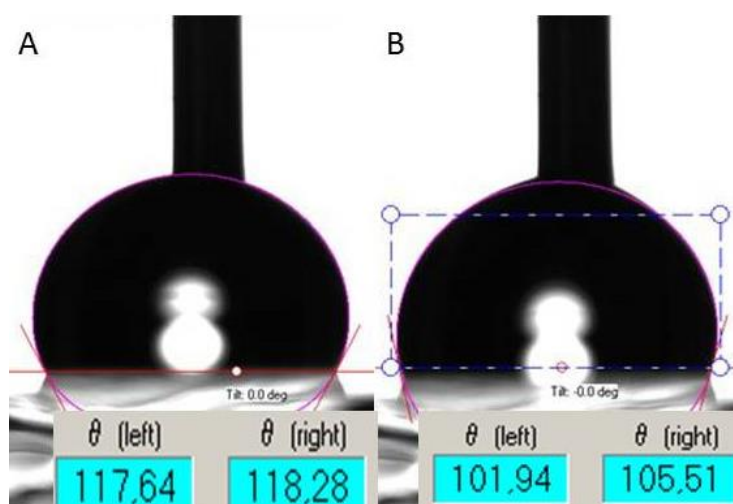


**Figure 39.** a) Advancing contact angle measurement of 1-Octadecanethiol SAM on gold. b) Receding contact angle measurement of 1-Octadecanethiol SAM on gold.

## 2.2 General experimental procedures

In this section technical details and working parameters of the instruments used in the study will be provided. In addition, details of the gold substrate and SAM preparation procedures will be explained.

### 2.2.1 Au film and self assembled monolayer preparation

**Materials.** 1-octadecanethiol (ODT, 97 %), 11-Mercapto-1-undecanol (MUD, 97%), Ethanol (99.8%) and Acetone (99.5%) were purchased from Sigma-Aldrich. The chemicals o-carboran-1-thiol (98%), m-carborane-1-thiol (96%) and m-carborane-9-thiol (97%) were purchased from Katchem Ltd (Czech Republic). All chemicals used as received without any further purification. The chemical structure of these molecules are depicted in **Figure 40**. Carboxylic acid functionalized m-carborane-9-thiol was synthesized and characterized, however, due to time limitation the film properties could not be investigated (for more details see APPENDIX section 2) . Gold pellets (99.99%) bought from Kurt J. Lesker Company and Istanbul gold refinery and were used for the gold surface preparation. The two epoxy glue used in the template stripped

procedure were Norland optical adhesive 61 (USA, purchased from Optomek Ltd Turkey distributor) and SU-8 (2000) from Microchem (USA). Ruby muscovite mica (which was used as substrate in gold surface preparation) was purchased from S&J trading Inc (USA).

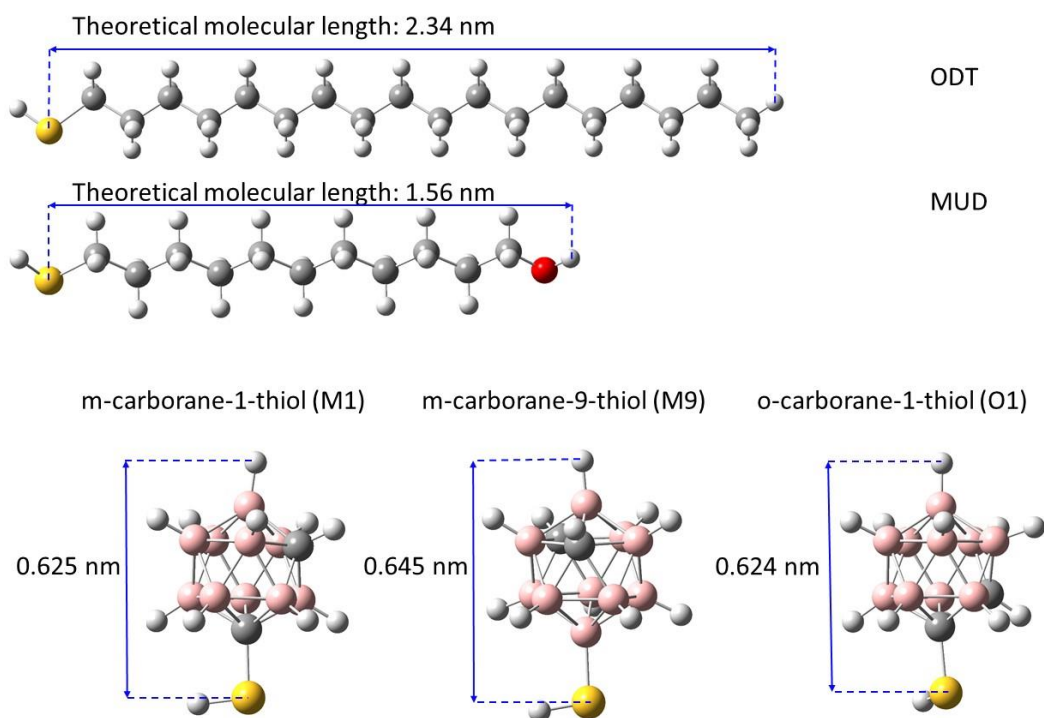


**Figure 40.** The chemical structure of molecules was used in this thesis. ODT and MUD was the reference molecules to optimization instruments and SAMs preparation. Grey: carbon, pink: boron, yellow: sulphur, white: hydrogen, red: oxygen. Theoretical lengths are calculated at AM1 level for alkanethiols and at DFT (PBE) level for carboranethiols.

Au films were prepared by thermal evaporation onto freshly cleaved mica wafers with 15x15 cm<sup>2</sup> size. Tungsten boat loaded with gold was heated resistively (1250 °C) to achieve a deposition rate of  $\approx 0.4 \text{ \AA s}^{-1}$ . The preferred thickness of the Au films was 150 nm which was monitored by a quartz crystal oscillator during deposition. Deposition was carried out in a deposition chamber at a base pressure of  $1 \times 10^{-6}$  mbar (pumped by an oil-free pump) at room temperature. Freshly prepared gold films were



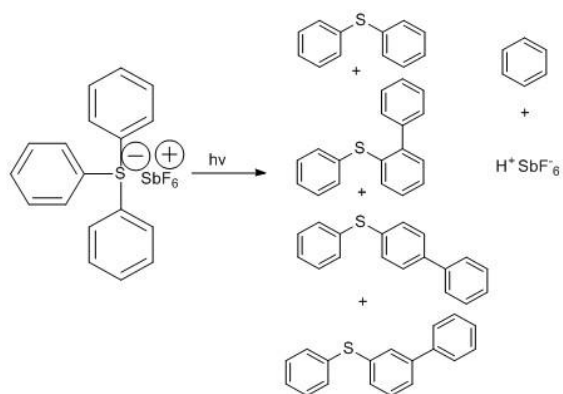


**Figure 41.** Activation of triaryl sulfonium hexafluoroantimonate catalyzer.

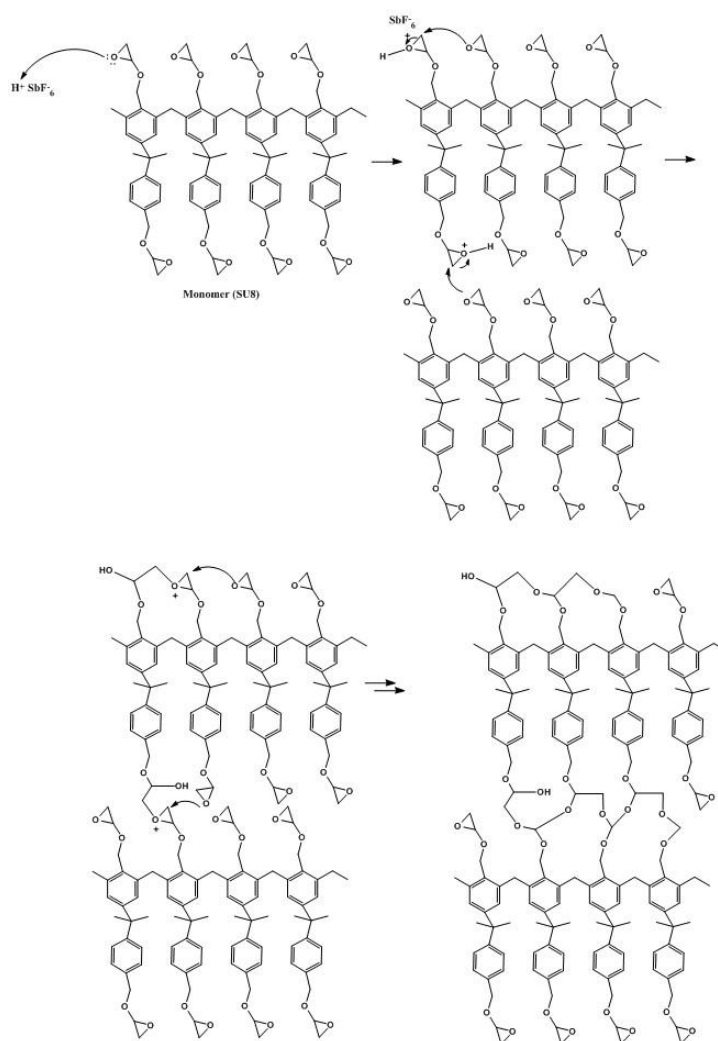


**Figure 42.** Polymerization of SU 8 after activating catalyst. Intra as well as inter molecular polymerization takes place via in cross linking.



as described in the previous section. Then about 2 mg of SU-8 epoxy resin dripped on gold slide and glass pieces was put on it and gently pressed. After the sandwich preparation, it was illuminated to 365 nm monochromatic light from glass side for 1 hour. The mica could easily be cleaved by tweezers and flat gold films could be obtained successfully. However after 1 day in ethanol, the prepared gold surfaces were observed to deteriorate as depicted in **Figure 44 A**. The reason of this deterioration was thought to be low degree of polymerization. Hence to perform hard baking and increase degree of polymerization after the illumination to the light the sandwiches were baked for 24 hours **Figure 44 B**. However, the deterioration problem was still present even after this procedure.

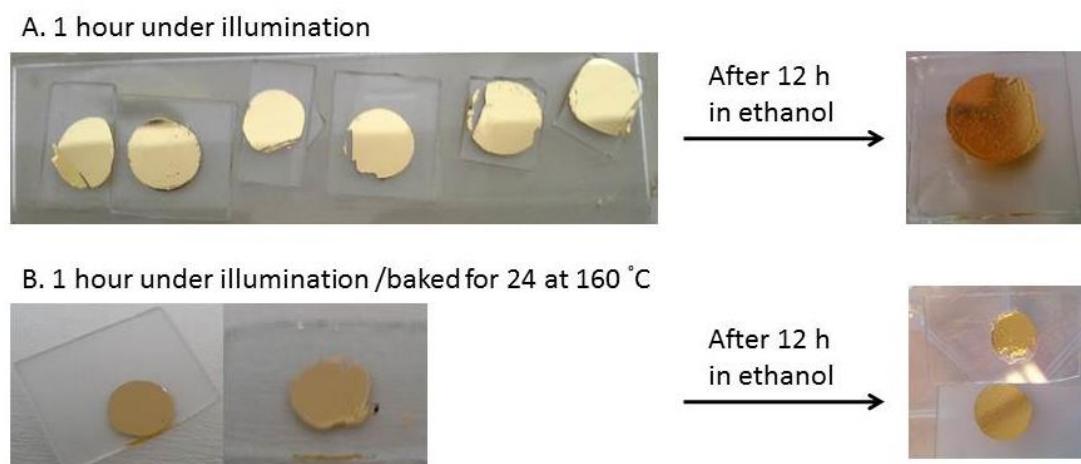


**Figure 44.** UV-Visible assisted crosslinking. A) 1 hour light illuminated then kept in ethanol for 12 hours. B) 1 hour light illuminated and hard baked for 24 hours then kept in ethanol.

Different procedures were used to solve the deterioration problem. For example, soft baking (4mg the glue spin coated on glass at rate of 5000 rpm for 30 s then 5 min heated at 65 °C and 15 min 95 °C) was performed before illumination of the light. However, in this case gold films did not attach to glass surface. In the final procedure the resin (sandwiches) were illuminated to 365 nm light for 24 hours which yielded the best template stripped (TS) gold films. Increasing illumination time hardens epoxy resin and flat gold surface could be stripped successfully with a yield of 85% (11 gold

stripped from 13 sandwiches prepared). A successfully stripped gold is shown in **Figure 45**.



**Figure 45.** Successfully stripped gold by UV-Visible assisted cross linking.

### 2.2.3 Contact angles

Static contact angles of water were measured at room temperature on an Attension Theta Lite optical tensiometer. An approximately 2  $\mu\text{l}$  drop of water was formed at the end of a needle attached to a 50  $\mu\text{l}$  syringe. The needle was lowered until the drop touched the surface and then raised, detaching the drop. Dynamic contact angle measurements were performed using a dynamic sessile drop method, where a sample is placed near the tip of the needle. A drop of deionized water (2  $\mu\text{l}$ ) is deposited on the surface of the sample, and the needle is carefully positioned in the center of the drop without changing its shape. The advancing contact angles were determined by increasing the volume of drop on surface to a size of 4  $\mu\text{l}$ . The receding contact angle was measured at the same speed of volume reduction to a size of 2  $\mu\text{l}$ . All these measurements were collected on an automated system with photographs. The photographs were collected at 20 frames/second for three seconds. The drop images were processed with an image analysis software, which calculated both left and right contact angles from the shape of the drop with an accuracy of  $\pm 0.1^\circ$ . For each SAM composition studied, three parallel samples were prepared and on each sample measurements were made on two different positions on the surface. Hence each data point reported in the contact angle plots that will be discussed in the Results section corresponds to average of 6 measurements.

#### **2.2.4 Spectroscopic ellipsometry**

Ellipsometric measurements were performed on a PhE-102 Variable Angle Spectroscopic Ellipsometer (VASE) equipped with a 75W Xe lamp from 250 nm to 1100nm at an incident angle of 65°. Measurements were taken with a spot size of 1.5 mm. Samples were rinsed with ethanol and blown dry in a stream of nitrogen prior to characterization. Each bare gold sample was individually measured and then immersed directly in the appropriate thiol solution for SAM preparation. These measurements took a total time of less than 15 min. After removal from the thiol solution, with appropriate cleaning, the samples were again measured. The film thickness calculations were based on a three-phase ambient-film-gold model in which the film was assumed to be isotropic and assigned a scalar refractive index value of  $1.57 + 0i$  which was determined by Abbe Refractometer measurements. For each SAM composition studied, three parallel samples were prepared and on each sample measurements were made on two different positions on the surface. Hence, each data point reported in the ellipsometric thickness plots that will be discussed in the results and discussion chapter corresponds to average of 6 measurements.

#### **2.2.5 Atomic force microscopy**

The system used for AFM measurements was a commercially available Ambient AFM/MFM (Nanomagnetics instruments, Ankara). The measurements were performed in air at room temperature by use of a Silicon cantilever (rectangular with 225  $\mu\text{m}$  long) with a force constant of 48 N/m. All images (1.25x1.25  $\mu\text{m}^2$ ) were collected in constant amplitude in tapping mode of Ambient AFM. The images were taken at scan rate of 0.5  $\mu\text{m}/\text{s}$  and WSXM software was used to plane fit the images. Also, to compare the measurements a few samples were analyzed with Veeco MultiMode V AFM.

Quantitative analysis of AFM images was performed by the free software Gwyddion. This program is a modular software for SPM imaging and analysis. Vincent algorithm for watershed was utilized to find grains/domains on the surface. The grains are

marked by virtual water droplet that fills the low potential (height) part of the image. There are six parameters for processing SPM images as follow.

1. Gaussian smoothing:

A mask is produced by the algorithm to smoothen the image by using Gaussian Dispersion.

2. Add gradient:

Relative weight of the mask is added to the image according to local slope. As local slope increases larger value of gradient is needed to mark the grain boundaries.

3. Add curvature:

The concaveness of grains detected by the algorithm is adjusted by this parameter. Large value of local concaveness indicates grain boundaries.

4. Barrier level:

This parameter determines threshold value to mark boundaries. The absolute minimum of the image gets 0% and absolute maximum of the image is assigned 100 % value. The boundaries could be marked by adjusting this value, by increasing this value concaves start to be filled by the mask.

5. Prefill level:

Prefills the valleys to eliminate details at deep valleys. Since valleys are filled before mask is applied, increasing this parameter effect the mask at the bottom of valleys. It is suggested to maintain this parameter close to 0% to have precise analysis.

6. Prefill from minima:

Prefills the local minima to eliminate details at local valleys. This parameter effects the valleys by considering the local minima whereas absolute minima is taken into account at prefill level (parameter 5).

To demonstrate AFM image analysis, processed images and processing parameters for bare gold on mica are shown in **Figure 46**. The abovementioned six factors were adjusted in a way that boundaries are marked with the mask clearly. The blue regions shows gold domains and the yellow-orange sites shows the boundaries of these domains. Total projected length of the boundaries (yellow sites) was calculated by software and reported as domains boundaries length. In addition, black regions can be

seen in image which shows pits on gold surface. The projected area of the pits and domain boundaries will be reported as defects. The area of these defects are relative to the scan area, hence, the reported defect area are percentage to scan area. Remaining AFM image of SAMs were analyzed by using the same program and by adjusting the parameters (For more processed image of SAMs see APPENDIX section 3).

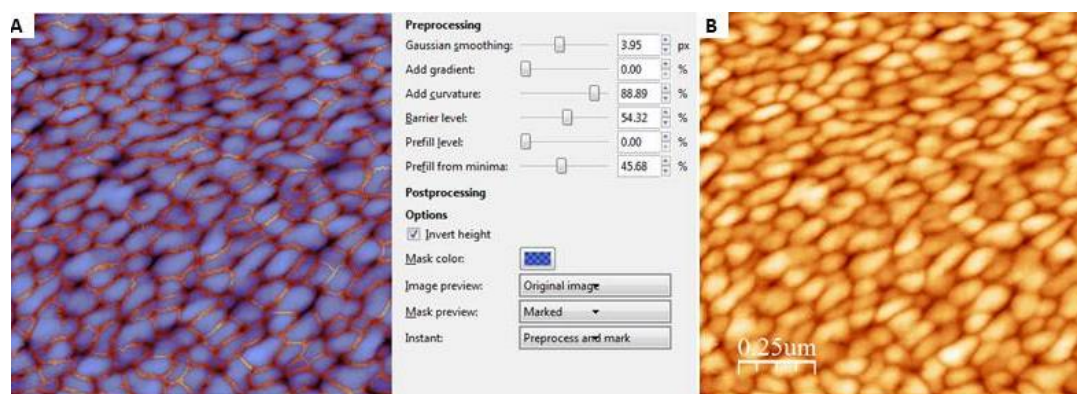


**Figure 46.** AFM image processing: A) A processed image and the program window that shows the used parameters. B) Raw height image of the sample.









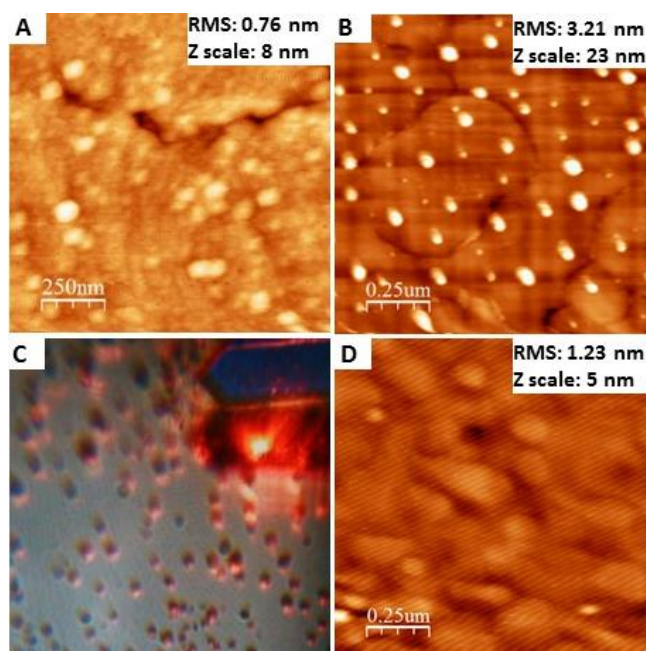


**Figure 49.** Treatments to eliminate contamination. A) piranha treated Au surface. B) ozone treated Au surface. C) microscopic contamination on gold which was flamed for 5 min. D) AFM image of contaminated gold surface after 5 min.

To find the source of contamination scanning electron microscopy (SEM) analysis were performed on 5 min flame annealed samples the results of which are depicted in **Figure 50**. SEM results suggest that mica substrate surface pops and orifices form in/on the gold surface (**Figure 50C**). In order to determine the chemical nature of these features energy dispersive X-ray analysis (EDX) was performed on two different parts of the gold film. EDX analysis indicates the chemical composition of the surface as muscovite mica ( $(\text{KF})_2(\text{Al}_2\text{O}_3)_3(\text{SiO}_2)_6(\text{H}_2\text{O})$ ) and gold (the peak of carbon at 0.22 keV) with no indication of organic contaminations. The reason of the formation of the orifices is thought to be due water molecules trapped between the layers of mica which diffuse to the surface upon annealing. In fact, many groups suggested to heat mica substrate to remove any hydroxyl and water adsorbents before evaporating the gold film. [74–76] However, since the evaporator we used did not have heating capability we were not able to anneal the mica substrates in vacuum. Instead we tried annealing







thickness of the formed SAMs is less than the theoretical molecular length of the molecules. This discrepancy, between molecular length and SAM thickness is due to tilt angle of the SAM surfactants (the tilt angle is almost  $30^\circ$  for both molecules). The structure of SAMs as well as the relation between molecular length and SAMs thicknesses are depicted in **Figure 52**.

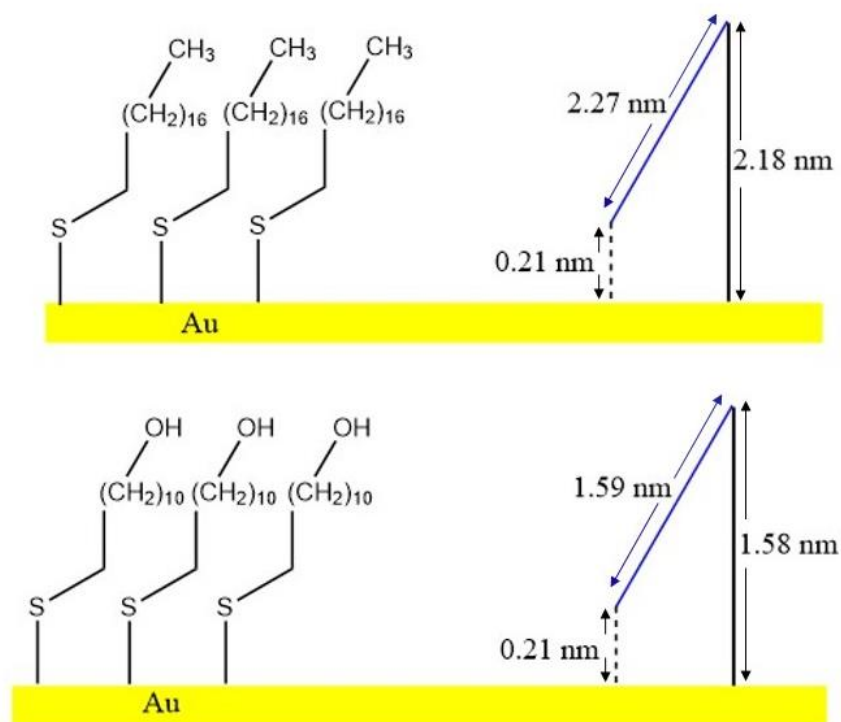


**Figure 52.** Schematic presentation of reference SAMs on surface. A) ODT SAM. B) MUD SAM. The molecular length and SAMs thicknesses are related to each other and can be calculated by considering the tilt angle of the molecules. The blue line indicate theoretical length of molecules from center of top hydrogen to center of sulfur. Dash line shows sulfur-gold bond length. Black lines show the theoretical thickness of SAMs.

SAMs of ODT and MUD were prepared from ethanolic solutions of corresponding molecules. 1mM solutions were prepared for each species and gold substrates were submerged for 24 hours in the corresponding solutions. These SAMs were characterized by means of contact angle, ellipsometry and AFM measurements.

**Figure 53** shows water CAs and ellipsometric thickness of ODT SAMs on (30

seconds) FA-Au and TS-Au (The CA of ODT on TS-Au and FA-Au surfaces are referred to as TS-ODT and FA-ODT respectively). CAs are also tabulated in **Table 4** to facilitate comparison of the results. CAs of full monolayer of ODT agree with literature values which varies in the range of 110-113°. [87,88] Due to nonpolar CH<sub>3</sub> termination, ODT SAMs form a hydrophobic surface. In other words, polar water molecules do not wet the nonpolar methylene surface. Due to this dissimilarity, water droplet reduces its interaction with the surface by increasing the CA. For alkanethiols CA is reported to increase as the chain length of the molecules forming the SAM increases. The reason of increasing in CA is the formation of a well-defined crystalline structure due to significant van der Waals interaction of backbone of the molecules. The CAs and ellipsometric thickness (about 2.5 nm) of ODT on both surfaces are close to literature values (2.21 nm). [91,92] The slightly higher value of the SAM thickness might be due to physisorption of molecules or accuracy limitation of our ellipsometer (the accuracy is  $\pm 0.3$  nm). On the other hand, OH terminated MUD SAMs are polar, hence substrates decorated with MUD SAM would have hydrophilic characteristics. **Figure 53** shows water CAs and ellipsometric thickness of MUD SAMs on FA-Au and TS-Au (The CAs of MUD on TS-Au and FA-Au surfaces are referred to as TS-MUD and FA-MUD respectively). The thickness of the MUD SAMs are almost equal on both substrates (1.6 nm) however the CAs value on TS-Au surface could not be measured since water disperses completely on the surface. [85,91,92] This can be due to more well-ordered SAM formation of MUD on template stripped surface relative to the FA-Au. Representative AFM images of alkanethiol SAMs on both substrates are shown in **Figure 54**. The domain boundaries of alkanethiols can clearly be seen on TS-Au substrates (**Figure 54 A** and **C**). The boundaries form due to merging of SAM domains with different orientation or domain boundaries of the substrate. The results of quantitative analysis of ODT and MUD SAMs are summarized in **Table 5** (The defect size and grain boundary length determined by software, for more details see 2.2.5).

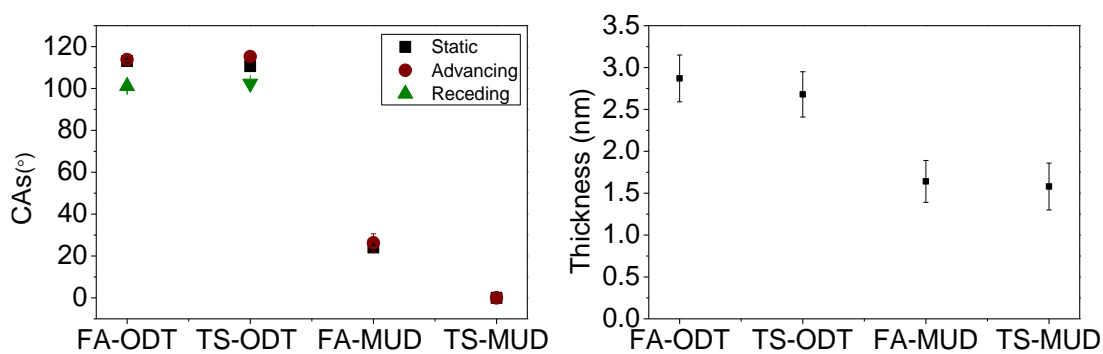


**Figure 53.** Contact angle and ellipsometric thickness of ODT and MUD on TS-Au and FA-Au.

**Table 4.** Contact angle results of reference SAMs.

	<i>Static</i>	<i>Advancing</i>	<i>Receding</i>	<i>Hysteresis</i>
<b><i>TS-ODT</i></b>	110.7±0.7	115±0.6	102.4±1.2	12.6
<b><i>FA-ODT</i></b>	113.1±0.8	113.8±2.1	101.1±1.8	12
<b><i>TS-MUD</i></b>	0	0	0	0
<b><i>FA-MUD</i></b>	24.1±1	26.3±4.3	-	-

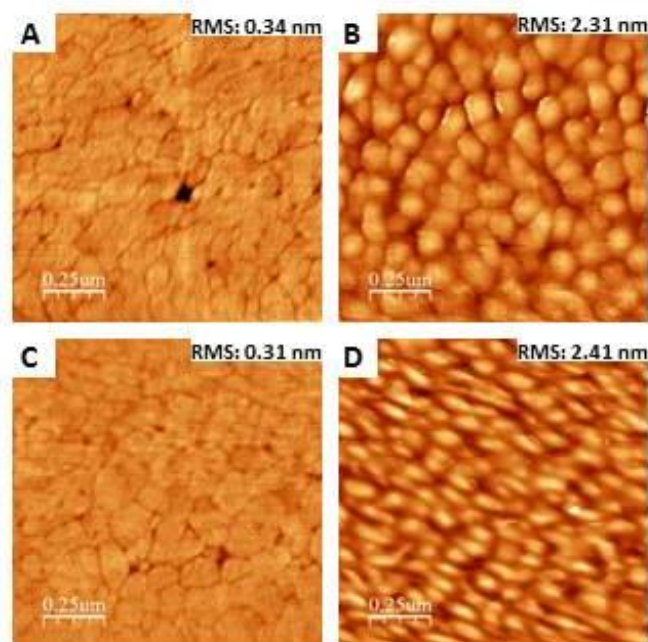


**Figure 54.** AFM images of alkanethiol SAMs on template stripped and flame annealed (30 s) gold. A) ODT on template stripped gold. B) ODT on flame annealed gold. C) MUD on template stripped gold. D) MUD on flame annealed gold.

**Table 5.** Results of quantitative analysis of AFM for ODT and MUD growth ODT.

	<i>Average roughness (nm)</i> <i>1.25x1.25 <math>\mu\text{m}^2</math>/2.5x2.5 <math>\mu\text{m}^2</math></i>	<i>Average Boundary length</i> <i>1.25x1.25 <math>\mu\text{m}^2</math>/2.5x2.5 <math>\mu\text{m}^2</math></i>	<i>Average defect coverage</i> <i>1.25x1.25 <math>\mu\text{m}^2</math>/2.5x2.5 <math>\mu\text{m}^2</math></i>
<b>ODT</b>	0.32±0.03/0.28±0.03	29.0±2.04/105±13	9.09±0.20/9.12±1.22
<b>MUD</b>	0.29±0.03/0.29±0.05	45.1±6.88/107±28	8.45±0.48/9.81±1.02

To facilitate optimization study, time dependent film formation of ODT on TS-Au was investigated. The aim was to observe striped phase formation by AFM. Hence, films were grown by keeping the gold substrates in dilute ODT solutions (about 50  $\mu\text{M}$ ) for 3 s and 10 s. Although striped phases were not observed, the resulting films had significantly different morphological properties as will be discussed below. The contact angle and ellipsometric thickness of films are shown in **Figure 55** and tabulated in **Table 6**. The static CAs are lower than well ordered (full coverage) ODT SAMs by 20°. The reduction in CA is more pronounced for receding CAs. Moreover, high hysteresis (about 30°) of CAs with respect to full coverage ODT SAMs (12°) shows that the films are not formed densely. Besides these, quite high standard deviation for SAMs grown with 3s immersion in ellipsometric thickness is another indication of the disorder/inhomogeneity of the film. Representative AFM images and corresponding quantitative analysis of samples are depicted in **Figure 56** and **Table 7**, respectively. The analysis of images show that 3 s immersed films contain average defect area of 5.95% whereas 10 s immersed samples have defect area of 1.95%.

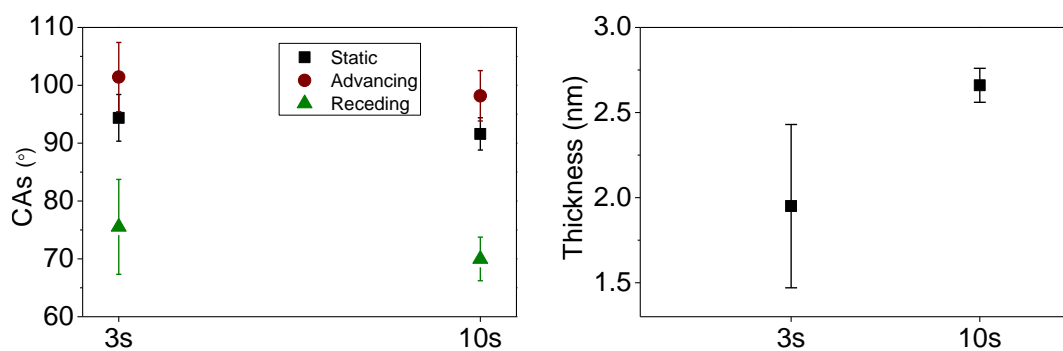


**Figure 55.** Contact angle and ellipsometric thickness of ODT growth from solution for 3 s and 10 s.

**Table 6.** Contact angle results of 3 s and 10 s growth ODT film.

	Static	Advancing	Receding	Hysteresis
<b>3s</b>	94.37±4.03	101.4±5.97	75.5±8.2	25.9
<b>10s</b>	91.6±2.78	98.2±4.35	70±3.77	21.6

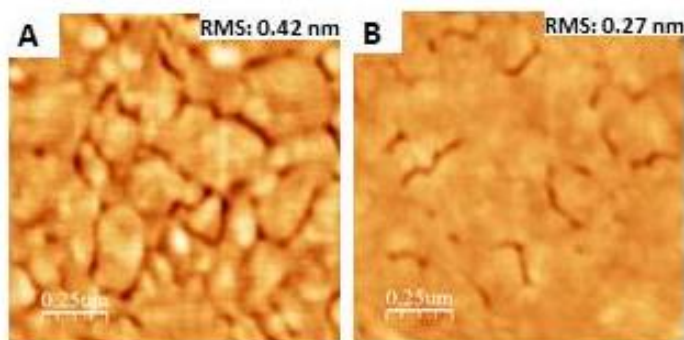


**Figure 56.** AFM image of ODT growth for A) 3 s and B) 10 s.

**Table 7.** Results of quantitative analysis of AFM for 3 s and 10 s growth ODT film.

	<i>Average roughness (nm)</i>	<i>Average domain boundary length (μm)</i>	<i>Average defect coverage (%)</i>
<b>3s</b>	0.43±0.02	14.7±2.25	5.95±0.95
<b>10</b>	0.28±0.01	6.1±1.8	1.93±0.66

### 3.3 Carboranethiol SAMs

Pseudo-crystalline SAMs of organic alkanethiols provide suitable interfaces for variety of applications such as nanotechnology and semiconductors. Functionalization of molecules utilized as component of SAMs enables surface properties to be tuned for desired applications. In this context, cage molecules draw interest due to their rigid structure and tunable chemical or structural properties. Thiol derivatives of dicarba-closo-dodecaboranes (HS)-C<sub>2</sub>B<sub>10</sub>H<sub>11</sub> with icosahedral molecular structures is one of the promising candidates for 3D-SAMs. The SAMs of carboranethiols (CTs) possess various advantages relative to organic counterparts, such as high stability towards chemical and thermal degradation as well as well-ordered monolayer formation that has fewer defects. The last advantage can be attributed to robust chemical structure and anchoring molecules almost perpendicular to surface whereas organic SAMs folded and have tilt angle. Organic SAMs form collapsed sites due to folding of the chain which results in defect formation in the film. However, such defect does not appear in CT SAMs owing to rigidity of carborane's backbone. Besides this, etch pits formed in organic SAMs were not observed in CT SAMs.

Advanced synthetic approaches in preparation of these compounds offer substitution on both boron and carbon. Altering positions of carbon atoms in the cage changes the dipole moment strength and direction while maintaining an identical assembly and molecular geometry. Therefore, each isomeric carboranethiol has specific dipole moments strength and orientation. The difference in dipole moments of isomers enables to tune surface properties such as work function and wettability.

In this work, SAMs of three positional isomers of carboranethiols on Au(111) was characterized. These isomers are 1-mercapto-1,7- dicarba-closo-dodecaborane (M1), 9-mercapto-1,7-dicarba-closo-dodecaborane (M9) and 1-mercapto-1,2- dicarba-closo-dodecaborane (O1). Moreover, co-deposited (mixed) SAMs of these isomers was studied by systematically changing concentration ratio of isomers in the growth solution. Since the direction and magnitude of dipole moments of carboranes are distinct, co-deposited SAMs are expected to have different properties relative to their

pure SAMs. It is worth to emphasize that O1 has almost opposite dipole moment to M9, hence we hypothesize that co-deposited SAMs of O1 and M9 could have dipole-dipole interaction. To have qualitative idea about effect of dipole-dipole interaction as well as surface wettability, static and dynamic CA measurements were performed. The thickness of SAMs was measured by means of ellipsometry. The morphology of these SAMs was investigated via AFM. Static CAs of were used to determine the surface composition of the mixed SAMs. AFM topographic (height) images were used to determine defect coverage and domain boundary lengths.

### 3.3.1 Pure carboranethiol SAMs

Contact angle and ellipsometric thickness values of pure CT-SAMs on TS-Au surface are shown in **Figure 57** and **Table 8**. Static CAs of pure M1 and M9 SAMs on TS-Au surface are consistent with the CAs reported in the literature. Although static CAs are consistent with literature values, dynamic CAs of pure M1 and M9 SAMs are quite different then what is reported by Weiss group. [105,106] To explain this difference, it is worth to review Weiss group's works in two papers they published in 2009 and 2014. [105,106] In the paper published in 2009 the dynamic CAs of M1 and M9 were reported while in the latter paper static CAs were investigated. These results are summarized in **Table 9**. As can be seen from the table, there is contradiction between dynamic and static angles reported, since static CAs should lie between advancing and receding CAs. Since our static CAs agree with those of Weiss group, and they lie between the dynamic angles measured in this study it can be safely concluded that our results are more reliable then the literature reports. The lowest CAs belongs to O1 SAM which was not studied before in the literature. CAs of O1 and M9 have significant difference (about 4°) with respect to each other in spite of the similar magnitudes of their dipole moments.

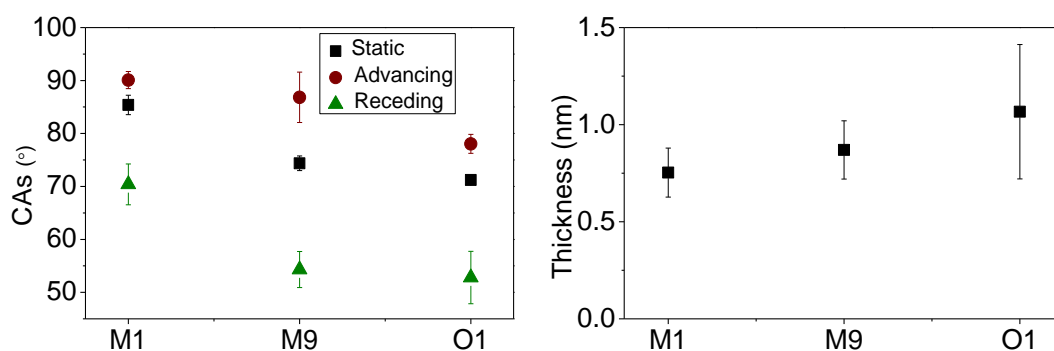


**Figure 57.** Contact angles and ellipsometric thickness for pure carboranethiols. Solid symbols refer to FA gold and the open symbols refer to TS gold surfaces.

**Table 8.** Contact angles of pure carboranethiol SAMs.

	<i>Static</i>	<i>Advancing</i>	<i>Receding</i>	<i>Hysteresis</i>
<i>M1</i>	85.4±1.8	90.1±1.6	70.4±3.9	19.7
<i>M9</i>	74.4±1.4	86.8±4.7	54.3±3.4	32.5
<i>O1</i>	71.2±0.7	78.0±1.8	52.8±4.9	25.2

**Table 9.** Contact angles of M1 and M9 in literature.

	<i>M1</i>	<i>M9</i>
<i>Advancing</i>	82±2	72±4
<i>Static</i>	85.8 ± 1.1	77.7 ± 0.8
<i>Receding</i>	71±1	52±1

Topography and morphological properties of SAMs were investigated by AFM. Topography and phase images of pure CT films on TS-Au surfaces in two different scales are shown in **Figure 58** and their properties are summarized in **Table 10**. Roughness of pure CT SAMs on TS-Au vary between 0.42 to 0.63 nm which is significantly higher than bare TS-Au (0.12 nm). The domain boundaries and pits clearly are visible in topographic images. Formation of these pits on TS-Au might be due to imperfect deposition of gold on mica substrate during thermal evaporation. The boundaries form due to merging of domains with different orientation, domain boundaries of substrates and step edges of substrate. The latter two reasons seem to be

more reasonable since CT SAMs are almost perpendicular to the surface and forms ordered structure without defects. The values of defect coverage and boundary length are close to each other which implies identical nature of different SAMs. It is worth to note that for  $2.5 \times 2.5 \mu\text{m}^2$  scans, the standard deviations are quite large in case of M9 and O1 due to higher noise level of the AFM images.

**Table 10.** Results of the AFM image analysis for pure M1, M9 and O1 films.

	$2.5 \times 2.5 \mu\text{m}^2$		$1.25 \times 1.25 \mu\text{m}^2$	
	<i>Boundaries length</i>	<i>Percent coverage of pits</i>	<i>Boundaries length</i>	<i>Percent coverage of pits</i>
<b>M9</b>	62.9±21.2*	5.40±1.57	15.6±1.97	5.54±0.81
<b>M1</b>	48.4±4.27	4.53±0.10	14.35±4.57	4.49±0.67
<b>O1</b>	77.7±23.1*	6.87±0.245	15.4±2.05	5.13±1.54

\* High standard deviation is due to noise level and/or artifact of the images.

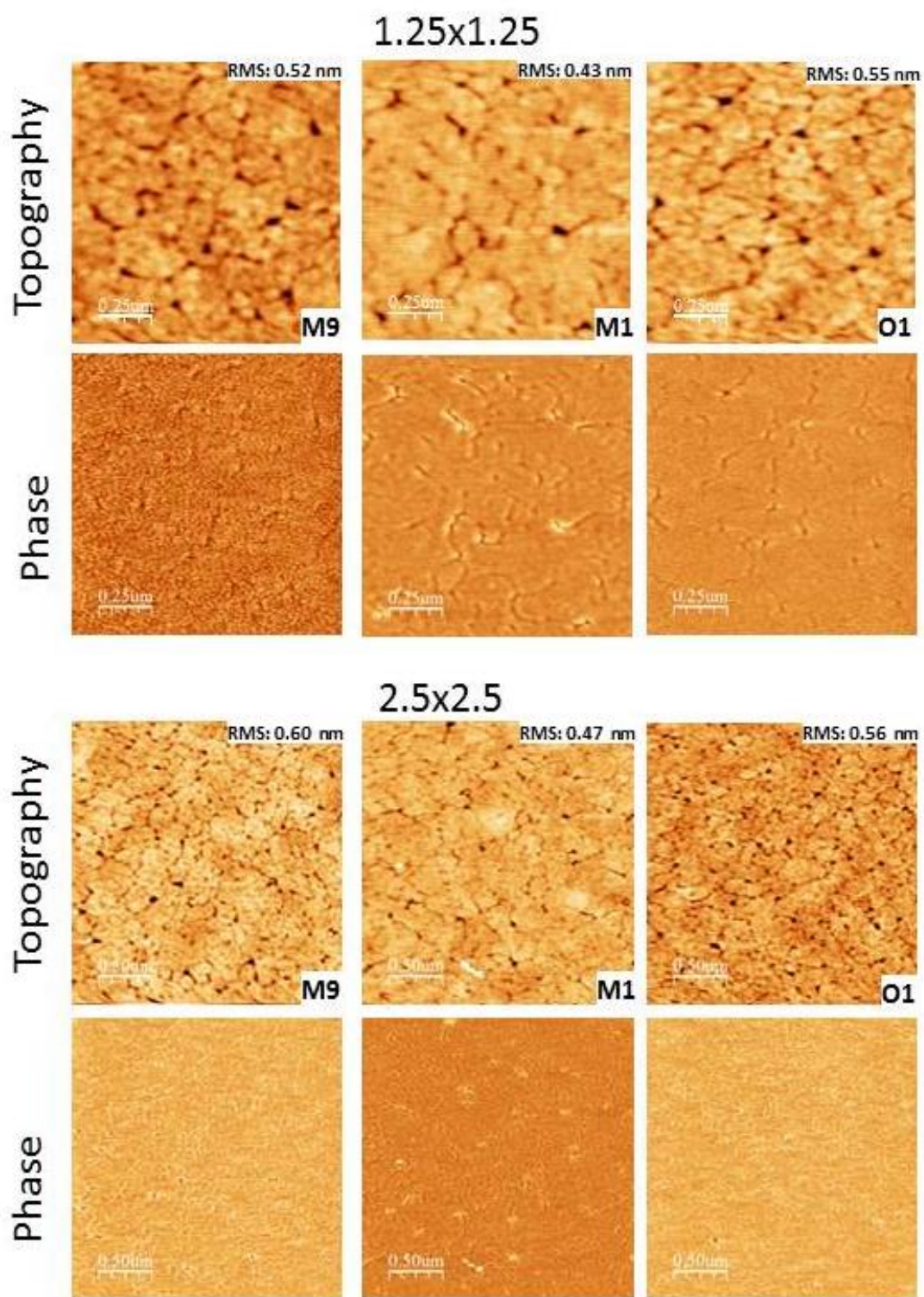


**Figure 58.** AFM images of pure M9, M1 and O1 SAMs on template stripped gold surface. Upper rows correspond to  $1.25 \times 1.25 \mu\text{m}^2$  and bottom rows  $2.5 \times 2.5 \mu\text{m}^2$ .

### 3.3.2 Mixed carboranethiol SAMs

In this part of the study mixed SAMs of CTs will be discussed. Co-deposited SAMs have different properties relative to their pure SAMs due to distinct magnitude and direction of dipole moments of the component molecules. The thickness of all SAMs were almost equal (0.8-1 nm) regardless of the surface composition. However, CAs of mixed SAMs were different with respect to pure SAMs.

#### 3.3.2.1 M1:M9 mixed SAMs

CAs and ellipsometric thickness of mixed M1:M9 films on TS-Au surfaces are exhibited in **Figure 59**. In order to facilitate a comparison with higher precision, CAs are summarized in **Table 11**. The CAs of mixed M1:M9 are close to those of pure M1 SAMs for all mixtures, however, a gradual reduction is observed with increasing M9 ratio in the growth solution. The results turned out to be the same for both dynamic and static CAs. The hysteresis values are almost similar for all ratios of M1:M9 in growth solution. In order to investigate the correlation between the M1:M9 ratio in the growth solution and on the surface (film) we utilized Cassie's law with the assumptions detailed in section 2.1.3 and calculated the theoretical CAs of mixed M1:M9 SAMs as a function of surface composition ( $q_{M1,sur}$  which is equal to  $1-q_{M2,sur}$ ) by using the CAs of pure M1 and M9 SAMs in equation 7. The resulting theoretical contact angle values are reported in **Figure 60 A**. Then by comparing this theoretical values with the experimentally observed CAs (that is by solving equation 7 for  $q_{M1,sur}$  by using the experimentally measured CAs), the surface fraction of M1 and M9 can be determined for each growth solution ratio (mole fraction of M1 in the growth solution,  $q_{M1,sol}$ ). This analysis can be applied to both static and dynamic CAs and the results are shown in **Figure 60 B** as a function of  $q_{M1,sol}$ . In addition, if the surface fractions are assumed to be equal to the solution fractions then the theoretical CAs given in **Figure 60 A** can be directly compared with the experimental CAs given in **Figure 59**. Such a comparison enables one to judge whether the surface fractions follow the solution fractions (one-to-one) which is a measure of the preferential

binding of one of the components over the other one on the surface. To enable this comparison we plotted theoretical CAs (given in **Figure 60 A**) also in **Figure 59** with lines (by assuming surface fraction being equal to solution fraction). It can be seen in **Figure 60 B** that for 3:1 and 1:1 M1:M9 solution ratio ( $q_{M1,sol}=0.75$  and  $0.5$ ), the advancing CAs yield  $q_{M1,sur}$  values larger than 1 which is of course not meaningful. This is most probably due to high standard deviation of the advancing CAs and the small difference between the advancing CAs of pure M1 and M9 films. However, the surface composition results based on static or receding CAs are more reasonable and indicate that for almost all the solution ratios, the surface fraction of M1 is higher than its solution fraction. When the static angle results are considered it can be seen that surface ratio of M1 is 49 % ( $q_{M1,sur}=0.49$ ) even at 1:3 ratio of M1:M9 in growth solution. Hence, it can be concluded that M1 has higher tendency to form film due to head to tail dipole-dipole interactions. This outcome is in agreement with the results of Weiss group who concluded that surface coverage of M1 is 56% in case of 1:3 ratio of M1:M9 in growth solution by utilizing grazing incidence FTIR. **Figure 61** presents topography and phase images of mixed M1:M9 SAMs on TS-Au surfaces. Of course we should here stress that the above given CA analysis assumes the components of the mixed SAM to effect the CA independently and linearly (with coverage) which need not be the case (see the discussion in section 2.1.3). The morphology and roughness of the films are almost identical regardless of the mixing ratio. All of the films possess a homogenous structure and no domain separation was observed in the phase image. This observation is also consistent with STM results of Weiss group which show strong structural similarities of M1 and M9 and indistinguishable nature of M1 and M9 in mixed SAMs. Quantitative analysis results of AFM images are summarized in **Table 12**. The analysis of  $1.25 \times 1.25$  as well as  $2.5 \times 2.5 \mu\text{m}^2$  images show that boundary length increase with decreasing M1 ratio in the growth solution whereas roughness remains almost constant for both scales. On the other hand, no clear trend was observed for defect (pit and domain boundaries) coverage which does not exceed 7%.

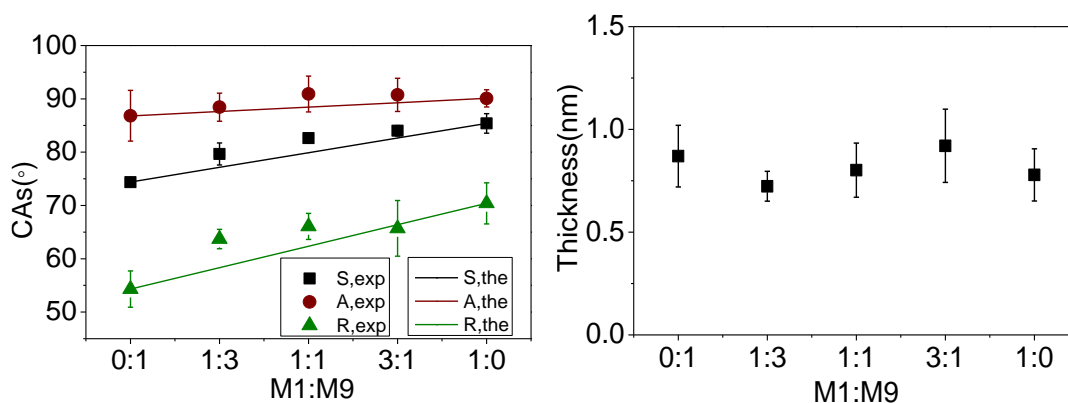


**Figure 59.** Contact angles and ellipsometric thicknesses of M1:M9 mixed SAMs. Lines in the CAs plot indicate theoretical CAs plotted by assuming surface fraction being equal to solution fraction. S: static, A: advancing and R: receding contact angles.

**Table 11.** Contact angles of M1:M9 mixed SAMs.

<i>M1:M9</i>	<i>Static</i>	<i>Advancing</i>	<i>Receding</i>	<i>Hysteresis</i>
<i>0:1</i>	74.4±0.3	86.8±4.7	54.3±3.4	32.5
<i>1:3</i>	79.7±2.1	88.4±2.6	63.7±1.8	24.7
<i>1:1</i>	82.6±0.9	90.9±3.4	66.1±2.4	24.8
<i>3:1</i>	84.0±1.0	90.7±3.1	65.7±5.2	25.0
<i>1:0</i>	85.4±1.8	90.1±1.6	70.4±3.9	19.7

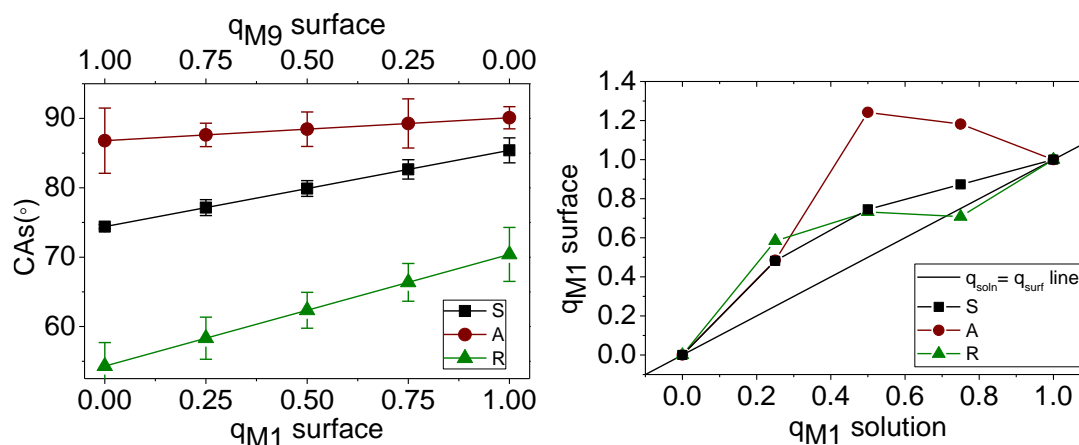


**Figure 60.** A) Theoretical contact angles as a function of surface composition for mixed M1:M9 SAMs. B) Surface composition of mixed M1:M9 SAMs calculated from the observed contact angles, plotted as a function of growth solution composition. S: static, A: advancing and R: receding contact angles.

**Table 12.** Results of the AFM image and contact angle analysis of M1:M9 SAMs.

	<i>Results of the AFM image analysis</i>		
<i>M1:M9</i>	<i>Average roughness (nm)</i> <i>1.25x1.25 /2.5x2.5 μm<sup>2</sup></i>	<i>Average domain boundary length (μm)</i> <i>1.25x1.25 /2.5x2.5 μm<sup>2</sup></i>	<i>Average defect coverage (%)</i> <i>1.25x1.25 /2.5x2.5 μm<sup>2</sup></i>
<i>1:0</i>	0.53±0.14//0.54±0.10	14.3± 4.5/48.4±4.27	4.49±0.67/4.53±0.10
<i>3:1</i>	0.40±0.08/0.42±0.05	10.9±1.8/63.1±9.53*	4.50±0.57/7.62±0.60
<i>1:1</i>	0.40±0.08/0.44±0.01	18.1±3.8/71.0±18.4*	6.94±0.07/6.96±0.54
<i>1:3</i>	0.38±0.09/0.43±0.09	18.6±1.65/75.7± 0.91	6.28±0.68/7.62±0.60
<i>0:1</i>	0.42±0.14/0.54±0.19	15.6±2.0/48.4±4.27	5.54±0.81/4.53±0.10

\* High standard deviation is due to noise level and/or artifact of the images.

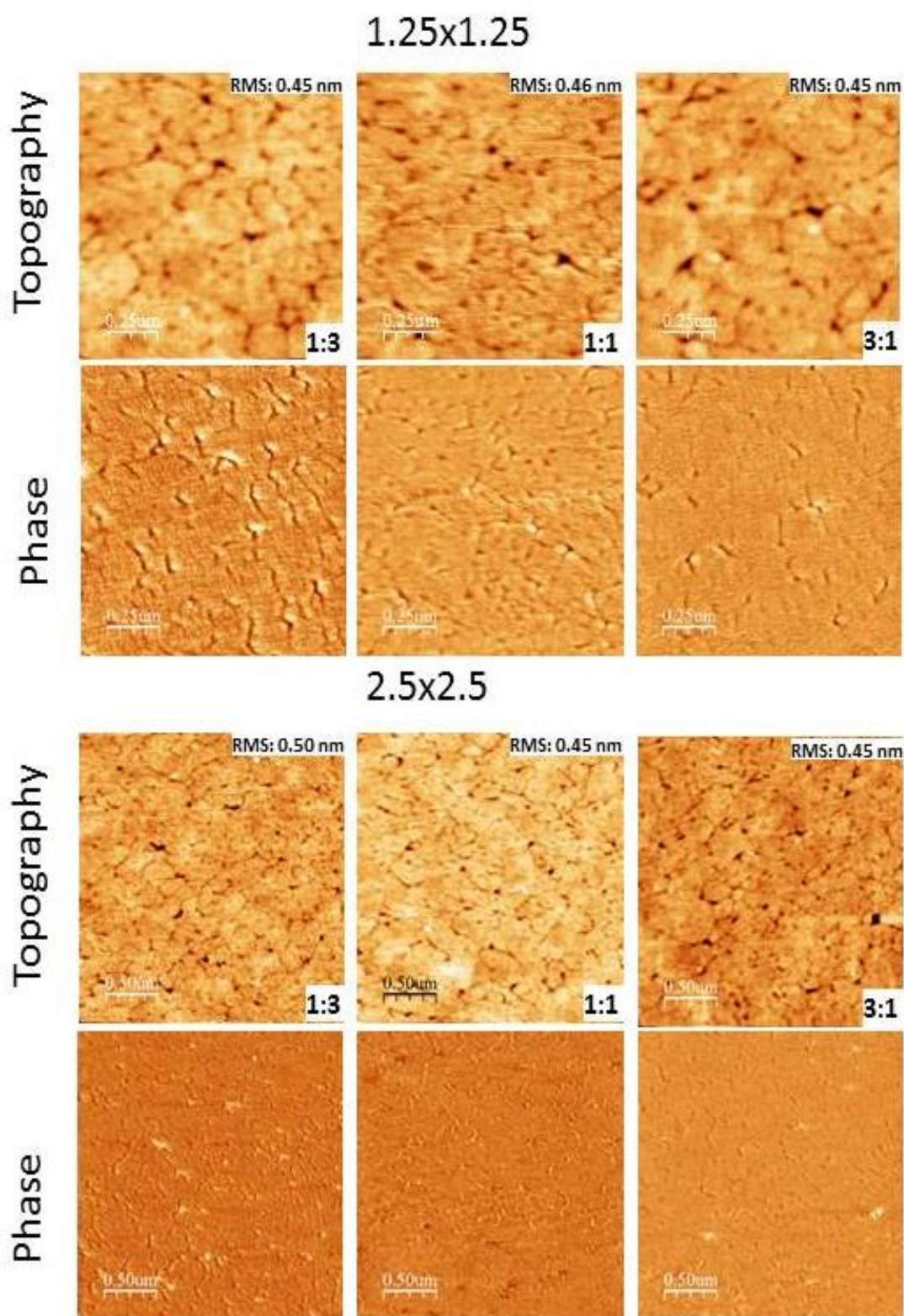


**Figure 61.** AFM images of Mixed M1:M9 SAMs on template stripped gold surface. Upper rows correspond to  $1.25 \times 1.25 \mu\text{m}^2$  and bottom rows  $2.5 \times 2.5 \mu\text{m}^2$ .

### 3.3.2.2 O1:M1 mixed SAMs

CAs and ellipsometric thickness of mixed O1:M1 films on TS-Au surfaces are summarized in **Figure 62** and **Table 13**. Though no clear trend was observed in CAs, the advancing CAs of all mixed O1:M1 SAMs were close to M1 as in the case of M1:M9 SAMs. The surface composition of mixed O1:M1 SAMs was determined by performing the same CA analysis procedure used for M1:M9 SAMs (as discussed in the previous section) and results are shown in **Figure 63**. When the analysis results for advancing CAs are considered it can be seen that for all solution ratios the surface fraction of M1 is higher than its solution fraction which implies preferential absorption of M1 over O1. However, for receding and static angles there was no such behavior which makes it difficult to derive a safe conclusion regarding the preferential absorption of M1 over O1. Nevertheless, since measurements performed in our group on O1:M1 mixed SAMs on FA-Au surfaces (which are not reported in this thesis) also indicate M1 to be dominant on the surface we believe this is also through for the SAMs on TS-Au surfaces studied here. **Figure 64** presents topography and phase images of mixed O1:M1 SAMs on TS-Au surfaces. The results of morphological analysis are summarized in **Table 14**. The morphological properties of O1:M1 SAMs are analogous to the properties of pure SAMs and are independent of the mixing ratios. It is worth to indicate that boundary length increases as M1 ratio decreases in growth solution.

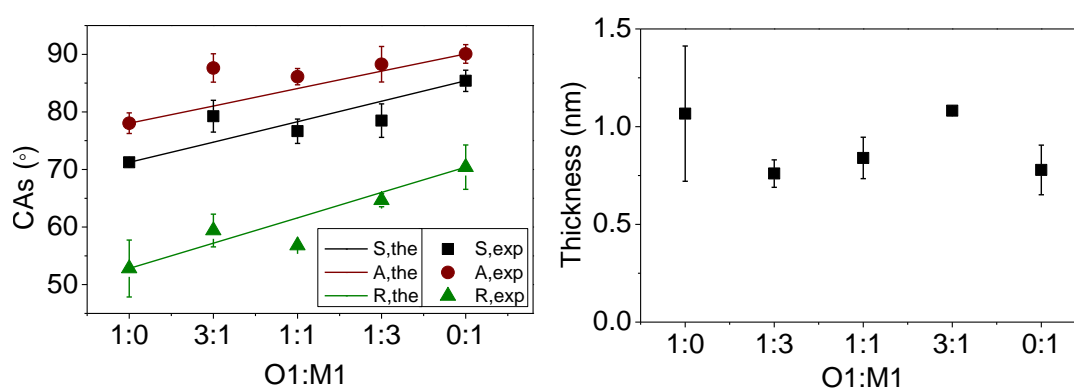


**Figure 62.** Contact angles and ellipsometric thicknesses of O1:M1 mixed SAMs. Lines in CAs indicate plotted theoretical CAs against  $q_{\text{surf}}$  by assuming surface fraction being equal to solution fraction. S: static, A: advancing and R: receding contact angles.

**Table 13.** Contact angles of O1:M1 mixed SAMs.

<i>O1:M1</i>	<i>Static</i>	<i>Advancing</i>	<i>Receding</i>	<i>Hysteresis</i>
<i>1:0</i>	71.2±0.7	78.0±1.8	52.8±4.9	25.2
<i>3:1</i>	79.3±2.8	87.6±2.5	59.4±2.8	28.2
<i>1:1</i>	76.6±2.1	86.1±1.4	56.8±0.3	29.3
<i>1:3</i>	78.5±2.9	88.3±3.1	64.7±1.1	23.6
<i>0:1</i>	85.4±1.8	90.1±1.6	70.4±3.9	19.7

**Table 14.** Results of the AFM image and contact angle analysis of O1:M1 SAMs.

<i>O1:M1</i>	<i>Results of the AFM image analysis</i>		
	<i>Average roughness (nm)</i>	<i>Average domain boundary length (<math>\mu\text{m}</math>)</i>	<i>Average defect coverage (%)</i>
<i>1:0</i>	0.59±0.05/0.48±0.11	12.3±2.3/77.7±23.1*	5.13±1.54/6.87±0.245
<i>3:1</i>	0.39±0.12/0.40±0.10	13.7±1.5/73.1±3.21	4.69±0.90/7.34±0.75
<i>1:1</i>	0.52±0.07/0.52±0.06	13.2±0.9/63.6±9.54	5.44±0.22/5.86±0.74
<i>1:3</i>	0.47±0.01/0.58±0.14	10.2±0.8/44.3±24.2*	4.66±0.58/5.68±2.55
<i>0:1</i>	0.53±0.14/0.54±0.10	14.3±4.5/48.4±4.27	4.49±0.67/4.53±0.10

\* High standard deviation is due to noise level and/or artifact of the images.

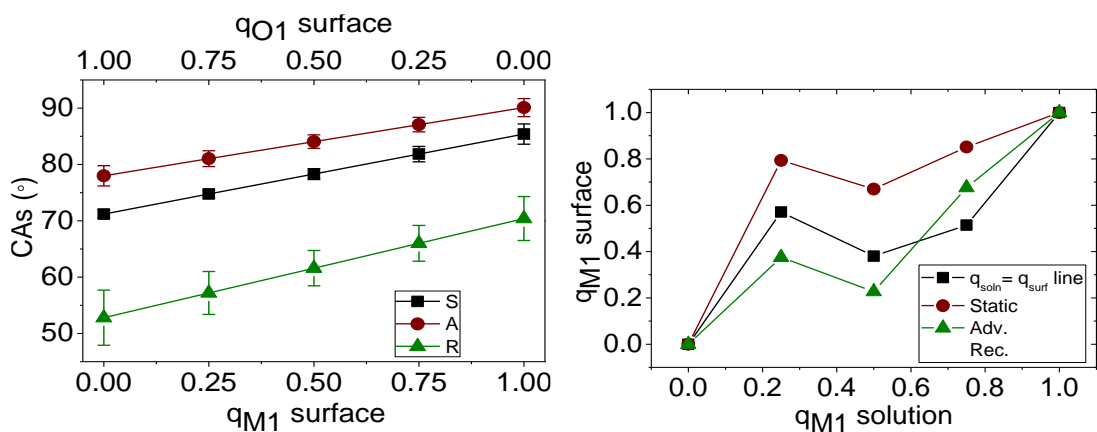


**Figure 63.** A) Theoretical contact angles as a function of surface composition for mixed O1:M1 SAMs. B) Surface composition of mixed O1:M1 SAMs calculated from the observed contact angles, plotted as a function of growth solution composition. S: static, A: advancing and R: receding contact angles.

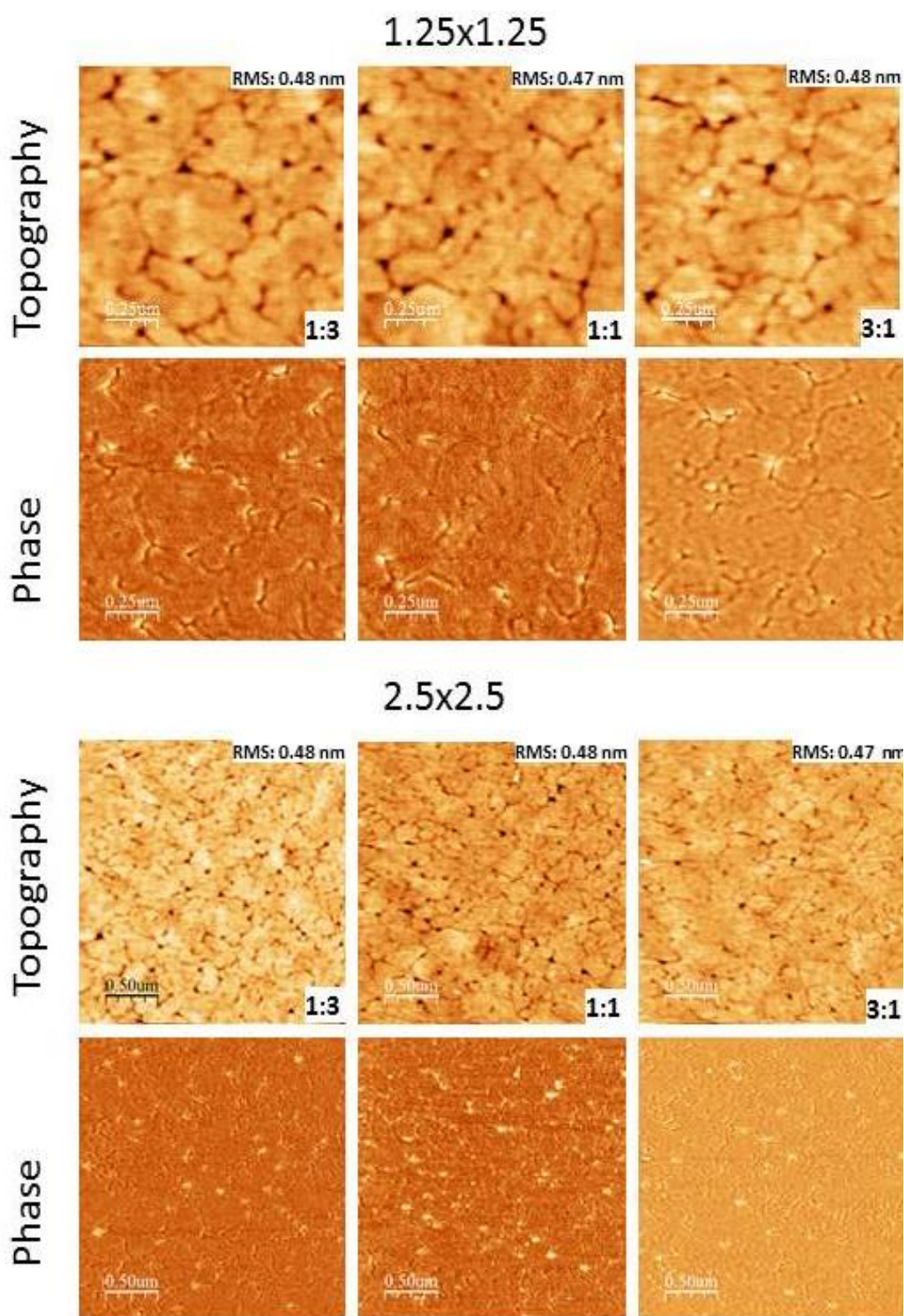


**Figure 64.** AFM images of mixed O1:M1 SAMs on template stripped gold surface. Upper rows correspond to  $1.25 \times 1.25 \mu\text{m}^2$  and bottom rows  $2.5 \times 2.5 \mu\text{m}^2$ .

### 3.3.2.3 O1:M9 mixed SAMs

CAs and ellipsometric thickness of mixed O1:M9 films on TS-Au surfaces are shown in **Figure 65** and **Table 15**. Contact angles of O1:M1 mixed SAMs.. CAs values of mixed SAMs lies between the pure SAMs except for receding angles. Since receding angles of the pure M1 and O1 SAMs are very close to each other and their standard deviations are high it is not reasonable to derive conclusions based on receding angles. Hence a surface composition analysis was performed based only on advancing and static angles results of which are shown in **Figure 66**. Interestingly, advancing and static angles show just the opposite trends when **Figure 66 B** is examined. It is also interesting to note that surface composition of O1 and M9 is calculated to be about 50% for 1:1 O1:M9 ratio growth solution. In addition, when **Figure 65** is examined it can be observed that the experimental CAs follow the theoretical lines very well (especially when the standard deviations of the data is considered) which implies that there is no preferential absorption of one the isomers over the other one. This observation may support our hypothesis that these two derivatives may have dipole-dipole interactions on surface. Representative AFM images of O1:M1 mixed SAMs are shown in **Figure 67** and their morphological properties are summarized in **Table 16** . Although the roughness are analogous to pure CTs SAMs and O1:M1 and M1:M9 mixed SAMs, the defect coverage and domain boundary lengths are smaller.

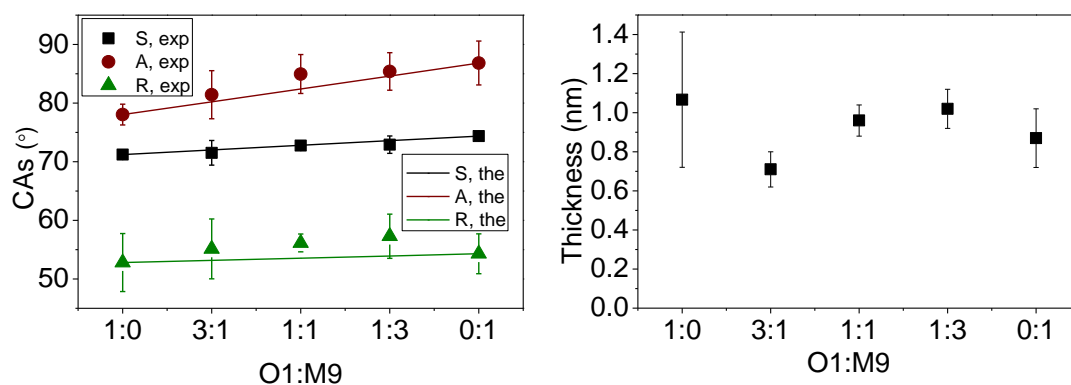


**Figure 65.** Contact angles and ellipsometric thicknesses of O1:M9 mixed SAMs. Lines in the CAs plot indicate theoretical CAs plotted by assuming surface fraction being equal to solution fraction. S: static, A: advancing and R: receding contact angles

**Table 15.** Contact angles of O1:M1 mixed SAMs.

<i>O1:M9</i>	<i>Static</i>	<i>Advancing</i>	<i>Receding</i>	<i>Hysteresis</i>
<i>1:0</i>	71.2±0.7	78.0±1.8	52.8±4.9	25.2
<i>3:1</i>	71.5±2.1	81.4±4.1	55.1±5.1	26.3
<i>1:1</i>	72.7±0.7	85.0±3.3	56.2±1.5	28.8
<i>1:3</i>	72.9±1.5	85.4±3.2	57.3±3.8	28.1
<i>0:1</i>	74.4±0.3	86.8±3.7	54.3±3.4	32.5

**Table 16.** Results of the AFM image and contact angle analysis of M1:M9 SAMs.

<i>Results of the AFM image analysis</i>			
<i>O1:M9</i>	<i>Average roughness (nm)</i>	<i>Average domain boundary length (<math>\mu\text{m}</math>)</i>	<i>Average defect coverage (%)</i>
<i>1:0</i>	0.59±0.05/0.48±0.11	12.3±2.26/77.7±23.1*	5.13±1.54/6.87±0.245
<i>3:1</i>	0.39±0.09/0.50±0.10	11.7±0.72/71.6±4.48	3.06±2.06/7.22±0.86
<i>1:1</i>	0.47±0.0/0.55±0.06	8.02±0.01/58.4±2.23	2.97±0.21/6.10±0.39
<i>1:3</i>	0.49±0.06/0.61±0.20	12.7±4.93/63.4±3.97	4.13±1.15/7.07±0.96
<i>0:1</i>	0.42±0.14/0.46±0.19	15.6±1.97/69.9±21.2*	4.49±0.67/5.40±1.57

\* High standard deviation is due to noise level and/or artifact of the images.

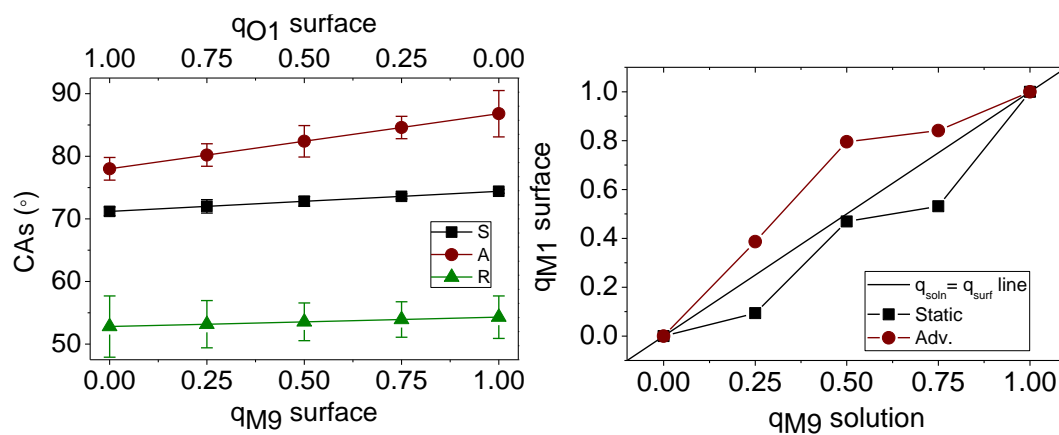


**Figure 66.** A) Theoretical contact angles as a function of surface composition for mixed O1:M9 SAMs. B) Surface composition of mixed O1:M9 SAMs calculated from the observed contact angles, plotted as a function of growth solution composition. S: static, A: advancing and R: receding contact angles.

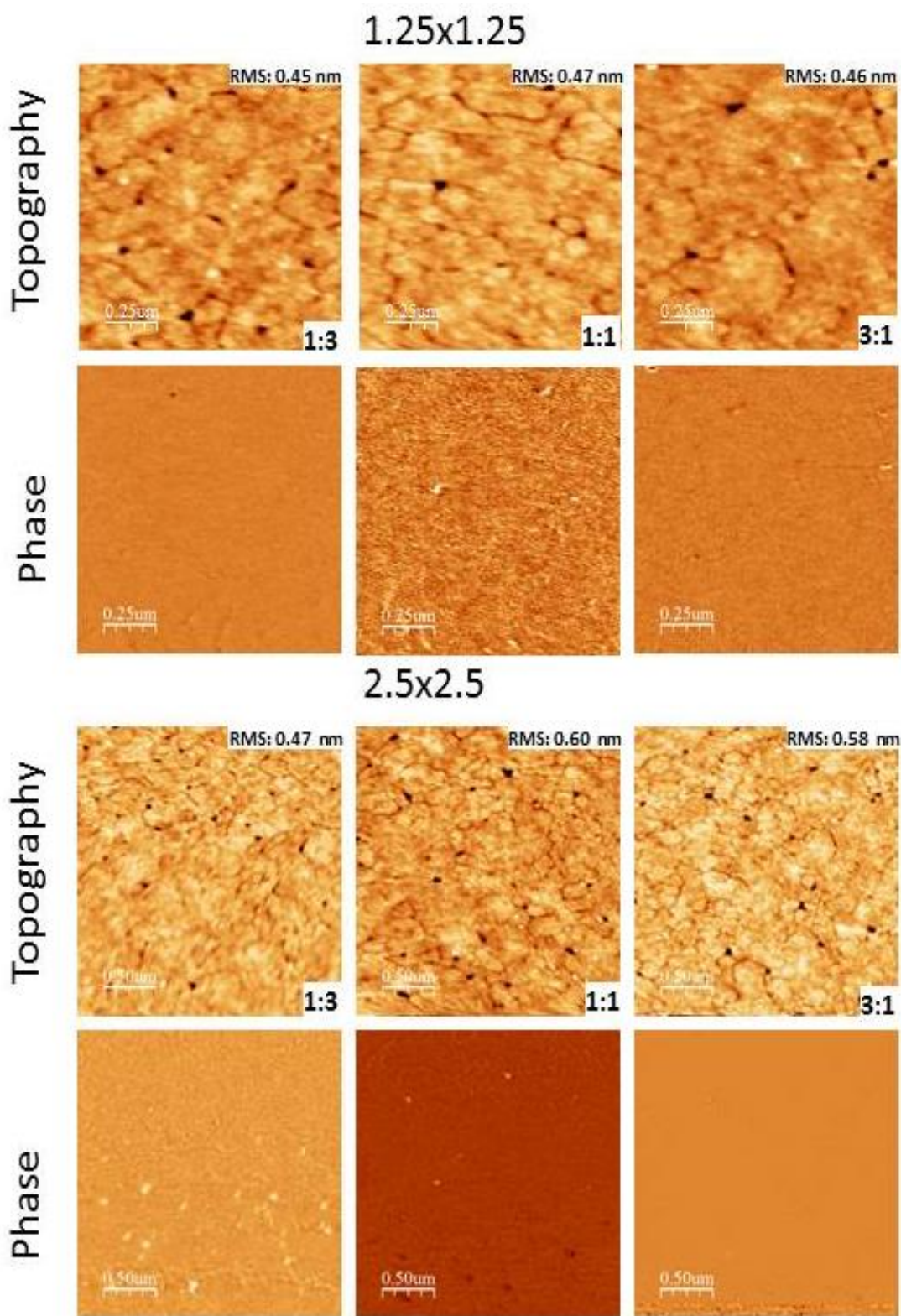


**Figure 67.** AFM images of Mixed O1:M1 SAMs on template stripped gold surface. Upper rows correspond to  $1.25 \times 1.25 \mu\text{m}^2$  and bottom rows  $2.5 \times 2.5 \mu\text{m}^2$ .

### 3.4 Summary

When the results discussed above are considered it may be useful to summarize some general observations. The CAs as well as ellipsometric thickness of reference alkanethiol SAMs were in agreement with literature values which proves the reliability of our measurements on CT SAMs. [ 85,87,88-92] Results obtained for CT SAMs can be rationalized as follows. Based on CAs results, for all co-deposited SAMs of M1 with M9 surface wettability mostly governed by M1 which binds to surface more preferentially. In case of O1:M1 films the dominance of M1 is obvious considering advancing contact angles, however, based on the static and receding contact angles such behavior was not observed. The dominance of M1 on surface is in agreement with the previous studies which explained this preferential binding by head-to-tail dipole-dipole interactions of M1 molecules on the surface. [107] In case of O1:M9 films however, surface fraction of the isomers follows the solution fractions which implies that there is no preferential adsorption of any of the components. This may be due to dipole-dipole interaction between O1 and M9 molecules on the surface. In fact, this dipole-dipole interaction can result in alternating anchoring of molecules on the surface and homogeneous film formation in molecular scale as depicted in **Figure 68**. In addition, comparing the morphological properties of mixed SAMs (see **Figure 69**), it can be seen that defect coverage is lower in O1:M9 mixed SAMs which may be due to the dipole-dipole interaction of M9 and O1. Besides these, all carboranethiol SAMs have similar morphological properties with surface roughness around 0.5 nm, domain boundary length in range of 10 and 20  $\mu\text{m}$  and defect coverage around 5%. The pits that were observed in AFM images have about 3 nm depth which are much higher than the depth of characteristic vacancy island (or etch pits) observed in alkanethiol SAMs. Although the size of the pits that we observed in carboranethiol SAMs are much larger than the size of vacancy islands of alkanethiol SAMs reported in the literature, their coverage is close to pit coverage of 6% to 9% reported by Poirier for several different alkanethiol SAMs. Nevertheless, the pits that are observed for carboranethiol SAMs most probably have different nature than those observed in alkanethiol SAMs and may

be originating from defects on template stripped gold substrate. In fact, in STM studies of M1, M9 and p-carboxyl-carbotanethiols no etch pit formation was reported by Weiss and co-workers. [105,113] On the other hand, STM image of p-carboranethiol derivatives (which contain alkane chains as spacer) shows formation etch pit like 3-4 nm vacancies due to partial absorption. [114,115]

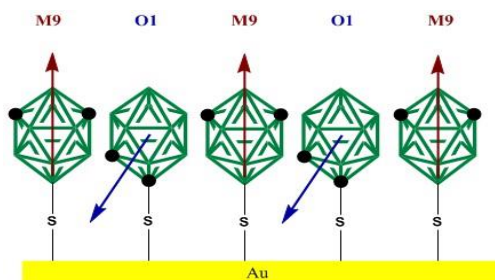


**Figure 68.** Schematic representation O1:M9 dipole-dipole interaction on surface

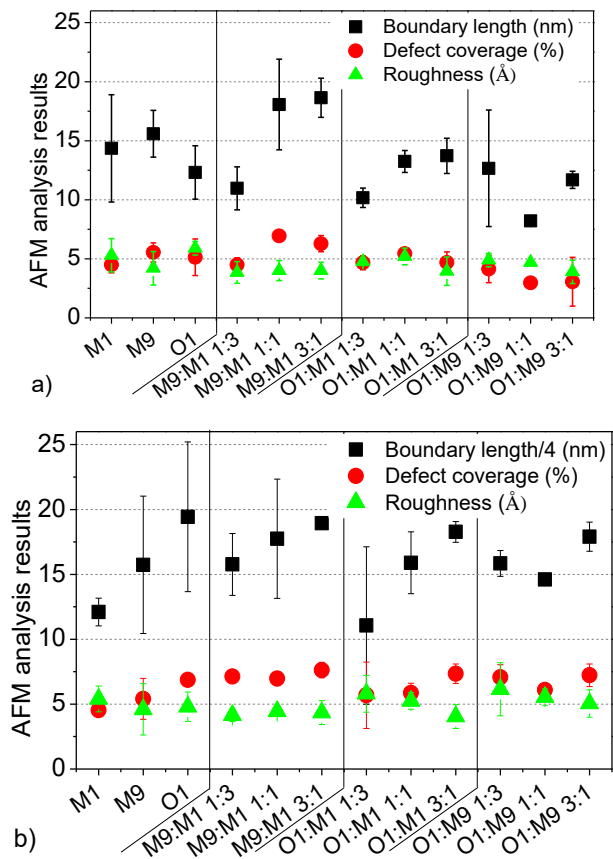


**Figure 69.** Summary of the AFM image analysis results performed on 1.25 μm x 1.25 μm images (a) and 2.5 μm x 2.5 μm images (b). Boundary lengths in (b) is divided by 4 for comparison with (a).



## CHAPTER 4

### CONCLUSION

In this study SAMs of three positional isomers of pure carboranethiols (M1, M9 and O1) as well as their corresponding mixed SAMs were investigated on template stripped gold surfaces. The ellipsometric thickness of SAMs was measured to be around 1 nm for all SAMs on both substrates. The ellipsometric thicknesses of SAMs are consistent with the thicknesses measured with STM in the literature. [107] The wetting properties of SAMs was investigated via contact angle (CA) measurements. Among pure SAMs, M1 films was found to be more hydrophobic than O1 and M9 films. O1 films have the lowest CA compared to other pure SAMs. Moreover, mixed SAMs of these isomers with different mixing ratios were studied. Based on CA analysis of contact angle results, surface fraction of M1 was found to be higher than its solution fraction for all growth solution ratio of M1:M9 which indicates the dominant component on the surface to be M1. The dominance of M1 on surface was also observed for O1:M1 mixed SAM, though the trend was not as clear as observed for M1:M9 SAMs. In case of O1:M9 modified surface CAs decrease with increasing O1 ratio in the growth solution. However, it is very difficult to judge the dominance of one of the species on the other on the surface based on CAs since the CAs of pure O1 and M9 SAMs are very close to each other. Lastly the morphology of SAMs was investigated by AFM. The topographic images of all SAMs are similar to each other except O1:M9 SAMs. In fact, based on AFM image analysis the O1:M9 mixed SAMs have lower defect coverage relative to pure and other mixed SAMs. No phase separation was observed for mixed SAMs which implies homogeneity of the films.



## REFERENCES

- (1) Gaines, G. L. *Journal of Colloid and Interface Science*. 1991, 149 (1), 301-302.
- (2) L. C. F. Blackman and M. J. S. Dewa. *J. Chem. Soc.* **1957**, 35 (162), 162–165.
- (3) Laibinis, P. E.; Bain, C. D.; Whitesides, G. M. *J. Phys. Chem.* **1991**, 95 (18), 7017–7021.
- (4) Zwahlen, M.; Tosatti, S.; Textor, M.; Hähner, G. *Langmuir* **2002**, 18 (10), 3957–3962.
- (5) Xia, Y.; Kim, E.; Mrksich, M.; Whitesides, G. M. *Chem. Mater.* **1996**, 8 (3), 601–603.
- (6) Tosatti, S.; Michel, R.; Textor, M.; Spencer, N. D. *Langmuir* **2002**, 18 (9), 3537–3548.
- (7) Schreiber, F. *Prog. Surf. Sci.* **2000**, 65 (5–8), 151–256.
- (8) Schlotter, N. E.; Porter, M. D.; Bright, T. B.; Allara, D. L. *Chem. Phys. Lett.* **1986**, 132 (1), 93–98.
- (9) Nuzzo, R. G.; Allara, D. L. *J. Am. Chem. Soc.* **1983**, 105 (13), 4481–4483.
- (10) Kim, S.; Choi, G. Y.; Ulman, A.; Fleischer, C. *Langmuir* **1997**, 13 (25), 6850–6856.
- (11) Sigal, G. B.; Bamdad, C.; Barberis, A.; Strominger, J.; Whitesides, G. M. *Anal. Chem.* **1996**, 68 (3), 490–497.
- (12) Malem, F.; Mandler, D. *Anal. Chem.* **1903**, 65 (12), 37–41.
- (13) Sabapathy, R. C.; Crooks, R. M. *Langmuir* **2000**, 16 (4), 1777–1782.
- (14) Leatherman, G.; Durantini, E. N.; Gust, D.; Moore, T. A.; Moore, A. L.; Stone, S.; Zhou, Z.; Rez, P.; Liu, Y. Z.; Lindsay, S. M. *J. Phys. Chem. B* **1999**, 103 (20), 4006–4010.
- (15) Sachs, S. B.; Dudek, S. P.; Hsung, R. P.; Sita, L. R.; Smalley, J. F.; Newton, M. D.; Feldberg, S. W.; Chidsey, C. E. D. *J. Am. Chem. Soc.* **1997**, 119 (11), 10563–10564.
- (16) Kobayashi, K.; Umemura, J.; Horiuchi, T.; Yamada, H.; Matsushige, K.

- Japanese J. Appl. Physics, Part 2 Lett.* **1998**, 37 (3 A).
- (17) Rodriguez, K. R.; Shah, S.; Williams, S. M.; Teeters-Kennedy, S.; Coe, J. V. *J. Chem. Phys.* **2004**, 121 (18), 8671–8675.
- (18) Wiedemair, J.; Le Thi Ngoc, L.; Van Den Berg, A.; Carlen, E. T. *J. Phys. Chem. C* **2014**, 118 (22), 11857–11868.
- (19) Wiedemair, J.; Le Thi Ngoc, L.; Van Den Berg, A.; Carlen, E. T. *J. Phys. Chem. C* **2014**, 118 (22), 11857–11868.
- (20) Fenter, P.; Eisenberger, P.; Liang, K. S. *Phys. Rev. Lett.* **1993**, 70 (16), 2447–2450.
- (21) Bracco, G.; Scoles, G. *J. Chem. Phys.* **2003**, 119 (12), 6277.
- (22) Becker, J. S.; Brown, R. D.; Johansson, E.; Lewis, N. S.; Sibener, S. J. *J. Chem. Phys.* **2010**, 133 (2010), 104705.
- (23) Barrena, E.; Ocal, C.; Salmeron, M. *Surf. Sci.* **2001**, 482–485, 1216–1221.
- (24) Riet, J.; Smit, T.; Coenen, M. J. J.; Gerritsen, J. W.; Cambi, A.; Elemans, J. A. W.; Speller, S.; Figdor, C. G. *Soft Matter* **2010**, 6, 3450.
- (25) Xu, G.; Woodruff, D. P.; Bennett, N.; Elliott, M.; MacDonald, J. E. *Langmuir* **2010**, 26 (11), 8174–8179.
- (26) Lüssem, B.; Müller-Meskamp, L.; Karthäuser, S.; Waser, R.; Homberger, M.; Simon, U. *Langmuir* **2006**, 22 (7), 3021–3027.
- (27) Dubois, H.; Laboratories, T. B.; Hill, M.; Nuzzo, R. G. *J. Am. Chem. Soc.* **1992**, 112 (5), 558–569.
- (28) Laibinis, P. E.; Whitesides, G. M. *J. Am. Chem. Soc.* **1992**, 114, 9022–9028.
- (29) Hsu, C.; Marcus, R. *J. Chem. Phys.* **1997**, 106 (2), 584–598.
- (30) Lautz, C.; Fischer, T. M.; Weygand, M.; Lösche, M.; Howes, P. B.; Kjaer, K. *J. Chem. Phys.* **1998**, 108 (11), 4640–4646.
- (31) Camillone III, N.; Chidsey, C. E. D.; Liu, G.-Y.; Scoles, G. *J. Chem. Phys.* **1993**, 98 (5), 4234–4245.
- (32) Nuzzo, R. G.; Korenic, E. M.; Dubois, L. H. *J. Chem. Phys.* **1990**, 93 (1), 767.
- (33) Love, J. C.; Estroff, L. A.; Kriebel, J. K.; Nuzzo, R. G.; Whitesides, G. M. *Self-assembled monolayers of thiolates on metals as a form of nanotechnology*;

2005; Vol. 105.

- (34) De Renzi, V.; Di Felice, R.; Marchetto, D.; Biagi, R.; del Pennino, U.; Selloni, A. *J. Phys. Chem. B* **2004**, *108* (111), 16–20.
- (35) Chaudhuri, A.; Lerotholi, T. J.; Jackson, D. C.; Woodruff, D. P.; Jones, R. G. *Phys. Rev. B - Condens. Matter Mater. Phys.* **2009**, *79* (19), 1–7.
- (36) Tang, L.; Li, F.; Zhou, W.; Guo, Q. *Surf. Sci.* **2012**, *606* (5–6), L31–L35.
- (37) Li, F.; Tang, L.; Gao, J.; Zhou, W.; Guo, Q. *Langmuir* **2012**, *28* (30), 11115–11120.
- (38) Li, F.; Tang, L.; Voznyy, O.; Gao, J.; Guo, Q. *J. Chem. Phys.* **2013**, *138* (19), 194707.
- (39) Maksymovych, P.; Sorescu, D. C.; Jordan, K. D.; Yates, J. T. *Science* (80-. ). **2008**, *322* (5908), 1664–1667.
- (40) Maksymovych, P.; Sorescu, D. C.; Yates, J. T. *Phys. Rev. Lett.* **2006**, *97* (14), 1–4.
- (41) Cavanna, D.; Bracco, G.; Renzi, V. De; Corradini, V.; Biagi, R.; del Pennino, U. *J. Phys. Condens. Matter* **2007**, *19* (30), 305019.
- (42) Gao, J.; Li, F.; Guo, Q. *Langmuir* .**2013**, *29* (35), pp 11082–11086.
- (43) Cossaro, A; Mazzarello, R.; Rousseau, R.; Casalis, L.; Verdini, A; Kohlmeyer, A; Floreano, L.; Scandolo, S.; Morgante, A; Klein, M. L.; Scoles, G. *Science* (80). **2008**, *321* (5891), 943–946.
- (44) Knoppe, S.; Burgi, T. *Acc. Chem. Res.* **2014**, *47* (4), 1318–1326.
- (45) Pablo,D; Guillermo,C; Christopher,J; David ,A; Roger ,D; *Science* (321). **2007**, *5891*, 430–433.
- (46) Bau, R. *J. Am. Chem. Soc.* **1998**, *120* (36), 9380–9381.
- (47) Bürgi, T. *Nanoscale* **2015**, *7* (38), 15553–15567.
- (48) Bertilsson, L.; Liedberg, B. *Langmuir* **1993**, *9* (1), 141–149.
- (49) Nuzzo, R. G.; Dubois, L. H.; Allara, D. L. *J. Am. Chem. Soc.* **1990**, *112*, 558–569.
- (50) G. E. Poirier;J. M. White, E. D. P. *J. Chem. Phys.* **1996**, *105* (5), 2089.
- (51) Himmel, H. J.; Weiss, K.; Jäger, B.; Dannenberger, O.; Grunze, M.; Wöll, C.

- Langmuir* **1997**, *13* (10), 4943–4947.
- (52) Vericat, C.; Vela, M. E.; Benitez, G.; Carro, P.; Salvarezza, R. C. *Chem. Soc. Rev.* **2010**, *39* (5), 1805–1811.
- (53) Wolfschmidt, H.; Baier, C.; Gsell, S.; Fischer, M.; Schreck, M.; Stimming, U. *Materials (Basel)*. **2010**, *3* (8), 4196–4213.
- (54) Uro, M.; Odon P.; Abdelrahim, H.; Miran G. *Acta Chim. Slov.* **2012**, *59*, 212–219.
- (55) Whitesides, G. M.; Kriebel, J. K.; Love, J. C. *Sci. Progress.* **2005**, *88* (Pt 1), 17–48.
- (56) Mamun, A. H. Al; Hahn, J. R. *J. Phys. Chem. C* **2012**, *116* (42), 22441–22448.
- (57) Schönenberger, C.; Sondag-Huethorst, J. A. M.; Jorritsma, J.; Fokkink, L. G. J. *Langmuir* **1994**, *10* (3), 611–614.
- (58) Li, Y.; Yu, D.; Dai, L.; Urbas, A.; Li, Q. *Langmuir* **2011**, *27* (1), 98–103.
- (59) Li, G.; Li, X.; Yang, M.; Chen, M.-M.; Chen, L.-C.; Xiong, X.-L. *Sensors (Basel)*. **2013**, *13* (10), 12794–12803.
- (60) Li, F.; Tang, L.; Zhou, W.; Guo, Q. *Langmuir* **2010**, *26* (12), 9484–9490.
- (61) Zhou, J. G.; Hagelberg, F. *Phys. Rev. Lett.* **2006**, *97* (4), 12–15.
- (62) Wang, T.; Kafle, T. R.; Kattel, B.; Liu, Q.; Wu, J.; Chan, W.-L. *Sci. Rep.* **2016**, *6* (March), 28895.
- (63) Murphy, C. J.; Shi, X.; Jewell, A. D.; McGuire, A. F.; Bellisario, D. O.; Baber, A. E.; Tierney, H. L.; Lewis, E. A.; Sholl, D. S.; Sykes, E. C. H. *J. Chem. Phys.* **2015**, *142* (10).
- (64) Li, F.; Tang, L.; Zhou, W.; Guo, Q. *Phys. Chem. Chem. Phys.* **2011**, *13* (25), 11958–11964.
- (65) Ohring, M. *The Materials Science of Thin Films*, 1st ed.; Academic Press: Boston, 1992.
- (66) Maver, U.; Maver, T.; Persin, Z.; Mozetic, M.; Vesel, A.; Gaberscek, M.; Stana-Kleinschek, K. *Polymer characterization with the atomic force microscope*; 2013.
- (67) Sayed, S. Y.; Wang, F.; Malac, M.; Meldrum, A.; Egerton, R. F.; Buriak, J. M.

- ACS Nano* **2009**, *3* (9), 2809–2817.
- (68) Moazzez, B.; O'Brien, S. M.; Merschrod S, E. F. *Sensors (Basel)*. **2013**, *13* (6), 7021–7032.
- (69) Maver, Uroš. Planinšek, Odon. Jamnik, Janko. Hassanien, Abdelrahim Ibrahim. Gaberšček, M. *Acta Chim. Slov.* **2012**, *59* (1), 212–219.
- (70) De Los Santos, V. L.; Lee, D.; Seo, J.; Leon, F. L.; Bustamante, D. A.; Suzuki, S.; Majima, Y.; Mitrelias, T.; Ionescu, A.; Barnes, C. H. W. *Surf. Sci.* **2009**, *603* (19), 2978–2985.
- (71) Dishner, M. H. *J. Vac. Sci. Technol. A Vacuum, Surfaces, Film.* **1998**, *16* (6), 3295–3300.
- (72) Ren, B.; Picardi, G.; Pettinger, B. *Rev. Sci. Instrum.* **2004**, *75* (4), 837–841.
- (73) Lipkowski, J. *Phys. Chem. Chem. Phys.* **2010**, *12* (42), 13874–13887.
- (74) Metering, S. *Director* **2007**, 365–371.
- (75) Barkai, M.; Deutscher, G. *Thin Solid Films*, **1982**, *90*, 85–90.
- (76) Levlin, M.; Laakso, A.; Niemi, .-M; Hautojarvi, P. *Appl. Surf. Sci.* **1997**, *115*, 31–38.
- (77) Li, M.; Chen, M.; Sheepwash, E.; Brosseau, C. L.; Li, H.; Pettinger, B.; Gruler, H.; Lipkowski, J. *Langmuir* **2008**, *24* (18), 10313–10323.
- (78) Vogel, N.; Zieleniecki, J.; Köper, I. *Nanoscale* **2012**, *4* (13), 3820.
- (79) Weiss, Emily .Kaufman, George.Kriebel, Jennah.Li, Zhefeng.Whitesides, G. *Langmuir* **2007**, *23* (19), 9686–9694.
- (80) Wagner, P.Hegner, M.Guntherodt, HJ.Semenza, G. *Langmuir* **1995**, *11* (10), 3867–3875.
- (81) Banner, L. T.; Richter, A.; Pinkhassik, E. *Surf. Interface Anal.* **2009**, *41* (1), 49–55.
- (82) Miura, Y. F.; Takenaga, M.; Koini, T.; Graupe, M.; Garg, N.; Graham, R. L. J.; Lee, T. R. *Langmuir* **1998**, *14* (20), 5821.
- (83) Bain, C. D.; Troughton, E. B.; Tao, Y. T.; Evall, J.; Whitesides, G. M.; Nuzzo, R. G. *J. Am. Chem. Soc.* **1989**, *111* (1), 321–335.
- (84) Folkers, J. P.; Laibinis, P. E.; Whitesides, G. M. *J. Adhes. Sci. Technol.* **1992**, *6*

- (12), 1397–1410.
- (85) Biebuyck, H. A.; Bain, C. D.; Whitesides, G. M. *Langmuir* **1989**, *5*, 723–727.
- (86) Bracco, G.; Holst, B. *Surface Science Techniques*; 2013; Vol. 51.
- (87) Newcomb, L. B.; Tevis, I. D.; Atkinson, M. B. J.; Gathiaka, S. M.; Luna, R. E.; Thuo, M. *Langmuir* **2014**, *30* (40), 11985–11992.
- (88) Chen, J.; Wang, Z.; Oyola-Reynoso, S.; Gathiaka, S. M.; Thuo, M. *Langmuir* **2015**, *31* (25), 7047–7054.
- (89) Folkers, J. P.; Laibinis, P. E.; Whitesides, G. M. *Langmuir* **1992**, *8* (5), 1330–1341.
- (90) Christopher Love, J.; Wolfe, D. B.; Haasch, R.; Chabinyc, M. L.; Paul, K. E.; Whitesides, G. M.; Nuzzo, R. G. *J. Am. Chem. Soc.* **2003**, *125* (9), 2597–2609.
- (91) Schwartz, D. K. *Annu. Rev. Phys. Chem.* **2001**, *52*, 107–137.
- (92) Ulman, A. *Chem. Rev.* **1996**, *96* (4), 1533–1554.
- (93) Guo, Q.; Li, F. *Phys. Chem. Chem. Phys.* **2014**, *16*, 19074–19090.
- (94) Voznyy, O.; Dubowski, J. J.; Yates, J. T.; Maksymovych, P. *J. Am. Chem. Soc.* **2009**, *131* (36), 12989–12993.
- (95) Gao, J.; Li, F.; Guo, Q. *J. Phys. Chem. C* **2013**, *117* (47), 24985–24990.
- (96) Alves, C. A.; Smith, E. L.; Porter, M. D. *J. Am. Chem. Soc.* **1992**, *114* (4), 1222–1227.
- (97) Fukuma, T.; Kobayashi, K.; Horiuchi, T.; Yamada, H.; Matsushige, K. *Appl. Phys. A* **2001**, *112*, 109–112.
- (98) Tamada, K.; Hara, M.; Sasabe, H.; Knoll, W. *Langmuir* **1997**, *13* (6), 1558–1566.
- (99) Huckstadt, C. Schmidt, S. Hufner, S. Forster, F. Reinert, F. Springborg, M. *Phys. Rev. B Condens. Matter* **2006**, *73* (10), 75409.
- (100) Evans, S. D.; Ulman, A. *Chemical Physics Letters* **1990**, *170* (5), 462–466.
- (101) Evans, S. D.; Urankar, E.; Ulman, A.; Ferris, N. *J. Am. Chem. Soc.* **1991**, *113* (11), 4121–4131.
- (102) Lee, H. J.; Jamison, A. C.; Lee, T. R. *Acc. Chem. Res.* **2015**, *48* (12), 3007–3015.

- (103) Chen, W.; Huang, C.; Gao, X. Y.; Wang, L.; Zhen, C. G.; Qi, D.; Chen, S.; Zhang, H. L.; Loh, K. P.; Chen, Z. K.; Wee, A. T. S. *J. Phys. Chem. B* **2006**, *110* (51), 26075–26080.
- (104) Base, T.; Bastl, Z.; Plzak, Z.; Grygar, T.; Plesek, J.; Carr, M. J.; Malina, V.; Subrt, J.; Bohacek, J.; Vecernikova, E.; Kriz, O. *Langmuir* **2005**, *21* (6), 7776–7785.
- (105) Hohman, J. N.; Zhang, P.; Morin, E. I.; Han, P.; Kim, M.; Kurland, A. R.; McClanahan, P. D.; Balema, V. P.; Weiss, P. S. *ACS Nano* **2009**, *3* (3), 527–536.
- (106) Kim, J.; Rim, Y. S.; Liu, Y.; Serino, A. C.; Thomas, J. C.; Chen, H.; Yang, Y.; Weiss, P. S. *Nano Lett.* **2014**, *14* (5), 2946–2951.
- (107) Mete, E.; Yilmaz, A.; Danişman, M. F. *Phys. Chem. Chem. Phys.* **2016**, *18* (18), 12920–12927.
- (108) Guo, D.; Xie, G.; Luo, J. J. *Phys. D: Appl. Phys.* **2014**, *47*, 013001.
- (109) Viji, V. (2014). Ellipsometry-Nondestructive measuring method. Retrieved from <http://www.slideshare.net/foolishcrack/ellipsometry>.
- (110) O'Dwyer, C.; Gay, G.; Viaris De Lesegno, B.; Weiner, J. *Langmuir* **2004**, *20* (19), 8172–8182.
- (111) Bain, C. D.; Whitesides, G. M. *J. Am. Chem. Soc.* **1989**, *111* (18), 7155–7164.
- (112) Tachibana, M.; Yoshizawa, K.; Ogawa, A.; Fujimoto, H.; Hoffmann, R. J. *Phys. Chem. B.* **2002**, *106*, 12727–12736.
- (113) Thomas, J. C.; Boldog, I.; Auluck, H. S.; Bereciartua, P. J.; Dušek, M.; Macháček, J.; Bastl, Z.; Weiss, P. S.; Baše, T. *Chem. Mater.* **2015**, *27* (15), 5425–5435.
- (114) Von Wrochem, F.; Scholz, F.; Gao, D.; Nothofer, H. G.; Yasuda, A.; Wessels, J. M.; Roy, S.; Chen, X.; Michl, J. *J. Phys. Chem. Lett.* **2010**, *1* (24), 3471–3477.
- (115) Scholz, F.; Nothofer, H.; Wessels, J. M.; Nelles, G.; Wrochem, F. Von; Roy, S.; Chen, X.; Michl, J. *Journal of Physical Chemistry C* **2011**, *115* (46), 22998–23007.



## APPENDIX

### 1.1 Effect of polar aromatic containing SAMs on work function

Later studies on alkyl thiol monolayers containing a polar aromatic group indicated that the work function of the underlying metal strongly depends on the direction and the magnitude of the dipole moment of the SAM. Kelvin probe measurements that were used by Evans et al. highlighted the critical effect of organic adsorbate's structure on the magnitude and sign of the work function. They observed that changing the terminal groups from n-alkane chain to a fluoroalkyl one reverses the direction of net dipole moment. These relations can be seen in **Figure 70**. In other words, terminal fluoroalkyl raises the work function of gold by 0.75 eV, whereas, n-alkane terminated one decreases as much as 0.45 eV. These conclusions were confirmed by Sita and co-workers via arenethiols with different terminal functional groups. [101]

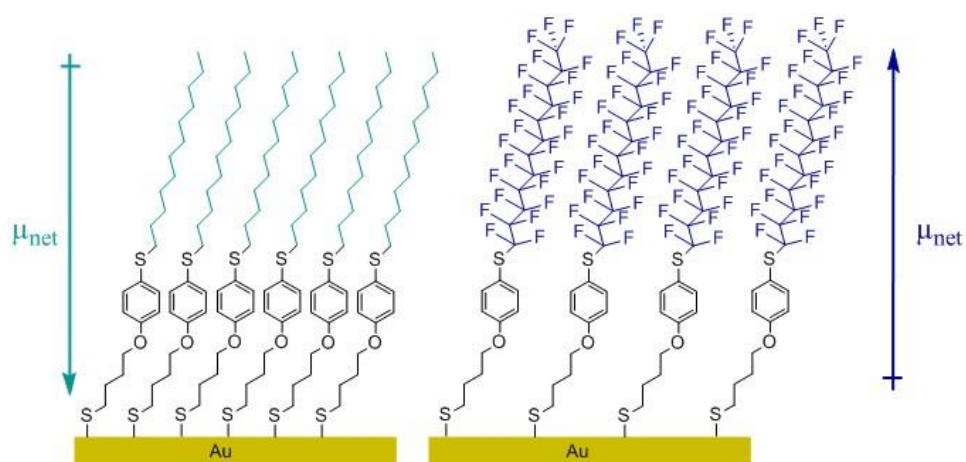


**Figure 70.** Gold decorated with polar aromatic groups. The structural differences as well as the direction of the dipole moments of corresponding organic adlayer is shown.

## 1.2 Effect of fluoroalkanethiol SAMs on work function

Aiming at bringing more clarity to the relationship between the work function of a coated surface and chemical composition of the SAM, the work function of gold surfaces modified with a series of alkanethiol SAMs ( $\text{CH}_3(\text{CH}_2)_n\text{SH}$  ( $n = 2, 7, 9,$  and  $17$ )) was investigated using UV-photospectroscopy (UPS) by Lee and coworkers. [102] It can be seen in the UV photoemission spectra (**Figure 71 A2**) that as alkyl chain length of the adsorbates increases, kinetic energy edge shifts to lower energies. The effect of direction and magnitude of dipoles from an array of adsorbate dipoles on the work function of metals was demonstrated considering an estimation of difference in the work function,  $\Delta W$ , between bare and SAM-modified gold surfaces which are depicted in **Figure 71 A3**. They also used a series of fluorocarbon-terminated SAMs ( $\text{CF}_3(\text{CF}_2)_n(\text{CH}_2)_{15-n}\text{SH}$ ,  $n = 0, 1, 3,$  and  $9$ ; **Figure 71 B1**) in order to investigate the influence of the direction of surface dipoles. The surface dipoles for these fluorocarbon-terminated gold surfaces exhibited a polarity opposite to the surface dipoles associated with the hydrocarbon-terminated gold surfaces (i.e., those coated with n-alkanethiol SAMs) as in the case of polar aromatic ones. It was observed that bare gold surface had higher kinetic energy edge position than those of  $\text{H}_{16}$ - and  $\text{F}_1\text{H}_5$ -modified gold surfaces and lower energy edge position compared to  $\text{F}_2\text{H}_{14}$ -,  $\text{F}_4\text{H}_{12}$ -, and  $\text{F}_{10}\text{H}_6$ - modified ones (**Figure 71 B2**). With an increasing number of fluorocarbons the work function of the fluorocarbon-terminated surfaces increased as well and this is depicted in **Figure 71 B3**.

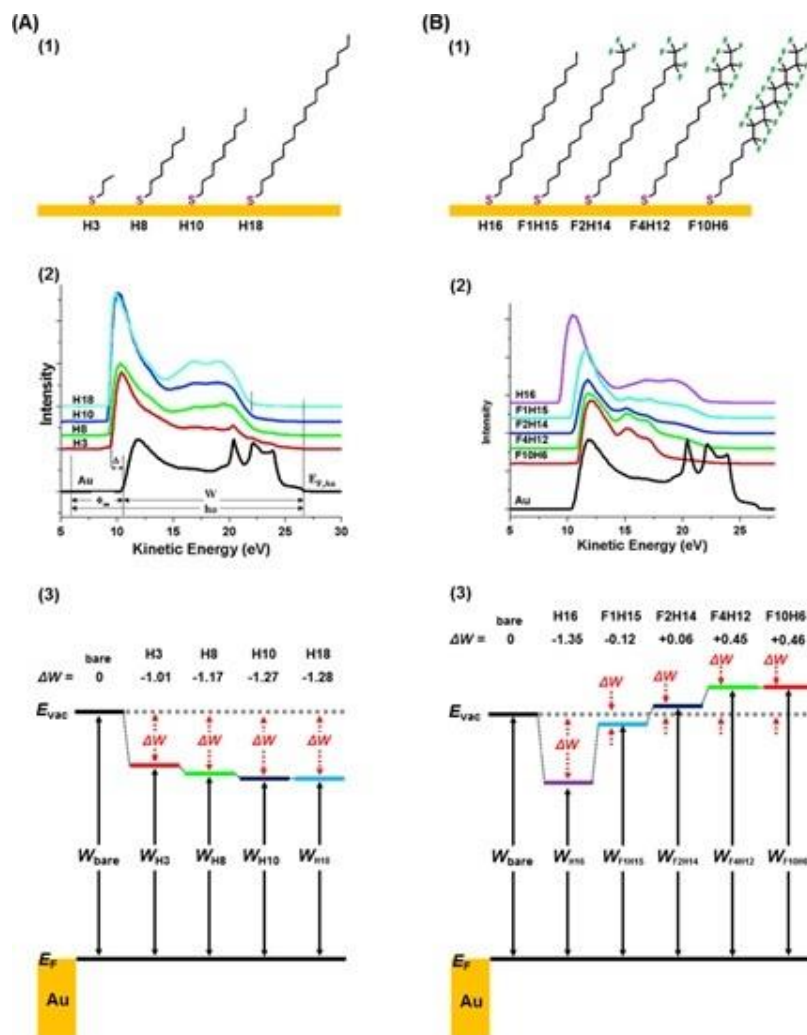


**Figure 71.** A1 and B1 shows the chemical structure of SAMs. A2 and B2 represent the UV photoemission spectra for clean Au and corresponding Au modified SAM. A3 and B3 is schematic diagram of the differences in work function ( $\Delta W$ ) of Au and modified surface. Retrieved from ref [102].

### 1.3 Advantage of conjugated SAMs for work function tuning

Alkyl chains possessing intrinsic electrically insulating characteristics was a limitation on the use of monolayers consisting of long-chain alkyl thiols for modifying injection barriers between metals and organics. More promising for this type of applications seems to be the monolayers consisting of  $\pi$ -conjugated thiols which were observed to exhibit considerably enhanced conductivity. Hence, very much attention was put on SAMs prepared from oligophenylthiols which have an aromatic. Oligophenylthiols'

molecular backbone is rigid and they have strong  $\pi$ - $\pi$  interactions that increase the stability of the formed monolayers against thermally induced disorder hence accounting for the problem present in case of alkyl derivatives. However, the low solubility of these aromatic molecules is a synthetic challenge. Chen et al. studied work function of gold decorated with series of differently substituted terphenyl thiol SAMs. They were able to show that a depression of the work function takes place in thiol coated gold when compared with clean gold. The authors showed their ability to tune the work function from 4.30 eV to 4.95 eV by simply using different SAMs on top of the gold electrodes. **Figure 72** shows the structures of the SAMs and the corresponding values of the measured work function. [103]

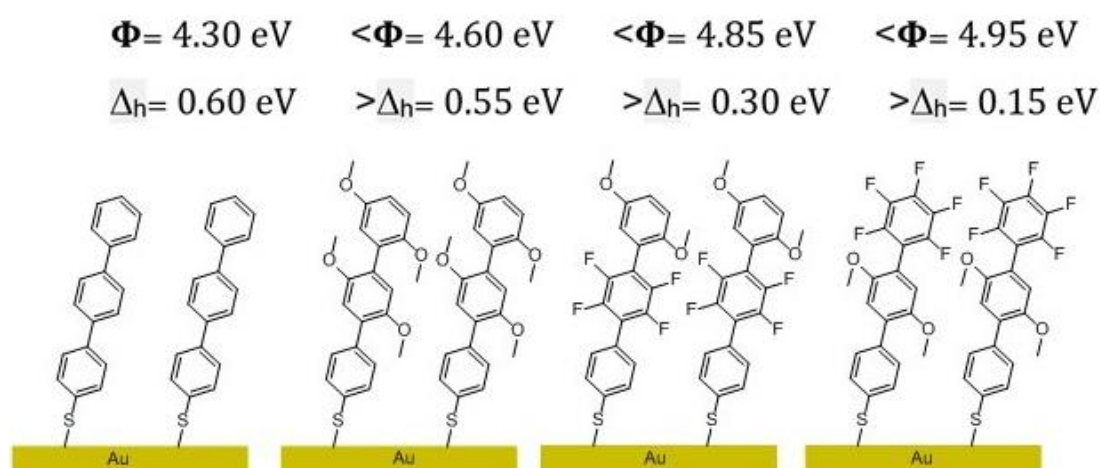


**Figure 72.** Oligophenylthiols SAMs structure and effect of them on work function.

## 2. Functionalization of carboranethiols

In this part m-carborane-1-thiol (M1) functionalized to 1-mercato-7-carboxy-m-carborane via nucleophilic substitution reaction. **Figure 73** shows synthetic route of carboxylic acid functionalized M1. 100 ml freshly distilled diethyl ether was prepared by distillation in presence of sodium and benzophenone. Then 300 mg of M1 dissolved in 50 ml of fresh diethyl ether under  $N_2$  atmosphere. After that, reaction medium brought to  $-73\text{ }^\circ\text{C}$  via dry ice. After 30 min n-buthyl lithium was added via canola over period of 1 hour. It stirred for extra 1 hour at this temperature. Then dry ice was added to mixture in excess amount and stirred reaction to maintain room temperature. Then reaction stirred at room temperature for 2 hours. Then 20 ml water added. The mixture extracted via diethyl ether and addition 10% HCl (50ml). Organic layer was evaporated and sample purified via sublimation. The system used for sublimation was large with respect to amount of the product, hence some product may escaped before crystallization on cold side. Therefore, column chromatography was used to purify product (hexane as elute, the yield is 27%). The IR spectra of reactant and product are depicted in **Figure 74**. The peak of carboxyl acid in  $3000\text{ cm}^{-1}$  is show formation of the product. The  $^1\text{H}$  and  $^{13}\text{C}$  NMR spectra of the product are depicted in **Figure 75** and **Figure 76**.

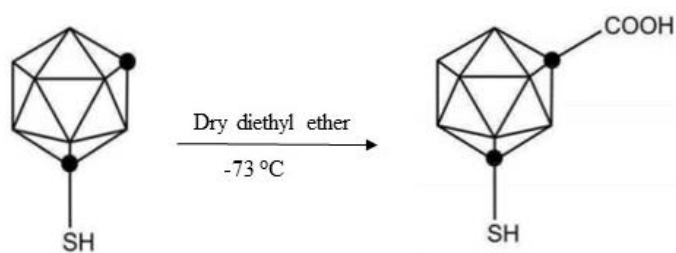


**Figure 73.** Synthetic route of 1-Mercapto-1,7 -dicarba-*closo*-dodecaborane-7-carboxylic acid.

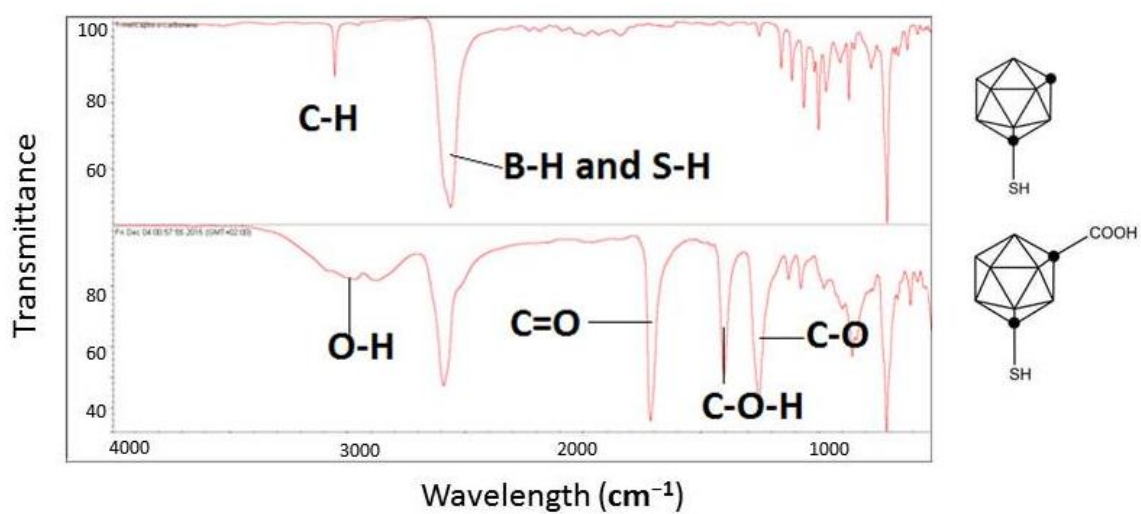


**Figure 74.** IR spectra of reactant (upper row) and product (bottom row).

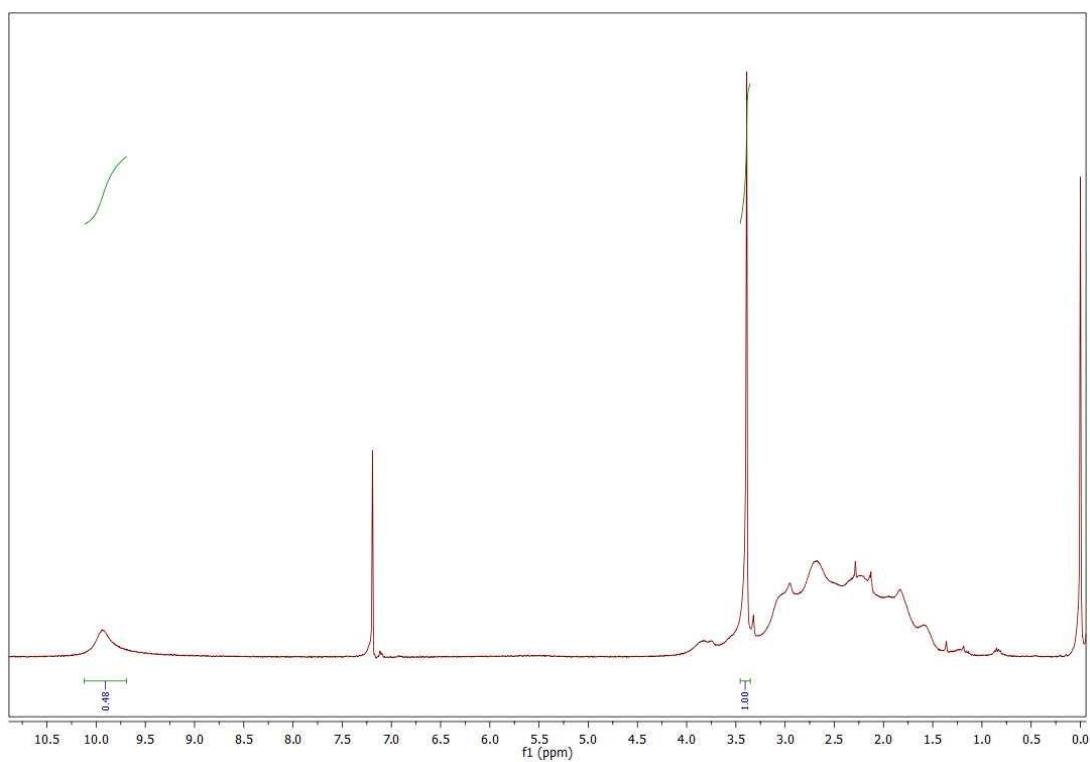


**Figure 75.** <sup>1</sup>H of 1-Mercapto-1,7 -dicarba-*closo*-dodecaborane-7-carboxylic acid

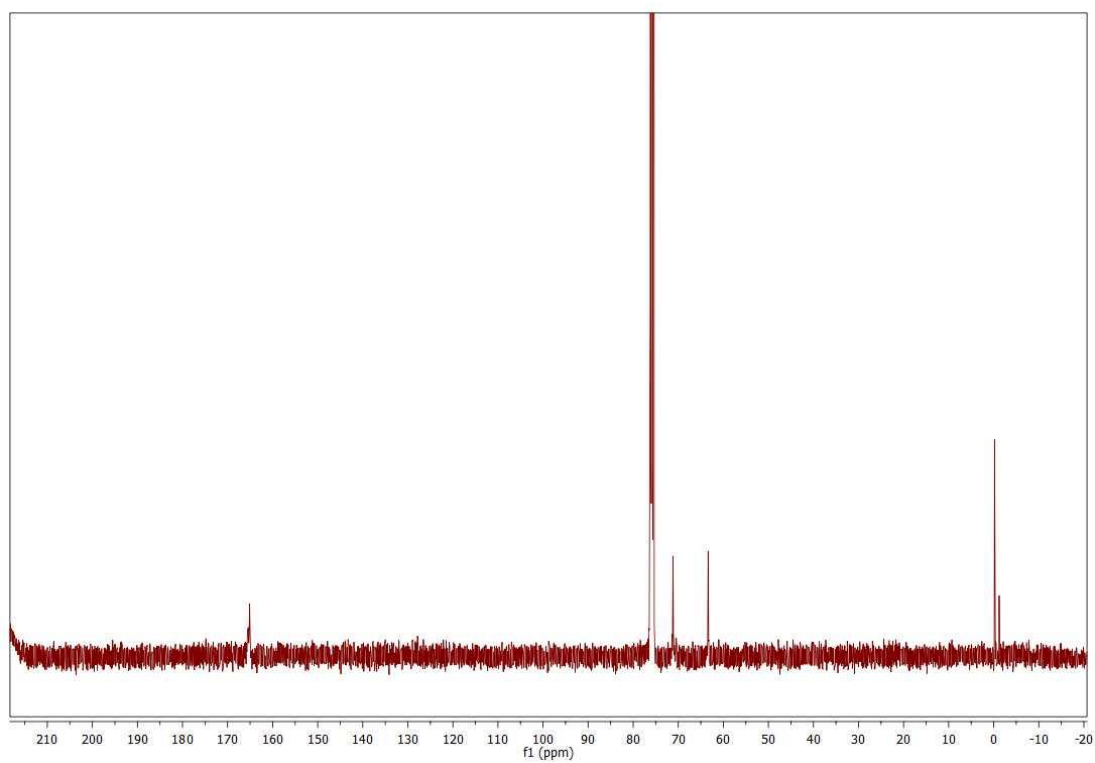
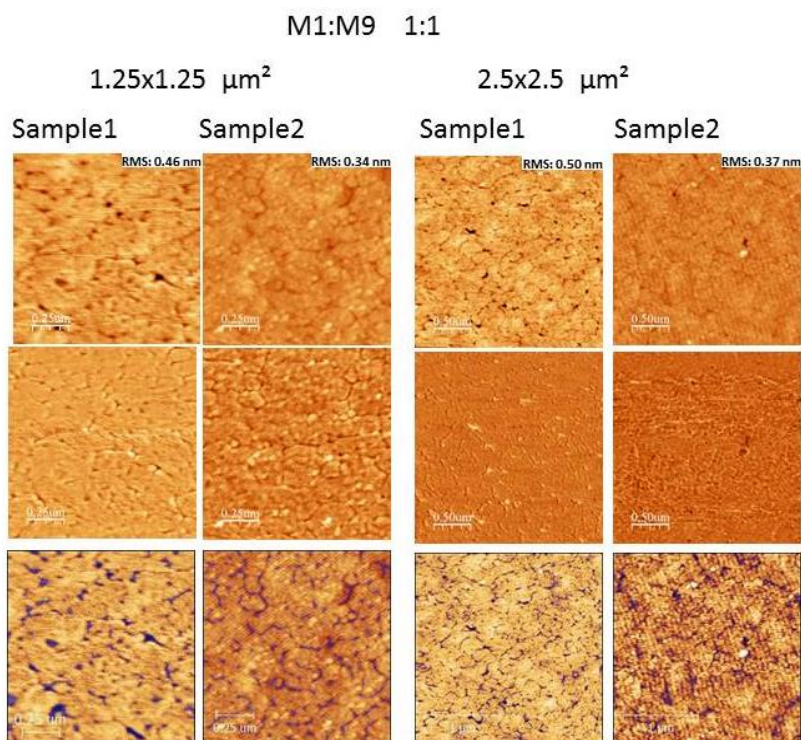
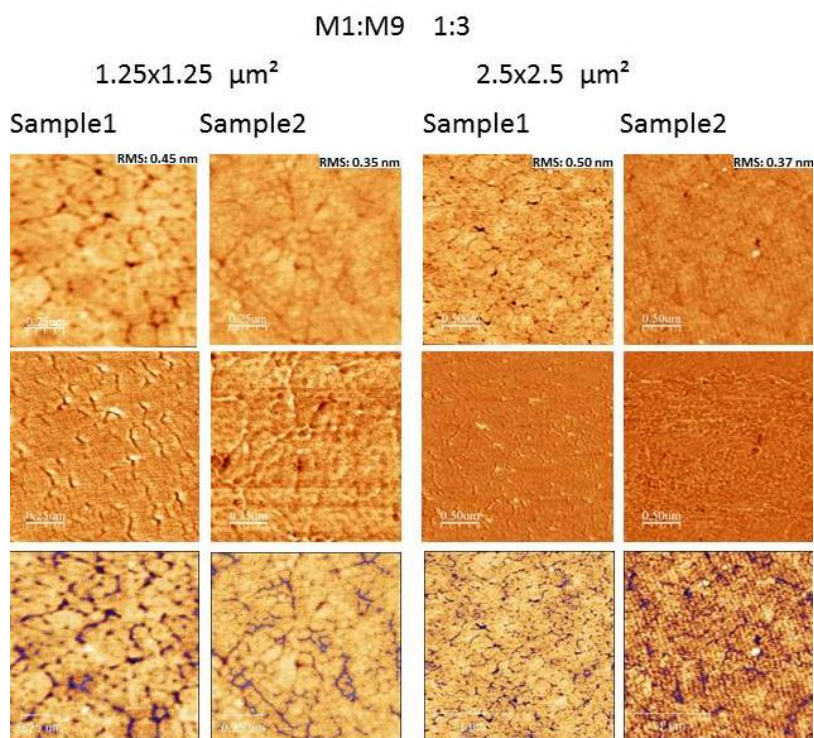


**Figure 76.**  $^{13}\text{C}$  NMR 1-Mercapto-1,7-dicarba-*closo*-dodecaborane-7-carboxylic acid.

**3. AFM image analysis: Raw image (upper row), phase image (middle row) and analyzed image (bottom row).**



M1:M9 3:1

1.25x1.25  $\mu\text{m}^2$

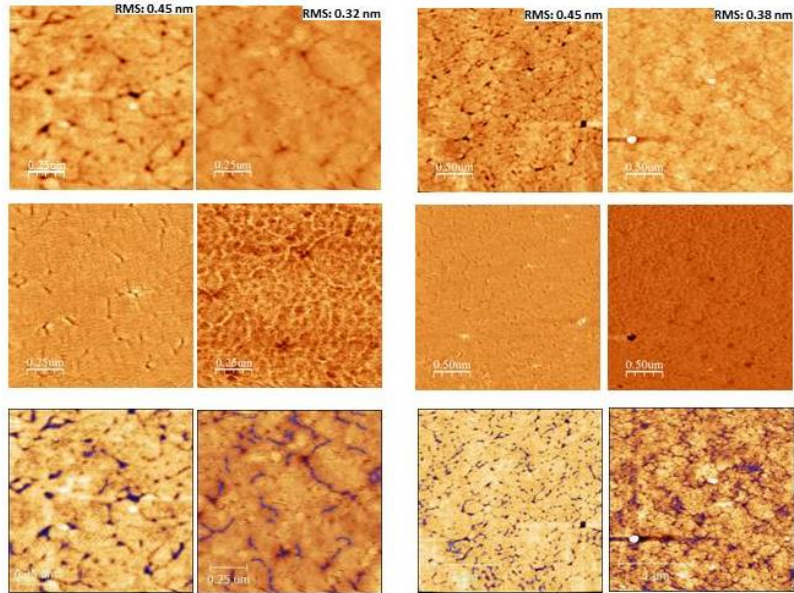
2.5x2.5  $\mu\text{m}^2$

Sample1

Sample2

Sample1

Sample2



O1:M1 1:3

1.25x1.25  $\mu\text{m}^2$

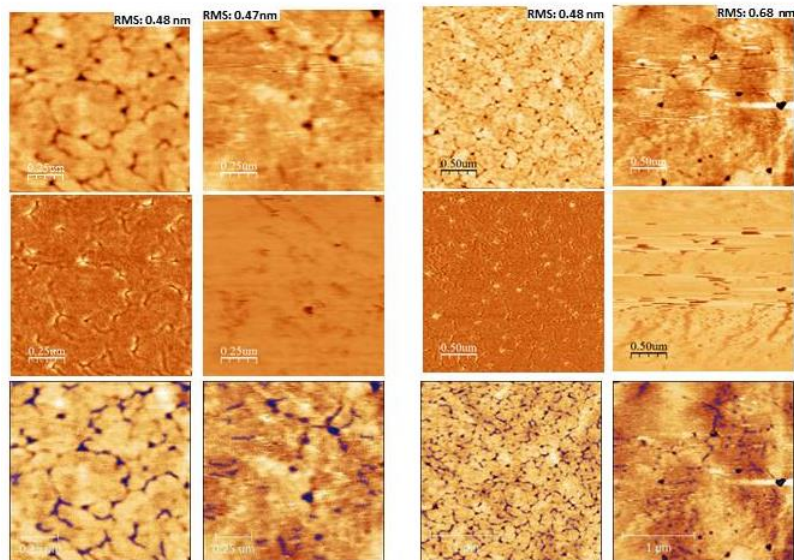
2.5x2.5  $\mu\text{m}^2$

Sample1

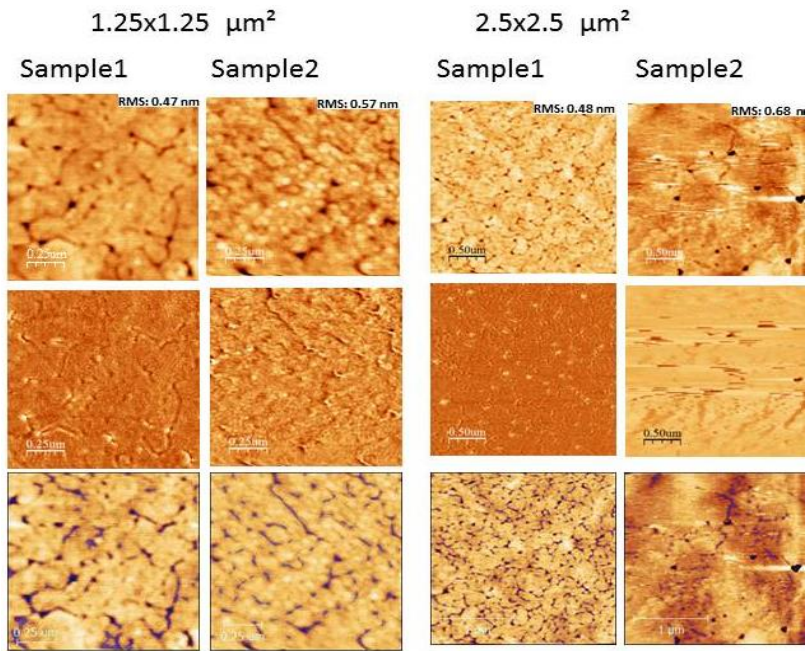
Sample2

Sample1

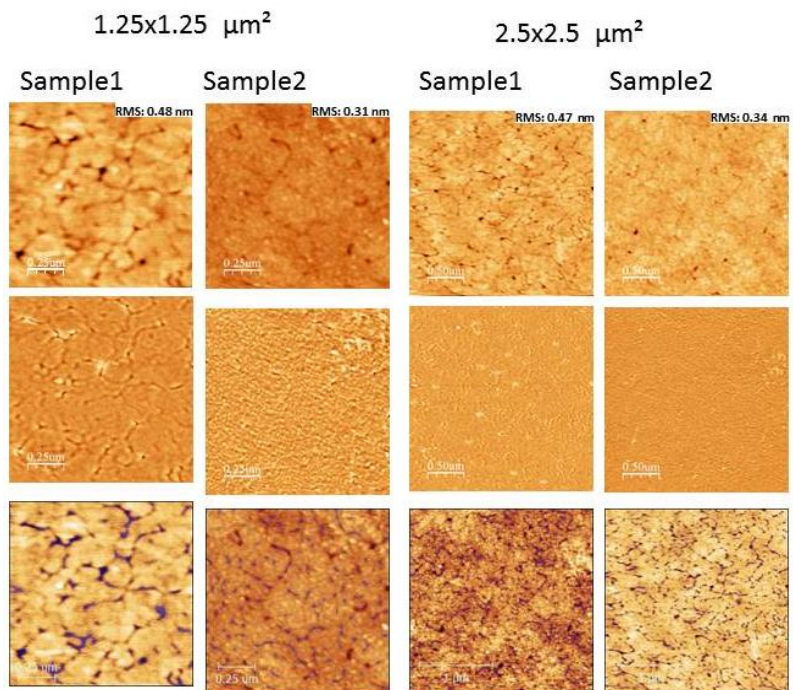
Sample2



O1:M1 1:1



O1:M1 3:1



O1:M9 1:3

1.25x1.25  $\mu\text{m}^2$

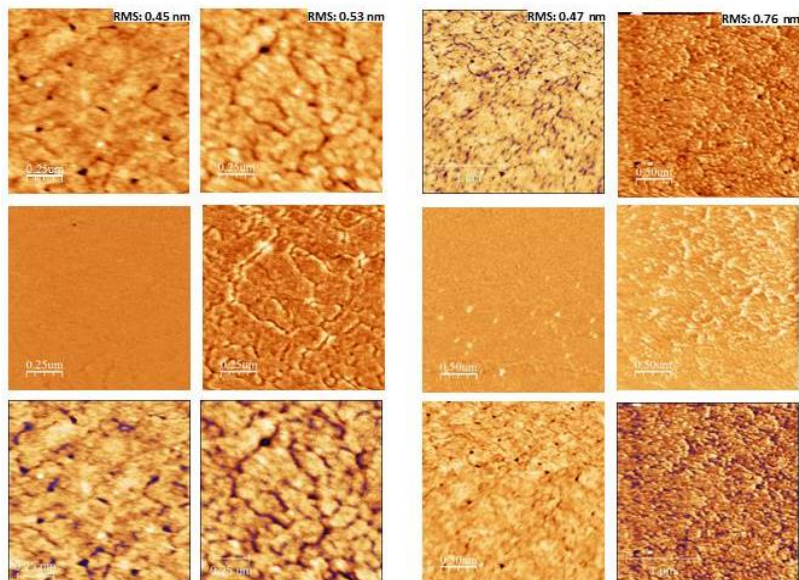
2.5x2.5  $\mu\text{m}^2$

Sample1

Sample2

Sample1

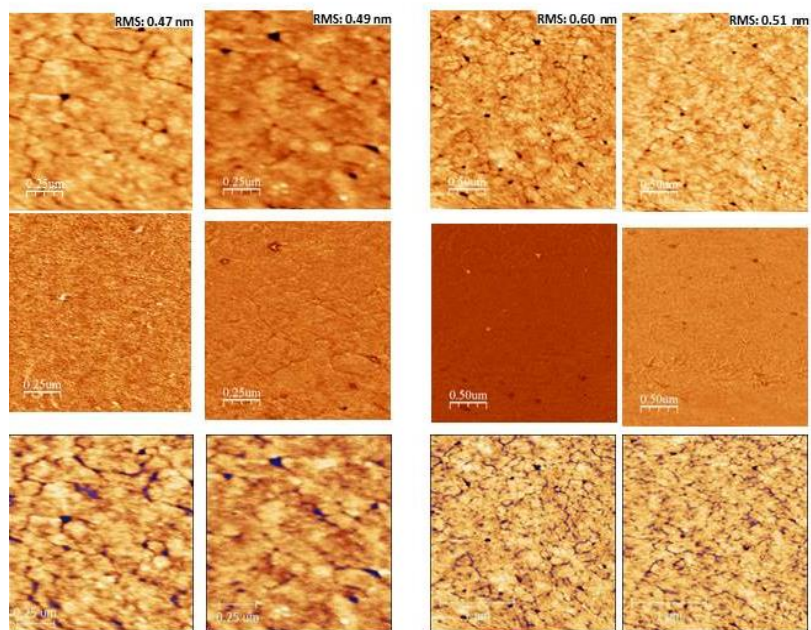
Sample2



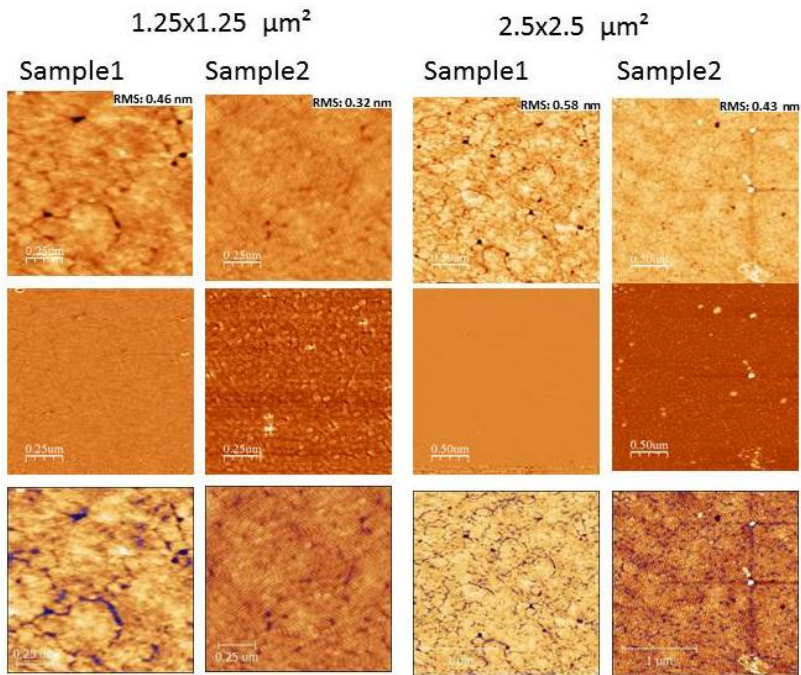
O1:M9 1:1

1.25x1.25  $\mu\text{m}^2$

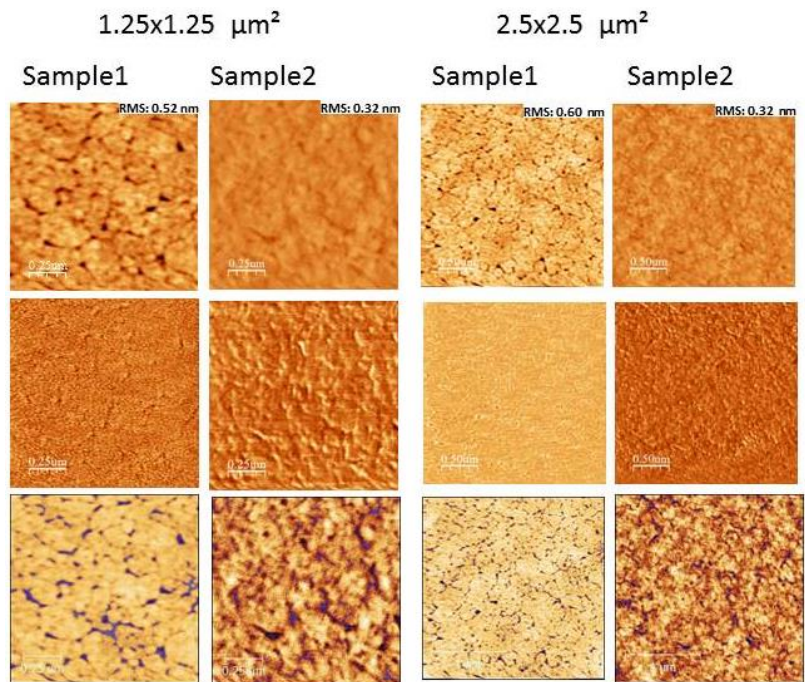
2.5x2.5  $\mu\text{m}^2$



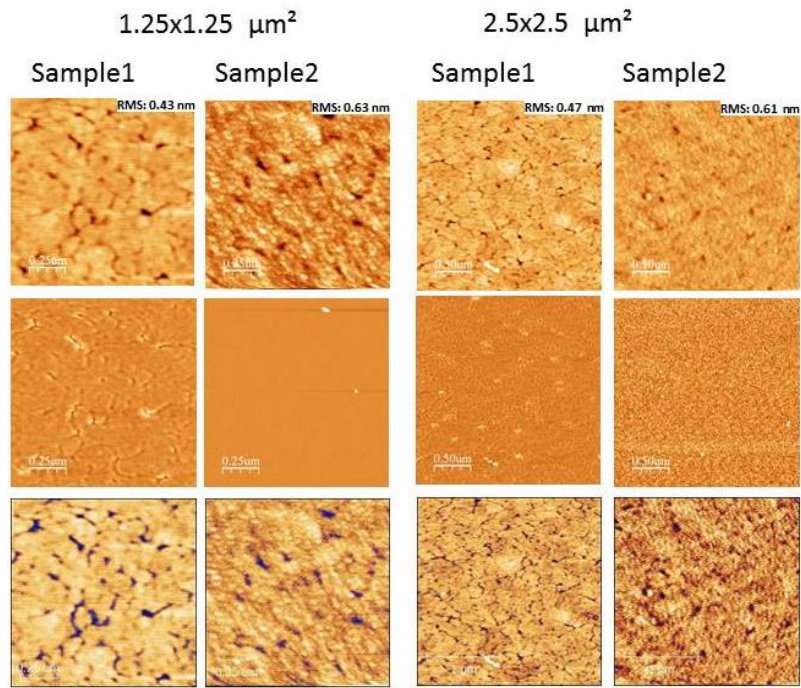
O1:M9 3:1



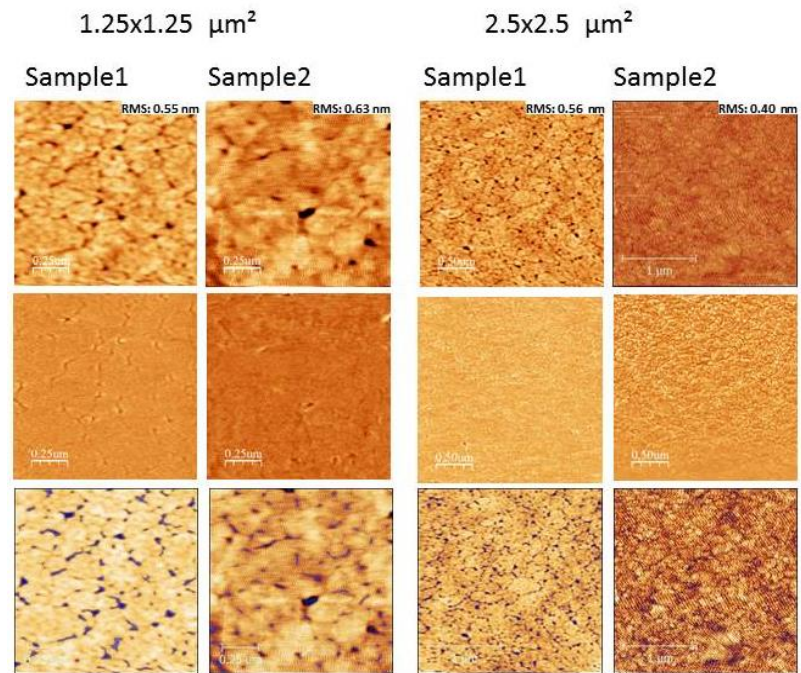
M9



M1



O1



#### 4. Contamination observed on mica substrate upon heating



**Figure 77.** Contamination observed on mica substrate upon heating.